DISSERTATION

Titel der Dissertation

„Investigation of Mechanical Behavior and Failure Mechanisms in Miniaturized Solder Interconnects“

Verfasser

Mag. Julien MAGNIEN

angestrebter akademischer Grad

Doktor der Naturwissenschaften (Dr. rer. nat.)

Wien, 2015

Studienkennzahl lt. Studienblatt:	A 796 605 411
Dissertationsgebiet lt. Studienblatt:	Physik
Betreut von:	O. Univ.-Prof. Dr. Herbert Ipser Dr. Golta Khatibi

ABSTRACT

Modern electronic systems, like SMDs (surface mounted devices), are composed of a variety of materials (ceramics, metals and polymers), with different electrical, thermal and mechanical properties and they are broadly used in automotive applications. Especially the solder joints in electronic devices are subjected to thermo-mechanical, electrical and vibrational loads during production and operation. Thermal mismatch and mechanical stresses, seriously affect the reliability of these systems.

In the recent years following the rising global trend in environmental issues and in compliance with RoHS directive, the use of lead-free solder has become mainstream. Development of lead-free alloys especially for automotive applications with high reliability demands has been subject of extensive investigations. Still due to the high number of potential lead-free solders, detailed investigations on the mechanical and thermal response of industrially relevant solder alloys are missing. In this PhD thesis isothermal static and dynamic behavior of the commonly used Sn3.5Ag0.75Cu solder alloy was investigated by using model solder joints and commercial SMD capacitors (CC 0805), which is recently used in automotive industry. Model solder joints of Cu/Sn3.5Ag0.75/Cu were used for characterization of the stress-strain, creep and thermal strain properties of the solder with respect to microstructural and constraint effects. The effect of IMC growth and microstrcutural changes on solder properties is much stronger for miniaturized solder joints than in bulk materials. The reliability and functionality of the SMD is primarily associated with the lifetime of the solder joint. Thus the fatigue response of the lead-free solder joints at the relevant length scale and temperature under low and high cycle mechanical loading was investigated by using commercial SMD capacitors. The main influencing factors on mechanisms of solder fatigue such as joint size, microstructure and testing temperature were investigated. Fatigue lifetime and the failure modes of the surface mounted solder joint subjected to high frequency mechanical loading were discussed and compared with thermally induced solder fatigue failure observed in the SMD capacitors. Testing at elevated temperature and after long term aging at 150°C resulted in a clear change of crack path and fracture mode, which is equal to the failure mode in the solder joints as observed due to traditional thermal cyclic procedures.

The extended knowledge gained in this thesis shall contribute to a better understanding of solder joint properties in real structures and their thermal and

mechanical response under operational conditions. The experimental results provide the basis for establishment of improved material models for Finite Element Simulations and lifetime prediction of solder joints. The results may allow determination of the weak sites in design and production of SMDs integrated in complex systems for mobile and automotive applications. The access to new design tools, which enable quicker and more reliable designs, with a reduction of rejection rates and better product quality, would be conceivable.

ZUSAMMENFASSUNG

Moderne elektronische Systeme wie SMDs (Surface Mounted Devices), bestehen aus einer Vielzahl von Materialien (Keramik, Metalle und Polymere), mit verschiedenen elektrischen, thermischen und mechanischen Eigenschaften. Besonders die Lötstellen in elektronischen Komponenten sind während der Produktion und im Betrieb thermo-mechanischen, elektrischen und vibrations Kräften ausgesetzt. Vor allem die Wärmeausdehnung und die mechanische Beanspruchung beeinträchtigen die Zuverlässigkeit dieser empfindlichen Systeme.

Die Dissertation behandelt das statische und dynamische isotherme Verhalten von Sn3.5Ag0.75Cu Modell Verbindungen und kommerziellen SMD Kondensatoren (CC 0805), die vor allem in der Automobilindustrie eingesetzt werden. Das mechanische und thermische Verhalten industriell relevanter Lötlegierungen ist durch die hohe Anzahl an möglichen bleifreien Verbindungen nicht ins Detail untersucht. Zur Charakterisierung der Spannung-Dehnung, Kriech und thermischen Dehnungseigenschaften des Lotes wurden Modell Lotverbindungen Cu/Sn3.5Ag0.75/Cu, hinsichtlich der Untersuchung mikrostruktureller Eigenschaften und miniaturisierungs Effekte herangezogen. Der Einfluss von IMC Wachstum und mikrostruktureller Änderungen auf die Materialeigenschaften ist bei miniaturisierten Lötstellen stärker als in Bulkmaterialien. Die Zuverlässigkeit und die Funktionalität der SMDs stehen hauptsächlich mit der Lebensdauer der Lötverbindung in Zusammenhang. Das Ermüdungsverhalten der Lötstellen in kommerziellen SMD-Kondensatoren wird im entsprechenden Maßstab unter niedrigen und hohen isothermen mechanischen zyklischen Belastungen untersucht. Wichtige Einflussgrößen wie Mikrostruktur und Testtemperatur standen hierbei im Fokus der Untersuchungen. Die Lebensdauer und die resultierenden Schadensbilder der Lötstellen unter hochfrequenter mechanischer Belastungen wurden diskutiert und mit thermisch induzierten Lot Ermüdungsbrüchen in SMD-Kondensatoren verglichen. Die Testung bei erhöhten Temperaturen und eine Langzeitalterung bei 150°C führten zu einer markanten Veränderung des Bruchverlaufs, welche vergleichbar mit Rissverläufen in Lötstellen belastet durch herkömmliche thermische zyklische Verfahren ist.

Die in dieser Arbeit gewonnen Kenntnisse führen zu einem verbessertes Verständnis von Lötstellen in realen Komponenten unter thermischen und mechanischen Randbedingungen. Die Versuchsergebnisse bilden die Grundlage für die Erstellung von verbesserten Materialmodellen für Finite Elemente Simulationen und Lebensdauervorhersage von Lötstellen. Diese ermöglichen eine Bestimmung von Schwachstellen in Design und Produktion der komplexen SMD Bauteilen integriert in Mobil und Automobilanwendungen. Der Zugriff auf neue Design-Tools, für die Entwicklung schnellerer und zuverlässigerer Designs mit einer Reduzierten Ausschussrate und einer besseren Produktqualität wäre an denkbar.

ACKNOWLEDGMENTS

I would like to express my appreciation and sincere thanks to my research supervisors, Prof. Dr. Herbert Ipser and Dr. Golta Khatibi, who have provided me the guidance and encouragement throughout the pursuit of this degree. Their advice has been invaluable and kept my motivation and determination at the highest level. I also wish to thank my colleagues Mag. Bernhard Czerny and Mag. Thomas Walter for their valuable discussions and critical reflections.

This work was carried out through the Comet-K Project A.7-11 „Life time of functional multilayer ceramic systems“ supported by the MCL (Material Center Leoben). I would like to recognize the help of several key members of the project, industrial partners and fellow graduate students. Special thanks are due to Dr. Oldrich Sevecek and Dr. Martin Lederer for their FEM simulations for this research thesis.

Finally, I would like to express my profound gratitude to my wife, Natascha Magnien for her encouragement and support throughout this work.

TABLE OF CONTENTS

NOMENCLATURE

ASTM	American Society for Testing and Materials
BGA	Ball Grid Array
$BaTiO_3$	Barium Titanate
CCD	Charge Coupled Device
CSP	Chip Scale Package
CTE	Coefficient of Thermal Expansion
DIC	Digital Image Correlation
EIA	Environmental Impact Assessment
FEM	Finite Element Modeling
FFT	Fast Fourier Transform
FMCS	Functional Multilayer Ceramic Systems
FR-4	Flame Retardant - 4
IMC	Intermetallic Compound
IPC	Institute of Printed Circuits
ITRI	Tin Markets, Technology and Sustainability
JEIDA	Japan Electronic Industry Development Association
LIS	Laser Interferometric System
NCMS	National Center for Manufacturing Sciences
NEMI	National Electronics Manufacturing Initiative
NIST	National Institute of Standards and Technology
PCB	Printed Circuit Board
PCIF	Printed Circuit Interconnection Federation
PID	Proportional Integral Derivative
RoHS	Restriction of Hazardous Substances
SAC	SnAgCu
SiC	Siliciumcarbid
SM-C	Surface Mounted Capacitor
SMD	Surface Mounted Device
SnAgCu	Tin Silver Copper
SnBiAg	Tin Bismuth Silver
SGT	Strain Gradient Theory
UTS	Ultimate Tensile Strength
VIC	Virtual Image Correlation

A_0	initial area
Ag	Silver
α	coefficient of thermal expansion
b	fatigue strength exponent
Bi	Bismuth
c	fatigue ductility exponent
Cu	Copper
$\mathrm{d_c}$	displacement (capacity sensor)
dl	change in length
ds	change between the Vickers indentations
dT	change in temperature
E	Young's Modulus
$e1$	first principle strain
ε	strain
$\dot{\varepsilon}$	strain rate
ε_e	elastic strain
ε'_f	fatigue ductility coefficient
ε_{max}	maximum strain
ε_p	plastic strain
F	force
H	failure probability
Ga	Gallium
In	Indium
k	reaction rate
k_0	frequency factor
L, l	length
L_0, l_0	initial length
λ	wavelength
Δm	relative fringe motion
n	stress exponent
N_f	number of load cycles
Pb	Lead
Q	activation energy
R	universal gas constant
RT	room temperature
Sb	Antimony
Sn	Tin
T	temperature
t	time
T_h	homologous temperature
Tm	melting temperature
σ	stress
σ_s	shear stress
$\dot{\sigma}$	stress relaxation rate
σ'_f	fatigue strength coefficient
v	velocity
Y	growth
Zn	Zinc

CHAPTER 1
Introduction: State of the Art

Lead-free solders are primary used in interconnection systems for electronic packages in the European Union (EU). Since July 2006 according to the two lead-free directives on waste electrical and electronic equipment (WEEE), and restriction of the use of certain hazardous substances in electrical and electronic equipment (RoHS) usage of lead (Pb) in electronics has been banned in the EU. Furthermore, other countries such as Japan follow the initiative to replace lead solders at the same time.

At present, the industry in cooperation with the existing international legislation (US, Japan, Europe, Australia, Denmark, Sweden) have created task forces to study the effects of replacement of Pb solder (IPC, EIA, NCMS, NEMI, NIST, PCIF, ITRI) with lead-free alloys. The challenge was selection of suitable Pb-free alloys, which comply with the industrial requirements regarding reliability, cost and availability. SnAgCu alloy was selected as the primary alternative due to its relatively low melting temperature, mechanical and thermal properties and solderability compared with other lead-free solders.

1.1. Lead-Free Solder Compositions

The potential lead-free solder alloy compositions must follow several criteria to replace effectively Pb containing solder alloys: melting temperature similar to SnPb solders, adequate wetting properties for the metallization, mechanical integrity, good fatigue resistance, compatible with existing liquid flux systems and low cost. The available supplies of potential elements as components in lead-free solders are listed in Table 1. Depending on the chosen elements different properties can be achieved. Eutectic SnAg solder alloyed with Zn, Cu, or Sb exhibit good mechanical strength and creep resistance. A BiSn basis solder doped with other elements is used in the low temperature soldering field. [1]

Among several candidate alloys, the SnAgCu alloy family is believed to be the preferred primary alternative together with alloys such as SnCu for wave soldering and hot air leveling and SnBiAg for surface mount technology. SnAgCu alloys were commonly used in reflow applications due its relatively low melting temperature (217°C), mechanical properties and solderability. The Japan Electronic Industry Development Association (JEIDA) has recommended Sn3.0Ag0.5Cu; the European Consortium has recommended Sn3.8Ag0.7Cu; and in US, NEMI has recommended Sn3.9Ag0.6Cu for reflow soldering and Sn0.7Cu for wave soldering [2].

Table 1. Supply status of potential candidate elements for lead-free solder applications. [1]

Element	*World production [10^3 kg]*	*World capacity [10^3 kg]*	*Spare capacity [10^3 kg]*
Ag	12,200	13,600	1,360
Bi	3,630	7,260	3,630
Cu	7,256,000	9,251,000	1,995,000
Ga	27	72	45
In	109	218	109
Sb	70,920	110,920	40,000
Sn	145,000	233,800	78,600
Zn	6,258,000	6,893,000	679,000

Alloy compositions are given in the form Sn3.5Ag$^{(a)}$0.75Cu$^{(b)}$, which means: (a) 3.5 % Ag and (b) 0.75 % Cu (percent by mass), with the leading element Sn making up the balance to 100 %. Through the many possible lead-free solder compositions, their effect on performance, lifetime and reliability of electronic devices are still unknown. It was observed that in comparison to tin-lead alloys, such as SnAgCu, are significantly stiffer, which result in higher solder joint loading under the same external deformation. One of the critical factors affecting the reliability of devices is the nature of the more brittle intermetallic layers that form the solder joint [3]. For this reason the further work is related to the lead-free solder composition Sn3.5Ag0.75Cu used in the automotive industry.

1.1.1. Microstructure and Intermetallic Compound of Lead-Free Solder

SnAgCu (SAC) solders are located in the Sn rich corner of the Sn-Ag-Cu liquidus projection (Figure 1.1). The solder alloy was chosen based on the existence of a ternary eutectic reaction and the opportunity of a low melting point. The solidification of this ternary eutectic involves the solid phases β-Sn, Ag_3Sn and Cu_6Sn_5. There are three thermodynamic events which take place during a cool down of the Sn3.5Ag0.75Cu alloy: L → L + Cu_6Sn_5 → L + Cu_6Sn_5 + β-Sn → β-Sn + Cu_6Sn_5 + Ag_3Sn. The microstructure of the eutectic Sn3.5Ag0.75Cu solder consists of a β-Sn phase matrix surrounded by fine Ag_3Sn and Cu_6Sn_5 intermetallic. Different cooling rates will modify the microstructure which implements the β-Sn grain size, orientation and number, as well as Ag_3Sn and Cu_6Sn_5 precipitate sizes and numbers. A detailed description of SnAgCu ternary eutectic alloys was done by Moon and Boettinger [4].

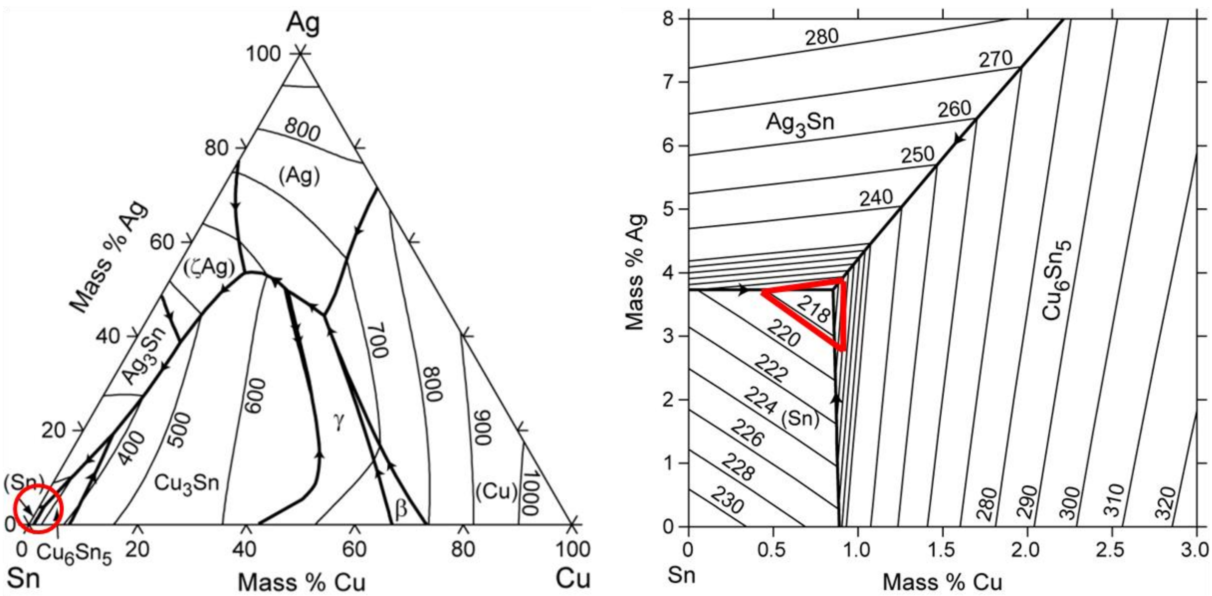

Figure 1.1.Liquidus projection of a SnAgCu system. [4]

1.2. Tensile Properties and Microstructure Analysis of Lead-Free Solder

The study of mechanical properties and microstructure is essential to understand the main characteristics of the possible solder alloys. The mechanical properties of solder alloys are determined by performing tensile experiments that replicate as closely as possible the service conditions. The microstructure and texture evolution also affect the mechanical performance and varies with the application and processing of the alloy composition. These properties are important in solder alloy selections for mechanical design.

1.2.1. Tensile Stress and Strain

Tensile testing is performed by elongating a defined specimen and measuring the axial load carried by the specimen. This test is a fully standardized destructive method to determine important mechanical properties. From knowledge of the specimen dimensions, the load and elongation data can be translated into a stress-strain curve. A variety of tensile properties can be extracted from a plot of stress σ versus strain ε. Figure 1.2 shows the typical ductile material stress-strain curve. The value of stress is given by dividing the amount of force F directed by the cross-sectional area A_0 of the specimen before any load is applied (1). Stress is usually measured in N/m² or Pa (1 N/m^2 = 1 Pa). The strain, which has no unit, can be calculated by using equation (2), where L is the instantaneous length of the specimen and L_0 is the initial length.

$$\sigma = \frac{F}{A_0} \left[\frac{N}{m^2}\right] \tag{1}$$

$$\varepsilon = \frac{L - L_0}{L_0} = \frac{\Delta L}{L_0} \tag{2}$$

The relationship between the applied load and resulting elongation is linear and represents the elastic deformation up to the yield point where the plastic deformation starts to occur while the material is loaded. This relationship is defined as Hooke's law where the ratio of stress to strain is constant, $E = {}^{\sigma}/_{\varepsilon}$. E is the modulus of elasticity or Young's modulus and is a measure of the stiffness of the material, but Hooke's law is not valid beyond the yield point. The stress at the yield point is called yield stress, and measures the resistance to plastic deformation. This yield point is chosen as that causing a permanent strain of 0.002. The maximum load which appears to the material is the ultimate tensile strength *UTS*. This all depends on the brittle or ductile nature of the material. Ductile materials have the ability to deform before braking and these can be given as percent maximum elongation ε_{max} or necking (3). The opposite are brittle materials and they break without significant deformation.

$$\%\, Elongation = \varepsilon_{max} \times 100\% \qquad (3)$$

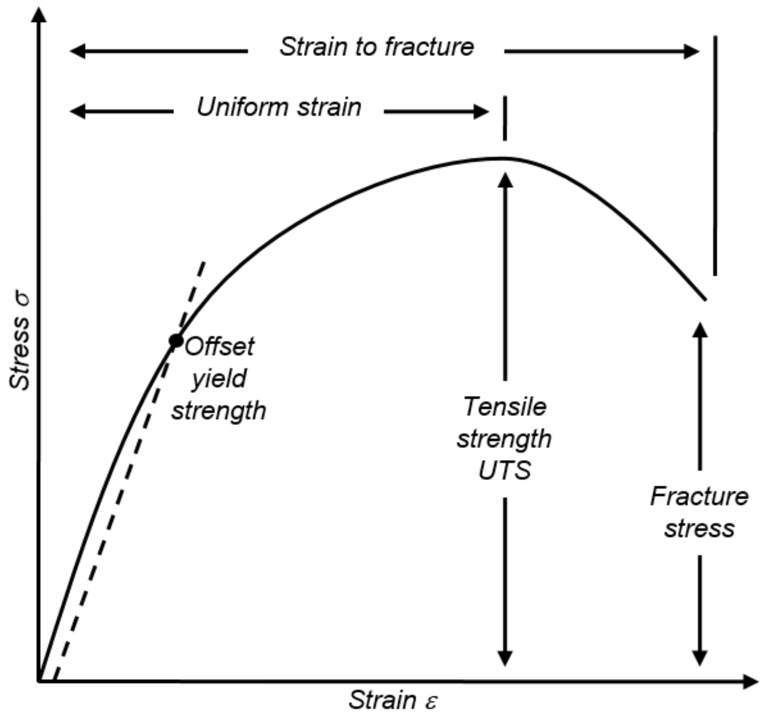

Figure 1.2.The engineering stress-strain curve. [5]

1.2.2. Tensile Properties of Lead-Free Solders

The material properties of lead-free solder, especially the tensile properties such as Young's modulus, yield strength and ultimate tensile strength are characteristics of the used material and are important key data to characterize the solder joint reliability of electronic packages, like chip scale package (CSP), ball grid array (BGA), surface mounted device (SMD) and flip chip. The specimen geometry, the solder microstructure, the strain rate and the testing temperature have an effect on the resulting tensile properties. Especially the microstructure and the miniaturization are the most important factors affecting the tensile properties of lead-free solders. The effect of miniaturization plays an important role by choosing the right specimen. Dog bone bulk samples of the solder alloy are used for characterization of the basic material. However, these samples do not represent the geometrical and microstructural effects of real solder joints. For a better characterization of the mechanical properties of the solder interconnects, model specimens with defined gap sizes and microstructures similar to those of the real devices are prepared by using suitable base materials and alloys. A representative overview of the constraint and microstructural effects in miniaturized solder joints is shown in Figure 1.3.

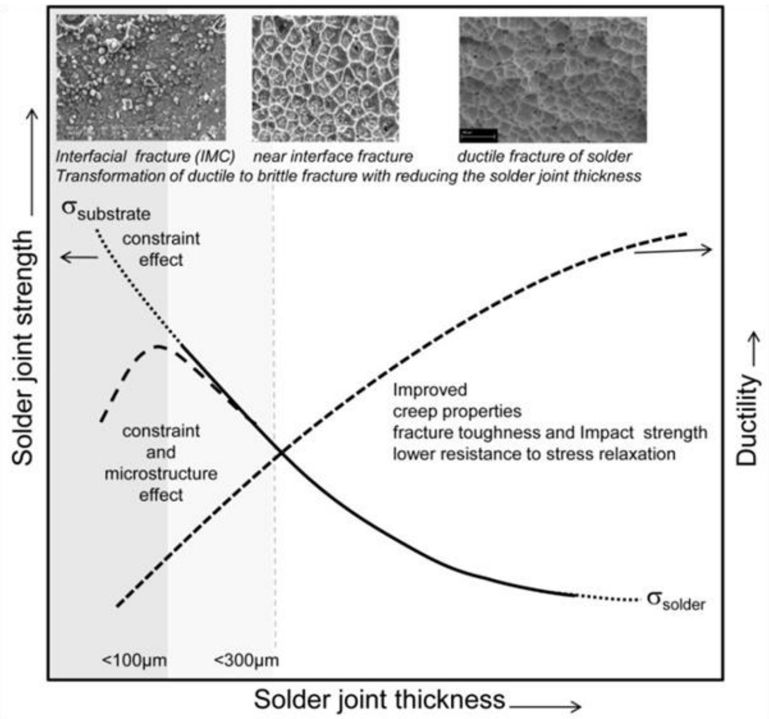

Figure 1.3. Constraint and microstructural effects on the relationship between gap size and strength of a solder joint. [6]

Due to the complexity of effects which can be influenced by the miniaturization of solder joints it is necessary to summarize them into two categories. First the microstructural effect describes a change of the texture and phase transition by a reduction of the solder volume resulting in a faster cooling rate. A faster cooling rate affects the size of Sn grains and the formation of interfacial IMC layers in lead-free solder alloys. A change in the texture and the IMC formation results in a change of the fracture mode. Secondly the constraint effect describes the hydrostatic stresses in the joint and will be modified by the strain rate and the specimen geometry. A reduction of the hydrostatic stresses will be achieved by increasing the solder gap thickness. [6]

A further point is the strain rate sensitivity of lead-free solders. Elongations in tensile tests depend on the strain rate and the existing microstructure after the reflow process. Figure 1.4 shows the engineering stress–strain curves of Sn3.5Ag0.7Cu bulk samples at strain rates ranging from 10^{-4} to 10^{-2} s^{-1} for two reflow cooling speeds (rapidly cooled R.C. and slowly cooled S.C.). The stress levels at both cooling speeds increase as the strain rate increases. The changes in UTS between the two cooling speeds can be reflected by microstructural changes. [7]

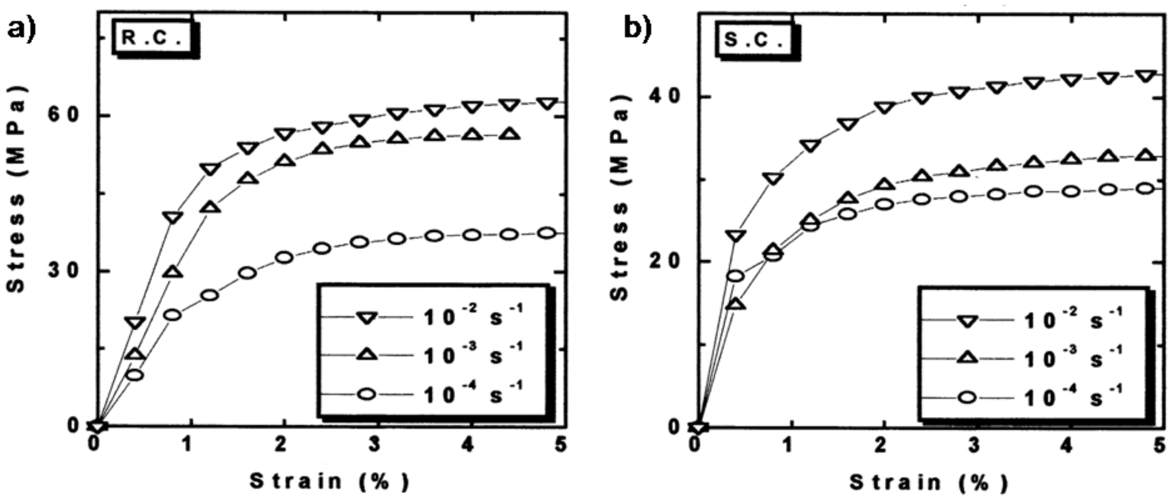

Figure 1.4. Engineering stress–strain curves in tensile tests at different strain rates and cooling speeds for Sn3.5Ag0.7Cu. [7]

The strain dependency of solder joints also determines the fracture behavior under cyclic deformations. In particular, the cyclic frequency dependency of thermal or mechanical loads is strongly affected by this effect. To study the complex stress-strain distribution of real devices, model solder experiments are investigated. Especially, influences of microstructure, strain rate and temperature on solder joints can be interpreted.

1.3. Creep Behavior of Lead-Free Solders

The creep behavior of lead-free solders is a material property, which is always present under thermal as well as mechanical loads. It is a time dependent deformation under a certain applied load. As a result, the material undergoes a time dependent increase in length, which could be responsible for failures in solder joints under static or dynamic loads and can be displayed via a stress / strain time relationship. The creep properties of a solder bulk alloy or solder joint can be determined by loading a solder specimen under constant stress (creep) or constant strain (stress relaxation). The microstructure and texture evolution also affect the creep performance and varies with the alloy composition.

1.3.1. Creep Properties – Stress Relaxation

Creep properties are important to understand the mechanical deformation of solder joints, because the creep processes involve progressive accumulation of plastic strain. Creep is a time-dependent plastic deformation measured as a function of applied load and temperature. The solder joint does not recover to the original shape and a permanent deformation remains after thermal or mechanical loading. The degree of creep depends on factors like material type or alloy composition, magnitude of load, temperature and time. The standard test method is application of a constant load to a specimen and the initial strain is predicted by its stress-strain modulus. Creep tests are long term measurements of strain or strain rate as function of time or load that may include all three stages of creep: primary, secondary (steady) and tertiary (third) creep, as illustrated in Figure 1.5. The material or alloy will deform slowly until rupture or yielding causes failure. However, creep data were often referred to the secondary creep, in which the creep rate is constant at fixed stress and temperature. This phenomenon of deformation of a material under load with time is called creep.

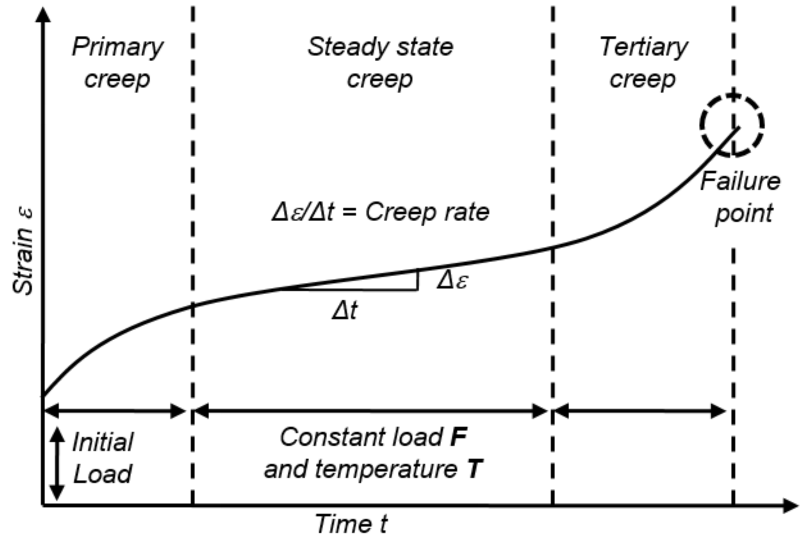

Figure 1.5. Illustration of an idealistic creep curve.

Another option to study the creep properties is the stress relaxation test subjected to a constant strain. This test has been proposed as an alternative test method to use a constant load, which is less time consuming. The stress relaxation test is more representative for deformation processes in a solder joint during thermo-mechanical cycle during operation of electronic devices. This context makes stress relaxations tests more suitable for reliability modeling in FEM simulations than creep tests. Therefore, the adequate characterization of the creep behavior of solder is one of the key issues in the reliability analysis of electronic packages and assemblies.

Stress relaxation is defined as a decrease in stress with time under a constant deformation or strain (Figure 1.6). This behavior of solder joint is studied by applying a constant deformation to the specimen and measuring the stress reduction as a function of time. If the solder joint is forced to hold a constant strain, the stress relaxation behavior can be regarded as a transition of the elastic strain into the plastic strain. Thus the stress reduction over the time $\frac{d\sigma}{dt}$ can be expressed as,

$$\frac{d\sigma}{dt} = E\frac{d\varepsilon_e}{dt} = -E\frac{d\varepsilon_p}{dt} \qquad (4)$$

where ε_e is the elastic strain, ε_p is the plastic strain and *E* is the Young's Modulus. A power law relationship was used to describe the temperature dependency of the stress relaxation.

$$\dot{\sigma} = A\sigma^n exp\left(\frac{-Q}{RT}\right) \tag{5}$$

where $\dot{\sigma}$ is the stress relaxation rate, *A* is a material constant, *n* is the stress exponent and *Q* is the creep activation energy. The stress exponent can be determined experimentally, by plotting the creep rate against the stress in a double logarithm coordinate. The stress exponent is given by the slope of linear dependency at a constant temperature. The activation energy can be determined by plotting the $\ln(\dot{\sigma})$ versus the reciprocal temperature. The activation energy, *Q*, and the stress exponent, *n*, depend on the creep mechanism, and have different values at different temperatures and applied stresses.

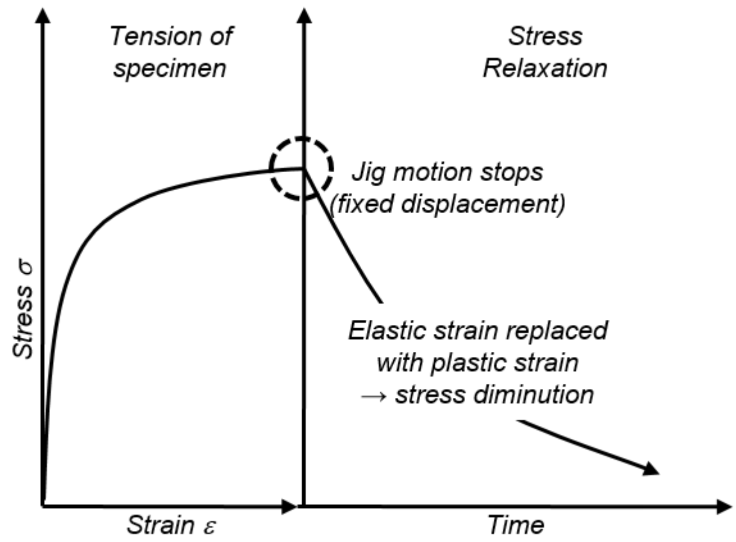

Figure 1.6. Illustration of the stress relaxation test using constant strain. [8]

1.3.2. Stress Relaxation Studies of Solder Joint

The characterization of creep behavior of solder alloys is usually done by using bulk samples. Due to the miniaturization of solder joints in electronic devices, the interest in creep response of solder alloys under conditions other than those encountered in bulk solders has been increased. In order to obtain relevant data for real solder joints, solder joint models are scaled down to the typical size or the real solder joints of the devices are used as specimen. The difficulty in comparison of the different values obtained for a typical solder alloy like SnAgCu using literature data is caused by two factors. Firstly different preparation steps to fabricate the specimens lead to variations in the microstructure with respect to the grain size and IMC formation.

Secondly the methodologies used to determine the creep properties of solder joints vary between different investigations, which includes the test type (creep or stress relaxation) and the test conditions. [9]

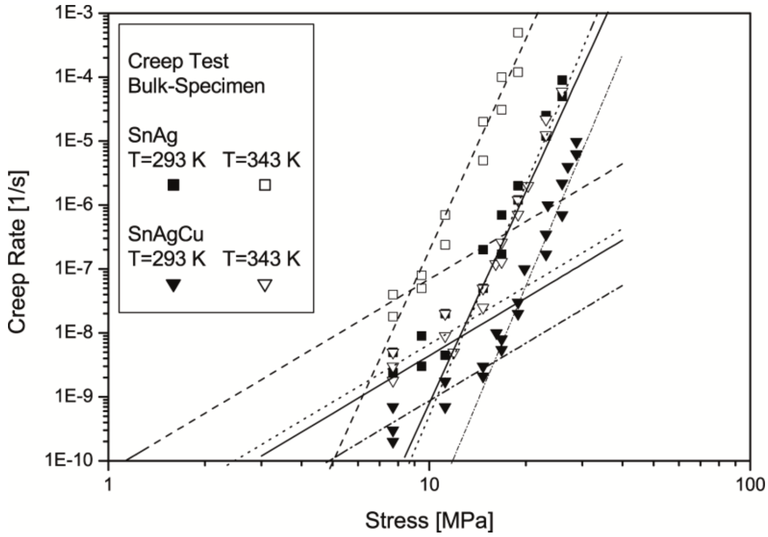

Figure 1.7. Results from creep tests on Sn3.5Ag and Sn3.8Ag0.7Cu bulk samples at test temperatures of 20°C and 70°C.[10]

The typical creep rates of lead-free solder alloys obtained for bulk specimens are shown in Figure 1.7. Sn3.5Ag and Sn3.8Ag0.7Cu bulk samples are characterized by a stress exponent of n = 11 for Sn3.5Ag and n = 12 for Sn3.8Ag0.7Cu with an activation energy of Q = 61 kJ/mol for both alloys [10]. The values are valid for the test temperatures 20°C and 70°C. Miniaturized solder joints show quite different creep behavior in comparison to bulk samples. For example, the creep experiments on micro solder balls (400 µm diameter) showed different stress exponents at different temperatures for the solder alloys Sn3.5Ag and Sn3.5Ag0.75Cu (Figure 1.8). The stress exponent for Sn3.5Ag is very similar to Sn3.5Ag0.75Cu and have the values n = 18, n = 12 and n = 8 at temperatures of 20°C, 75°C and 125°C [9]. Therefore the effect of IMC growth and microstructural changes on creep behavior is much stronger at solder joints than in bulk materials.

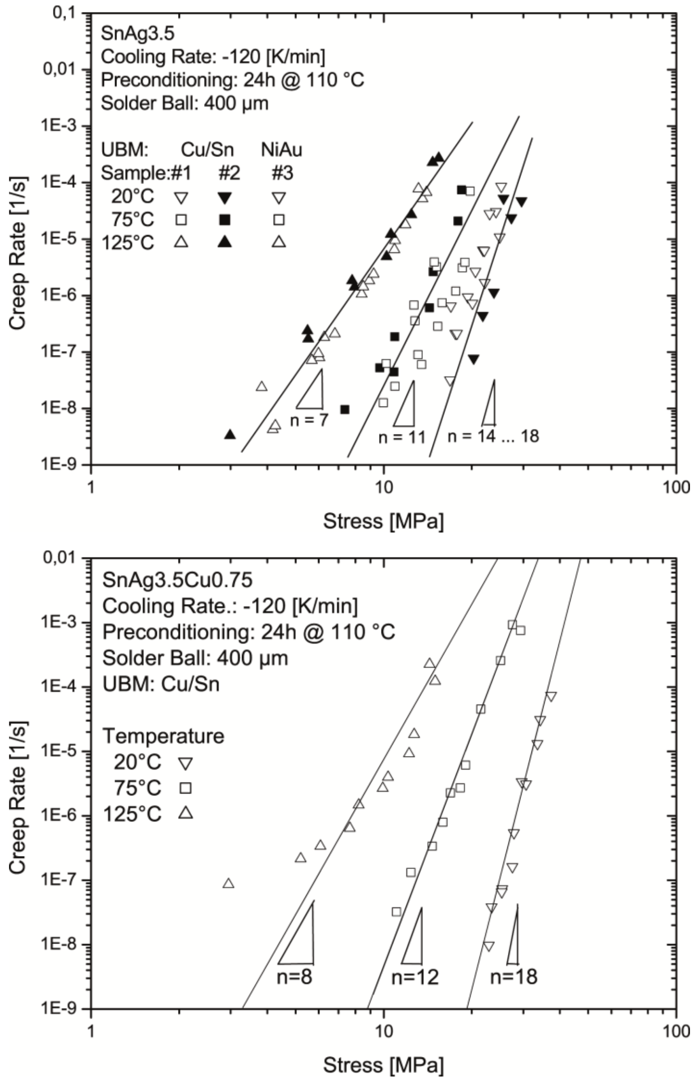

Figure 1.8. Results from creep tests on Sn3.5Ag and Sn3.5Ag0.75Cu solder balls (diameter 400 mm) at test temperatures of 20°C, 75°C and 125°C.[9]

1.3.3. Deformation Mechanisms of Creep

The mechanism of creep depends on dislocations, which are responsible for a main part of the plastic deformation of solders. Depending on the homologous temperature $T_h = T/T_m$ (T_m is the melting temperature of the material) and the applied stress during creep various microscopic processes were carried out. The strength of the solder alloy depends on the applied strain, strain rate and temperature. The dislocations are characterized by the dislocation density and by their spatial distribution. They can move under an applied stress and at higher temperatures by plastic flow. The underlying atomic processes, which cause flow, can be described in four terms of the mechanisms to which the atomic processes contribute. The deformations mechanisms are: 1) low temperature plasticity by dislocation glide which is limited by lattice resistance, discrete obstacles and phonons; 2) low temperature plasticity by twinning; 3) power law creep by dislocations glides and climbs which are limited by glide processes lattice-diffusion controlled climb (high-temperature creep) and core-diffusion controlled climb (low temperature creep). Further terms are the Harper-Dorn creep and creep accompanied by dynamic recrystallization; 4) diffusion flow which is limited by diffusion (Nabarro-Herring creep), grain boundary diffusion (Coble creep) and interface reaction controlled diffusion flow.

For solder materials, the mechanisms of stress relaxation or creep usually include bulk diffusion, dislocation climb/glide and grain boundary diffusion. The dominant deformation mechanism can be experientially reflected by the values of the stress exponent n and the activation energy Q. An overview of deformation behavior of tin and some tin alloys are given by Fuqian [11]. He comes to the conclusion that the plastic deformation of tin and tin alloys is not always clearly definable. Due to the complex crystal structure of Sn alloys, more studies are needed to understand the complex deformation mechanisms in solders.

1.4. Thermal Expansion Behavior

In this chapter the basic meaning of the coefficient of thermal expansion (CTE) will be explained and its importance for functional multilayer material systems. The CTE is a basic physical property, which is of considerable importance in mechanical and structural design applications of lead-free solders.

1.4.1. Coefficient of Thermal Expansion of Lead-Free Solder

The coefficient of thermal expansion (CTE) is one of the most important physical properties of materials. The thermal expansion mismatches between adjacent layers are the primary source of stress or strain. Since a small change in temperature, *dT*, will cause a linearly related change in length, *dl*, the coefficient of linear thermal expansion, *α*, is defined as

$$\alpha = \frac{1}{l_0}\frac{dl}{dT} \tag{6}$$

where l_0 is the initial length of the object. The linear thermal expansion is an average over a certain temperature interval (e.g. RT to 100°C), hence it is assumed to be constant within this temperature interval. CTE may be a function of temperature, thus accounting for nonlinearities in the expansion behavior. To determine the temperature dependence of the CTE, a general function by strain values must be specified which is usually defined by a higher polynomial function or by section-wise linearization of the strain curve.

1.4.2. Studies on the CTE of Lead-Free Solders Thermal Expansion

The CTE describes how the size of an object changes with a change in temperature. This thermal property of a material plays a major role in multilayer systems, such as for example in a surface mounted capacitor (SM-C), which is shown in Figure 1.9. Due to thermal mismatch especially under conditions of extreme temperature loads of the used materials, it comes to thermal stresses, crack initiation and crack growth under thermal influences. Finally it leads to the failure of the components and this is responsible for the functional deficits of microelectronic components. In addition to the thermal mismatch problem, the continuing miniaturization of electronic components is often responsible for a change in the reliability of electronic systems. The transition from macro to nanometer structures also leads to a change in the material properties, which must be taken into account. It is necessary to determine the thermo-mechanical properties of the used elements in microelectronic components considering their relevant dimensions and geometries [12].

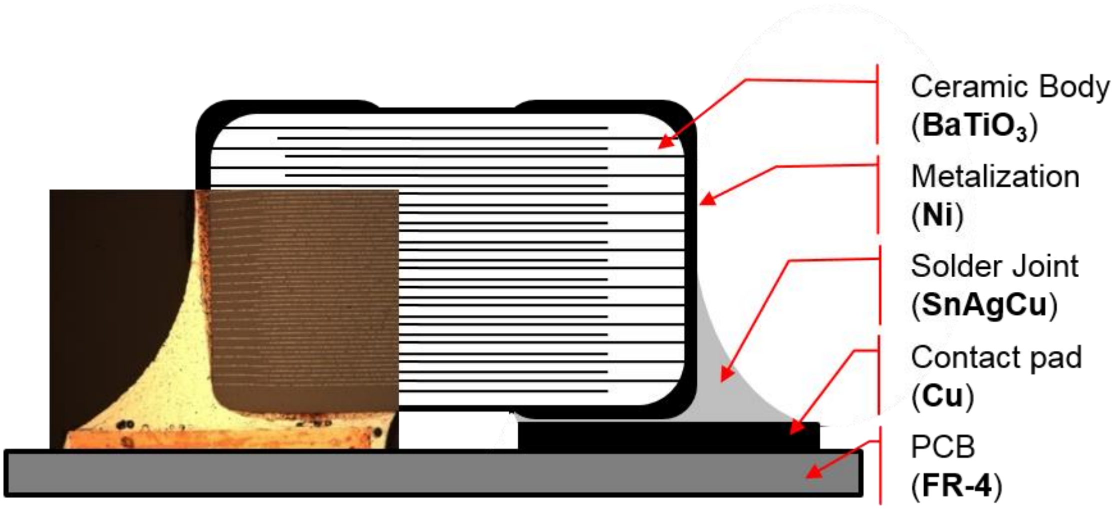

Figure 1.9. Schematically illustration of a surface mounted capacitor (SM-C).

Table 2. CTE and E-modulus of the used materials in a typically SM-C.

	CTE [ppm/°C]	E [GPa]	Reference
Sn3.8Ag0.7Cu	20 17	48.5(-55°C); 33(210°C) 46(25°C); 44(50°C); 35(100°C)	[13] [14]
$BaTiO_3$	6(0°C); 11(200°C) 8.5	 97.9	[15] [16]
Cu	16.7 17 17	117 82.7 123	[17] [14] [18]
FR-4	18.4	23	

Determination of the fatigue life under thermal cycling is based on the thermal mismatch of the used materials in a multilayer system. The normally used thermal fatigue profile ranges from -40°C to 125°C and is used as a standard accelerated cycle for automotive applications. Preliminary failure analysis has shown that the solder joint cracking and creep-fatigue damage are commonly observed in chip resistors on FR-4 substrates (PCB). The cracks begin underneath the component and then typically follow parallel along the capacitor termination. Once the crack reaches the edge of the capacitor, its path proceeds at either a 45°–60° angle to the board or continues parallel to the board. This crack propagation is shown in Figure 1.10 for a Sn3.8Ag0.7Cu solder joints in a SM-C. The resulting crack propagation is affected by the different coefficients of thermal expansion of the materials in the assembly (Table 2), the overall solder joint shape and the recrystallization phenomenon in the solder joint. Many works reported in literature [16][18][19][20][21] show these effects which affect the solder joint fatigue life during thermal cycles.

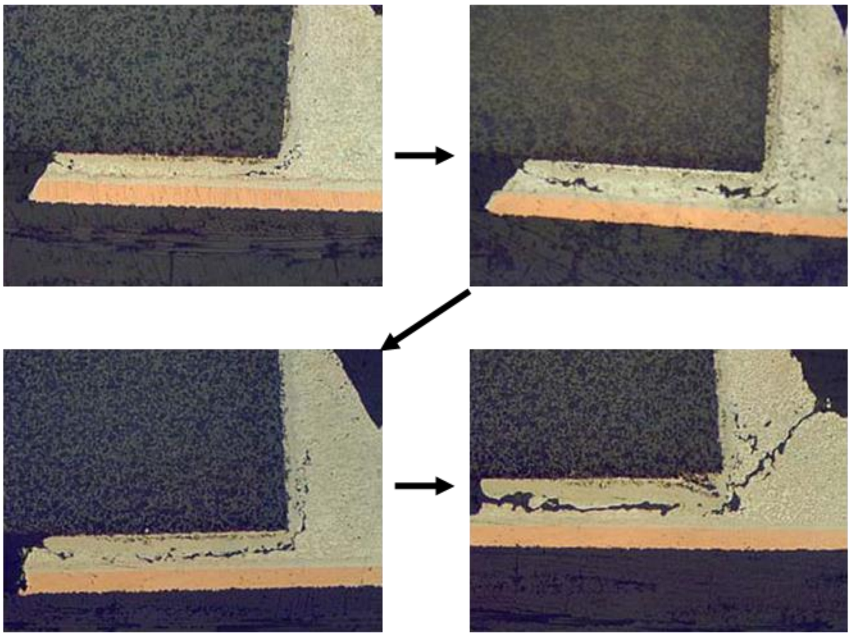

Figure 1.10. Crack propagation in a Sn3.8Ag0.7Cu of a SM-C due to thermal cycling (-40 to 125°C). [22]

1.5. Cyclic Fatigue

In general, fatigue is the failure or damage of a material subjected to repeated loading, at a load level that is lower than that required for failure upon one exposure. Low cycle fatigue (LCF) occurs at continuous cyclic loading $<10^3$ and high cycle fatigue at number of cycles $>10^3$. They are called time varying load fatigue, because of the accumulated permanent structure damage in the form of microscopic cracks at notches, defects or grain interfaces, acquired from repeated cyclic loading. The lifetime of materials under cyclic load is represented by a so-called Wöhler diagram (S-N diagram). The stress amplitude σ is plotted versus the logarithmic number of load cycles until failure $log(2N_f)$. The resulting curve describes the fatigue strength as a function of the number of load cycles. Such S-N plots are useful guides for lifetime prediction.

High cycle fatigue usually occurs from repeated deformations in the elastic range, and loading stresses much less than the yield stress of the material. The fatigue life can be expressed by the Basquin equation,

$$\frac{\Delta\sigma}{2} = \sigma_f'(2N_f)^b \quad (7)$$

where $\frac{\Delta\sigma}{2}$ is the stress amplitude, σ_f' is the fatigue strength coefficient and *b* the fatigue strength exponent, a material dependent constant. In low cycle fatigue, strains occur typically in the plastic range. For such situations, it is common to correlate strain with lifetime rather than stress (as in high-cycle fatigue). This relationship is often called a Coffin Manson relation and is defined as,

$$\frac{\Delta\varepsilon_p}{2} = \varepsilon_f'(2N_f)^c \quad (8)$$

where $\frac{\Delta\varepsilon_p}{2}$ is the plastic strain amplitude, ε_f' is the fatigue ductility coefficient and *c* the fatigue ductility exponent, a material dependent constant. The total strain is defined as the sum of elastic $\Delta\varepsilon_e$ and plastic strain $\Delta\varepsilon_p$ at constant strain amplitude.

$$\frac{\Delta\varepsilon}{2} = \frac{\Delta\varepsilon_e}{2} + \frac{\Delta\varepsilon_p}{2} \quad (9)$$

The Coffin Manson equation considers only plastic deformations. A combination with the Basquin equation over the Young's modulus E called Total Strain equation is defined as,

$$\frac{\Delta\varepsilon}{2} = \frac{\sigma'_f}{E}(2N_f)^b + \varepsilon'_f(2N_f)^c \qquad (10)$$

It is an improvement over the Coffin Manson equation in that it also accounts for the elastic range (Figure 1.11).

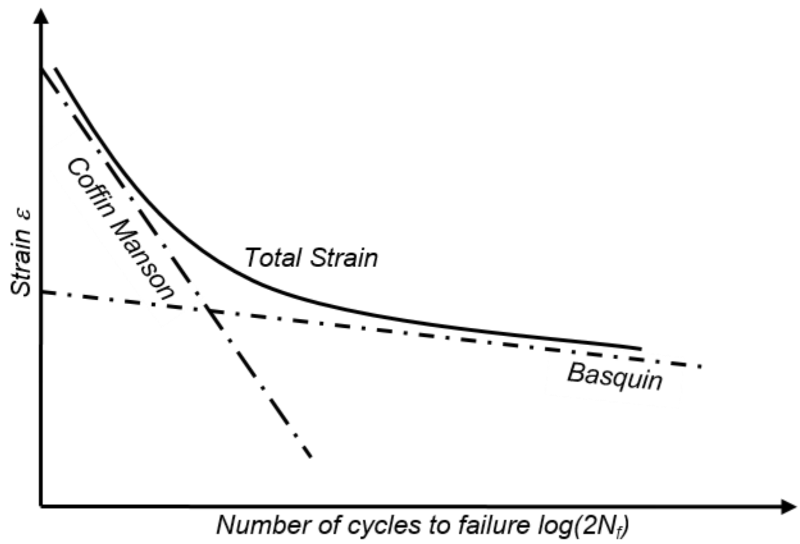

Figure 1.11. Total strain versus life equation.

This relation is the commonly used, but there are more possible models based on the fundamental mechanism for inducing damage. Lee et al [23] has summarized fourteen used possible solder joint models depending on their damage mechanism type. The fatigue life models of solder joints can be divided in five categories: stress based, plastic strain based, creep strain based, energy based and damage accumulation based models. Table 3 gives an overview of the fourteen solder joint fatigue models arranged by the mentioned categories.

Table 3. Summary of solder joint fatigue models. [23]

#	Fatigue model	Equation	Model class	Coverage	Constants
1	Coffin Manson	$\frac{\Delta\varepsilon_p}{2} = \varepsilon_f'(2N_f)^c$	Plastic strain	Low cycle fatigue	c = constant, ε_f'= fatigue ductility coefficient
2	Total Strain (Coffin Manson Basquin)	$\frac{\Delta\varepsilon}{2} = \frac{\sigma_f'}{E}(2N_f)^b + \varepsilon_f'(2N_f)^c$	Plastic strain + elastic strain	High and low cycle fatigue	b = fatigue strength exponent, c = fatigue ductility exponent, σ_f' = fatigue strength coefficient, ε_f' = fatigue ductility coefficient
3	Solomon	$\Delta\gamma_p N_p^\alpha = \theta$	Plastic shear strain	Low cycle fatigue	α = constant, θ = inverse fatigue ductility coefficient
4	Engelmaier	$N_f = \frac{1}{2}\left[\frac{\Delta\gamma_t}{2\varepsilon_f'}\right]^{1/c}$	Total shear strain	Low cycle fatigue	c = -0.442 -6e -4T_s +1.74e -2ln(1 +f), T_s = mean cyclic solder joint temp (°C), f = cyclic frequency (cycles/day), $2\varepsilon_f'$ = 0.65
5	Miner	$\frac{1}{N_f} = \frac{1}{N_p} + \frac{1}{N_c}$ $\frac{1}{N_f} = \frac{F_{pp}}{N_{pp}} + \frac{F_{cc}}{N_{cc}} + \frac{F_{cp}}{N_{cp}} + \frac{F_{pc}}{N_{pc}}$	Superposition (plastic and creep)	Plastic shear and matrix creep	N_p = plastic failure, N_c = creep failure
6	Knecht and Fox	$N_f = \frac{C}{\Delta\gamma_{mc}}$	Matrix creep	Matrix creep only	c= 890%
7	Syed	$N_f = \left([0.022D_{gbs}] + [0.063D_{mc}]\right)^{-1}$	Accumulation of creep strain energy	Implies full coverage	D_{gbs} = accumulated equivalent creep strain/cycle, D_{mc} = accumulated equivalent matrix creep/cycle
8	Dasgupta	$N_f = \left(\frac{\Delta\overline{W}_{total}}{W_0}\right)^{1/k}$	Total strain energy	Joint geometry accounted for	ΔW_{total} = total strain energy density, W_0 = 0.1573, k = -0.6342

Table 3. Summary of solder joint fatigue models. [23]

#	Fatigue model	Equation	Model class	Coverage	Constants
9	Liang	$\bar{N}_f = C(W_{SS})^{-m}$	Stress/strain energy density based	Constant from isothermal low cycle fatigue tests	C and m = temperature dependent material constants, W_{ss} = stress strain hysteresis energy
10	Heinrich	$N_0 = 18083\Delta W^{-1.46}$ $N_0 = 7860\Delta W^{-1.00}$	Energy density based	Hysteresis curve	ΔW = viscoplastic strain energy/cycle
11	Darveaux	$N_{\alpha W} = N_{0s} + \dfrac{a - (N_{0s} - N_{0p})\frac{da_p}{dN}}{\frac{da_s}{dN} + \frac{da_p}{dN}}$	Energy density based	Hysteresis curve	a = total possible crack length, da=dN = crack growth, N_0 = crack initiation,
12	Pan	$C = N_f^*(a\dot{E}_p + b\dot{E}_c)$	Strain energy density	Hysteresis curve	C = strain energy density E_p = plastic strain creep energy density/cycle, E_c = creep strain energy density/cycle, d = 0.5 for solder (damage parameter)
13	Stolkarts	$N_f = \dfrac{1-(1-d_f)^{k-1}}{(k+1)L}$	Damage accumulation	Hysteresis curve and damage evolution	k = material constant, u-use t-test f-frequency
14	Noris and Landzberg	$AF = \left(\dfrac{\Delta\gamma_t}{\Delta\gamma_0}\right)^2 \left(\dfrac{f_0}{f_t}\right)^{1/3} e^{1414(1/T_0 - 1/T_t)}$	Temperature and frequency	Test condition versus use conditions	T = temperature, Φ_u/Φ_t = isothermal fatigue life ratio

1.6. Research Objectives - Motivation

For a long time multilayer ceramic substrates have been considered superior to PCB (Printed Circuit Board) when it comes to rough environments and functional integration. The trend to miniaturization and the requirements for new applications yield increasing thermal and mechanical load levels in the components. As the structure sizes decrease into the µm range they come close to the microstructure length scales typically found in ceramic materials, making it necessary to look even closer to failure modes. Multilayer components for communication and automotive applications will continue to shrink and increase their functionality at the same time. This will result in smaller structures and a higher metal to ceramic ratio. While miniaturization is the primary driving force in the communication business various other applications make use of the multilayer ceramic substrates ability to handle high electrical, thermal and mechanical loads. Thermal management, electrical functionality and high mechanical reliability under extreme load conditions are the standard requirements in these segments.

Since July 2006, electronic components have been mostly soldered lead-free, which sparked a wave of research in the area of solder materials for functional multilayer systems with respect to their thermal and mechanical properties [24][25]. The melting temperatures of the lead-free solder materials are around 220°C and allow a higher operating temperature up to 175°C. But a high strength of the solder joint reduces the thermal fatigue resistance during thermal cycling. The mechanical stability of the joint decreases when the melting temperature is approached [26].

Modern electronic systems (functional multilayer ceramic systems; FMCS) are in general composed of a mix of materials (ceramics, metals and polymers), which have very different electrical, thermal and mechanical properties. During processing and in service large temperature changes and the mismatch in thermal expansion coefficients (CTE mismatch) cause the development of significant internal stresses, which may limit the system reliability. Another cause for failing may also be mechanical stresses due to vibrations. In principle there are two main loading scenarios, which can take place in FMCS: thermal cycling (-40°C to 125°C) and mechanical loading. The first one is characterized by the time dependent creep behavior of the solder joint, where the accumulated strain per cycle will determine the number of cycles to failure [27]. The second type of loading is mainly based on the response of the interconnect to high cycle fatigue and high frequencies due to vibrations [6][28][29]. Due to an increasing need for functional multilayer ceramic systems in various applications, there are many thermo-mechanical stress- and mechanical reliability tests for multilayer ceramic components which have already been performed [30][31]. An overview of possible cracks and their sources can be found in the literature [32]. The FMCS lifetime depends on the ceramic component as well as on the solder joint. Depending on the thermal or mechanical stress there is a different crack path in the solder joint which is characteristic for the applied load [27]. To characterize the solder joints, with regard to lifetime and crack initiation, the experiment must be below the threshold for the crack initiation in the ceramic.

Fatigue damage mechanisms such as size, temperature and aging effects have to be studied to improve lifetime prediction models of lead-free solder joints. Especially the miniaturization and the associated change in the microstructure play a major role in the testing of lead-free solder joints [33]. The study of internal stresses (residual stresses) in solder joints and their changes with time is a key feature for their lifetime. The extended knowledge about thermo mechanical properties of lead-free solders shall contribute improved lifetime prediction models for a better understanding of solder joint properties in real structures. The results may allow the determination of the weak points in design and production of SMDs integrated in complex systems for mobile and automotive applications. The access to new design tools, which enable quicker and more reliability designs, with a reduction of rejection rates and better product quality would be conceivable.

CHAPTER 2
Tensile Properties and Microstructure of SnAgCu Lead-Free Solder Joints

2.1. Introduction

In the recent years SnAgCu (SAC) alloys have emerged as one of the mostly accepted solders among the lead-free solder compositions in microelectronic applications [34]. The knowledge of the complex thermo-mechanical response of miniaturized solder joints is of high significance for prediction of the reliability of the devices. Thermal and mechanical behaviors of the solder joints are primarily affected by the dimensional constraint and microstructural factors. Several experimental and theoretical investigations have shown that decreasing the solder gap size results in an increase in the tensile strength of the solder joints [5][35]. This geometrical constraint effect was explained by the build-up of a triaxial state of stress in thin joints subjected to tensile loading [6]. During the processing and the subsequent operational life the microstructure of the solder joints in microelectronic devices is subjected to a continuous modification. The relationship between the solder size/volume and the microstructure has also been the subject of a number of investigations [37][38]. However, systematic studies on the influence of size and microstructure of the intermetallic compound (IMC) layers between the solder and the substrate on the mechanical response of miniaturized solder joint are scarce.

In the present chapter the influence of microstructure and geometrical constraint on mechanical response of miniaturized lead-free solder joints was investigated. The focus of the study was the relationship between the solder gap size and thickness of the intermetallic compound (IMC) on tensile behavior of Cu/Sn3.5Ag0.75Cu/Cu solder joints with different ratios of IMC to the gap size. Independent of the IMC to solder gap thickness ratio a steady increase of tensile strength with decreasing gap size was observed. The variation of the IMC size was realized by different reflow times or heat treatments. An increased ratio of IMC thickness to the gap size results in a transition of the fracture mode from ductile to brittle and affects the strength of the solder joint. As the influence of many parameters has to be taken into account in detail, the experimental study of size effects in solder joints turns out to be a complicated topic.

2.2. Specimen Preparation

Model solder joints of Cu/Sn3.5Ag0.75Cu/Cu with gap sizes of 800 μm, 400 μm, 100 μm and 50 μm were prepared by using a commercial solder paste and copper strips with a purity of 99.9 % as substrate. The end faces of the copper strips were ground carefully with 600#, 1200# and 2500# SiC paper and were cleaned to prepare the soldering. A specially prepared sample holder allowed adjusting the gap size in the desired range. The samples were soldered in a reflow furnace (LPKF Zelflow RO4) by using a near-industrial reflow temperature profile. The melting point of the used Sn3.5Ag0.75Cu solder is 218°C. The resulting reflow temperature was chosen 25°C above the melting point of the used solder alloy to achieve an optimal soldering. The reflow oven temperature was 270°C with a total time of ~15 min to obtain a resulting peak temperature of 243°C of the sample. The heating profile is shown in Figure 2.1, in which the measured furnace temperature (red curve) and the resulting temperature on the sample (black curve) are plotted.

After the soldering and mechanical preparation steps, the dog bone shaped tensile samples with a soldered area of 3 x 2 mm² were mechanically polished to reveal their microstructure (Figure 2.2). The samples were then subjected to three different heat treatments to modify the microstructure of the joints: 1) stress relieving at 80°C for 3 h, 2) aging at 150°C/500 h and 3) aging at 150°C/1000 h. The soldering process and the subsequent aging of the samples resulted in the formation of different ratios of IMC to joint thickness in samples with different gap sizes. The aging temperature at 150°C was selected with respect to the maximum temperature occurring during the operation of the real devices. This aging step simulates the natural occurring aging of real devices in an accelerated way. It makes it possible to study the microstructural effects on mechanical properties.

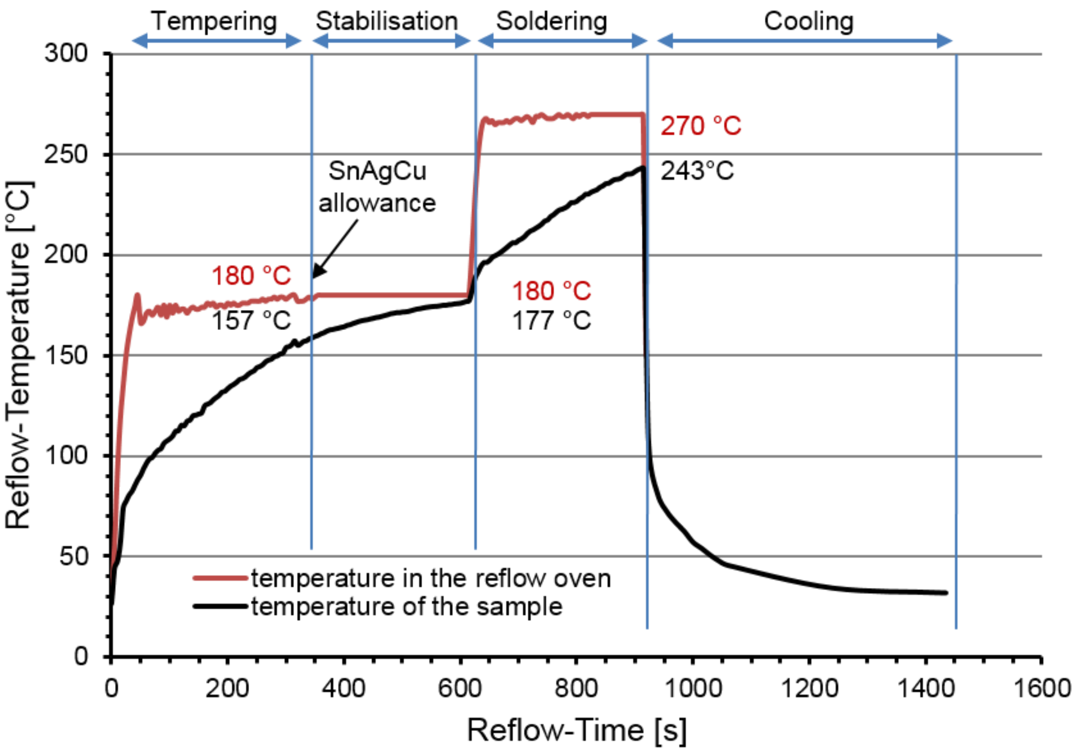

Figure 2.1. Actual heating profile measured during the soldering process (Sn3.5Ag0.75Cu).

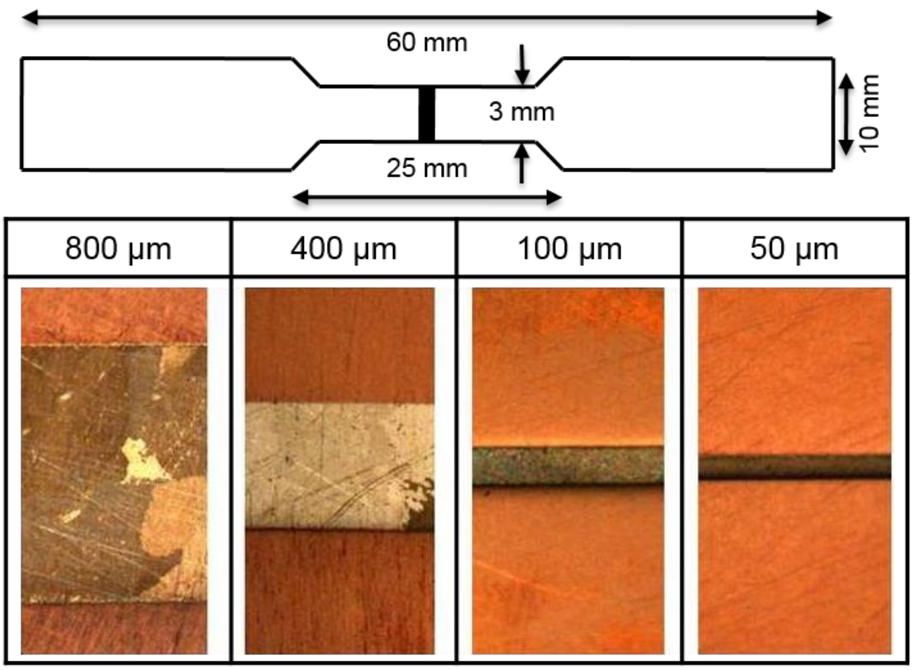

Figure 2.2. Schematic picture of the specimen geometry (Cu/Sn3.5Ag0.75Cu/Cu) and illustration of the fabricated solder gap size.

2.3. Microstructure of the SnAgCu System

The mechanical properties of the solder joints depend on the microstructure of the solder alloy. The challenge is to make a solder joint model, which has a comparable microstructure to that of a real device. The microstructure of a solder joint is mainly influenced by the geometry, the used substrate and especially the cooling profile of the soldering process. The ternary eutectic structure of Sn3.5Ag0.75Cu consists of a dendritic structure with a β-Sn matrix and fine Ag_3Sn particles as well as Cu_6Sn_5intermetallics at the interface of SnAgCu/Cu as shown in Figure 2.3. The main grain size of the β-Sn and the intermetallic Ag_3Sn increases by decreasing the cooling rate *dT/dt*, furthermore a faster cooling rate will produce a finer grain size (texture) [7]. This relationship is used to tune the microstructure of the solder model joint into a comparable structure of commercially used solder joint.

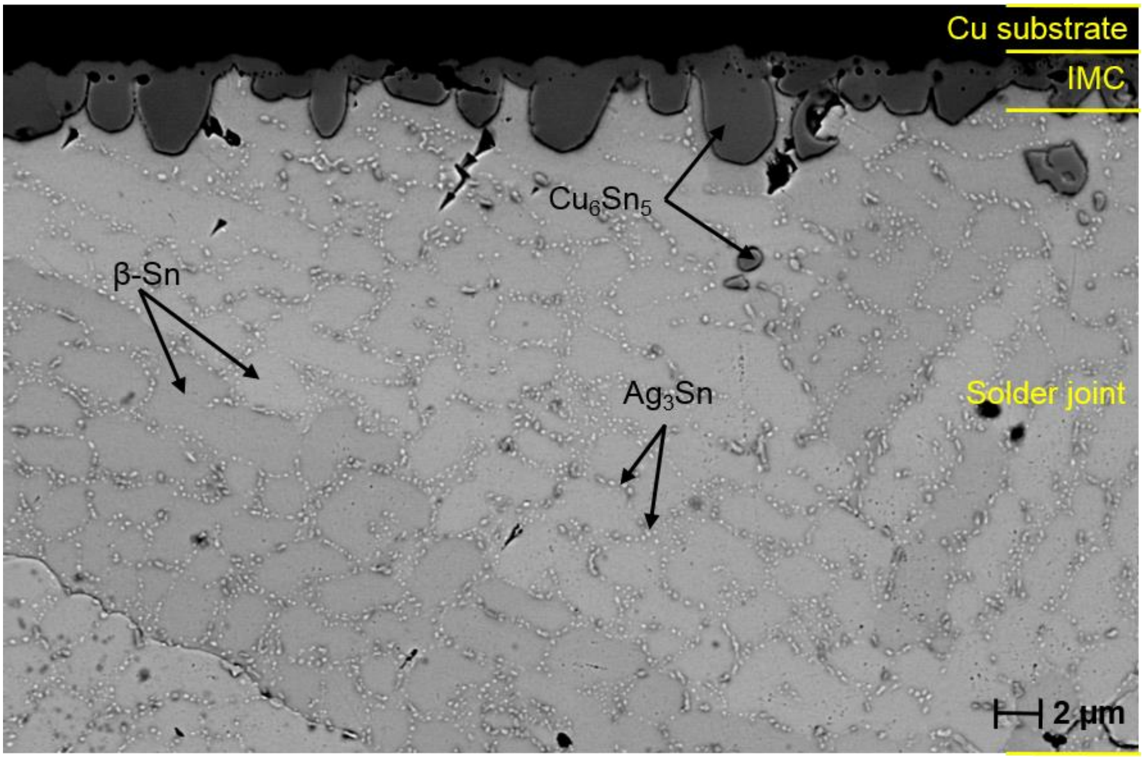

Figure 2.3. Microstructure of a 200 µm Sn3.5Ag0.75Cu gap.

2.3.1. Microstructure for Different Solder Volumes and Aging Time

The microstructures of the fabricated solder joints of various thicknesses subjected to heat treatment at 80°C/3h, 150°C/500h and 150°C/1000h are shown in Figure 2.4.

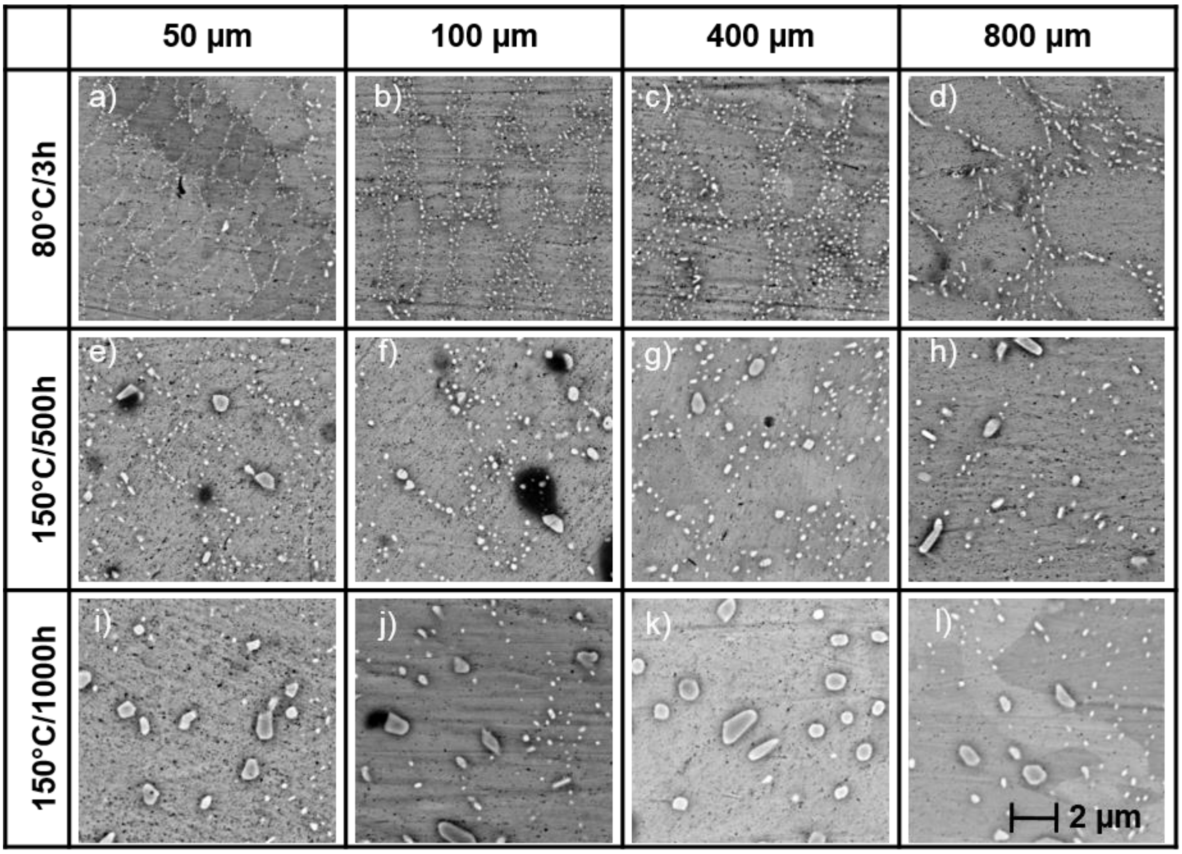

Figure 2.4. Microstructural changes of solder gaps in the range of 50µm up to 800µm subjected to (a-d) 80°C/3h, (e-h)150°C/500h and (i-l) 150°C/1000h heat treatments.

In the case of the solder gaps heat treated at 80°C/3h, β-Sn primary grains are surrounded by a fine eutectic Ag_3Sn network. With increasing solder gap size (volume) a continuous coarsening of the β-Sn grains and Ag_3Sn particles is observed due to the slower cooling rate in the joints with a higher solder volume (Figure 2.4a-d) [7]. Long time thermal exposure at 150°C resulted in a coarsening of the β-Sn phase and redistribution and coarsening of the Ag_3Sn particles for all solder joints with different thicknesses (Figure 2.4e-h). At this stage further formation of Cu_6Sn_5 particles in the solder bulk is promoted due to diffusion of the Cu from the substrate. After 1000 hours of aging the solders showed a rather similar microstructure independent of the size/volume of the joints (Figure 2.4i-l). However, aging leads to a rather considerable grain growth resulting in a lower number of grains across the cross section of thinner joints. Due to the coarsening of the microstructure and diffusion of the intermetallics during the heat treatment at higher temperatures and longer times, a reduction of tensile properties of the joint is expected.

2.3.2. Microstructure Evolution of the IMC Layer

The ternary eutectic structure of Sn3.5Ag0.75Cu consists of Cu_6Sn_5 particles in the solder bulk as well as Cu_6Sn_5 intermetallic at the interface of SnAgCu/Cu. During the reflow process of the SnAgCu/Cu joint system, Cu_6Sn_5 forms first at the interface and Cu_3Sn will form after heat treatments between Cu and Cu_6Sn_5 by solid-state reaction. Formation of IMC layers at the interface is an indication of a good connection between solder and the used pad. Moreover, further growth of Cu_6Sn_5 and Cu_3Sn intermetallic phase was observed at the interface between solder and substrate after heat treatments at 150°C as shown in the phase diagram of Figure 2.5.

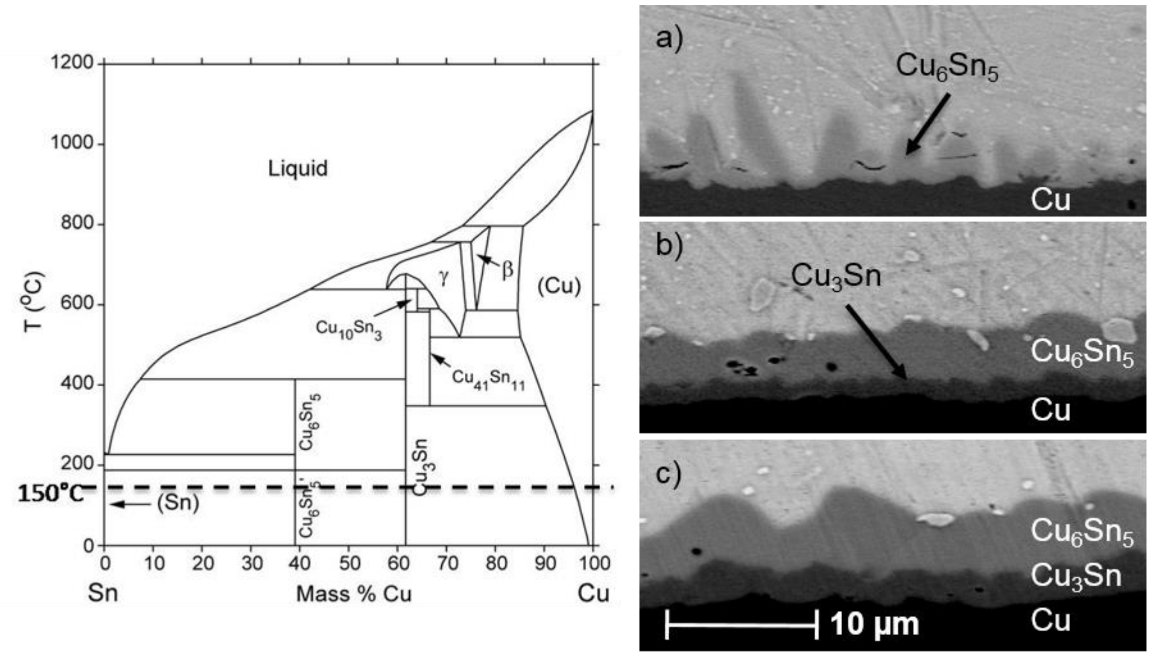

Figure 2.5. Sn-Cu Phase diagram with corresponding formation of interfacial IMCs in the solder joint subjected to heat treatment at (a) 80°C/3h, (b) 150°C/500h and (c) 150°C/1000h.

Increased thermal exposure resulted in an increase of the Cu_6Sn_5 thickness from 2.5 µm to 5.2 µm and of the Cu_3Sn layer from 0 µm to 3.1 µm from the original state and after an aging time of 1000h, respectively. The Cu_6Sn_5 IMCs show scallop-type morphology after the reflow and heat treatment at 80°C for 3h. The long time aging process at 150°C results in flattening of the IMC grains and transformation to a planar morphology (Figure 2.5a-c). The formation of interfacial IMCs in the solder joints is also highly dependent on the solder volume and the concentration of the elements in the solder that are required for interface phase formations. The growth kinetics of Cu_6Sn_5 and Cu_3Sn depends on the mass transport through the resulting layer and the reactions at the interface [39]. The relationship between the IMC growth *Y* and square root of time is given by,

$$Y = \sqrt{kt} \tag{11}$$

where *k* is the reaction rate constant and *t*, the aging time. The reaction rate coefficient is given by an Arrhenius type equation,

$$k = k_0 e^{-\left(Q/_{RT}\right)} \tag{12}$$

where k_0 is the frequency factor of IMC formation; *Q*, the activation energy; *R*, the gas constant (8.314 J/mol K and *T*, the absolute temperature in Kelvin (K).

The relationships between the thickness of the Cu_3Sn, the Cu_6Sn_5 and the total intermetallic layer and the square root of aging time are shown in Figure 2.6, respectively. The measured IMC layer thicknesses over the aging time are listed in Table 4. The increased growth rate of the Cu_3Sn phase in comparison with the Cu_6Sn_5 phase is due to the diffusion rate of copper into the solder joint from both sides of the substrate promoting the formation of Cu_3Sn. The activation energy for growth of Cu_6Sn_5 and Cu_3Sn were found to be 73.5 ± 1.5 kJ/mol and 120.2 ± 0.5 kJ/mol, respectively. These values were calculated by using the frequency factors of 4.3×10^{-12} for Cu_6Sn_5 and 3.3×10^{-3} for Cu_3Sn as taken from the literature [40]. The calculated values are approximately in the range of reported activation energies of 64.6–83.9 kJ/mol for Cu_6Sn_5 and 74.3–103.3 kJ/mol for Cu_3Sn [40][41].

Table 4. Measured IMC layer thicknesses over the aging time.

Sqr Time [h^1/2]	Total IMC [µm]	Cu_3Sn [µm]	Cu_6Sn_5 [µm]
0.0	2.6	0.0	2.6
22.4	6.5	2.3	4.2
31.6	8.4	3.1	5.3

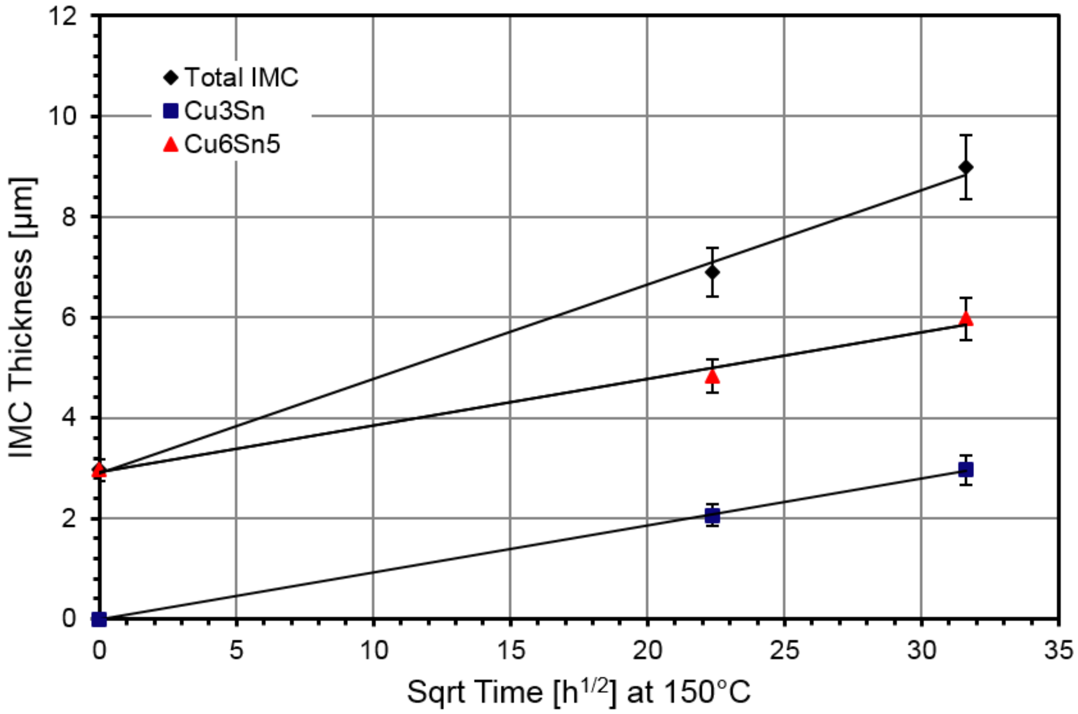

Figure 2.6. Growth of intermetallic compounds with respect to the aging time at 150°C.

The relationship between IMC growth and solder gap thickness is given in Figure 2.7. The total IMC thickness decreases with reduction of the solder gap thickness, based on the strong decrease of the Cu_6Sn_5 growth in comparison to the higher growth rate of Cu_3Sn. Both IMC formations are depending on the diffusion of Cu to the Sn/Cu_6Sn_5 and Cu_6Sn_5/Cu_3Sn interfaces, where Cu_6Sn_5 grow towards the Sn layer and Cu_3Sn grow towards the Cu_6Sn_5 layer. It takes much longer for Cu atoms to diffuse to the Sn/Cu_6Sn_5 interface than to the Cu_6Sn_5/Cu_3Sn interface. Furthermore the formation of Cu_3Sn is promoted by a higher content of Cu, as a result of reduction in the solder volume with constant soldering area (Cu). [40]

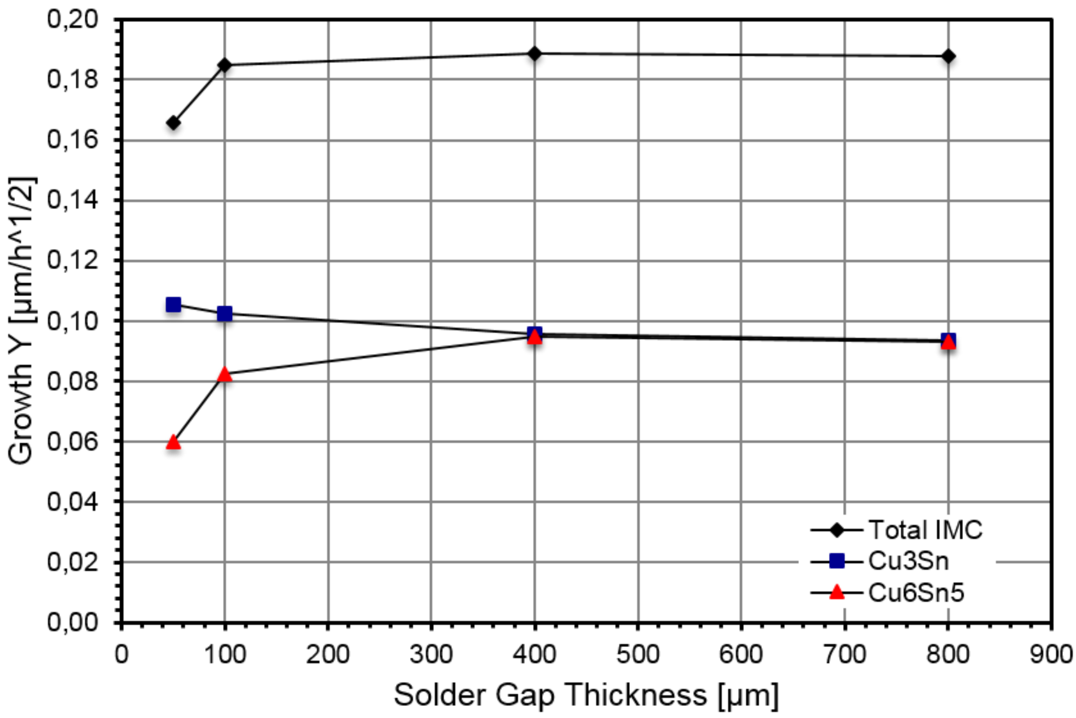

Figure 2.7. Calculated Growth kinetics for the IMC layer depending on the produced gap size and heat treatment at 150°C.

The dependency of the IMC thickness layer on the solder gap size and aging conditions are given in Figure 2.8 and Figure 2.9. Figure 2.8 shows the relationship between the solder gap size and the IMC thickness depending on the aging time. The absolute IMC layer thickness increases with increasing the solder gap size but the IMC layer proportion has an inverse relationship with solder gap size as shown in Figure 2.8. As example for a solder gap size of 50 µm the interfacial IMCs proportion was increased from the initial value of 9.5% to 24.0% at 500h and finally to 30.5% after 1000h of heat treatment at 150°C. The reason is the small volume of the solder in thinner solder joints and the faster cooling rate, which affects the formation of the IMC layer. Figure 2.9 shows the relationship between the $Cu_6Sn_5$and the Cu_3Sn phases with the gap size. While a steady increase in the Cu_6Sn_5layer is observed the thickness of the Cu_3Sn phase is reduced with increasing gap size. The higher rate of formation of the Cu_3Sn phase in smaller solder joints is due to the higher concentration of dissolved copper in thinner joints. The solder volume decreases, but the Cu diffusion from the boundary remains constant, which is also described by the change of the growth coefficient.

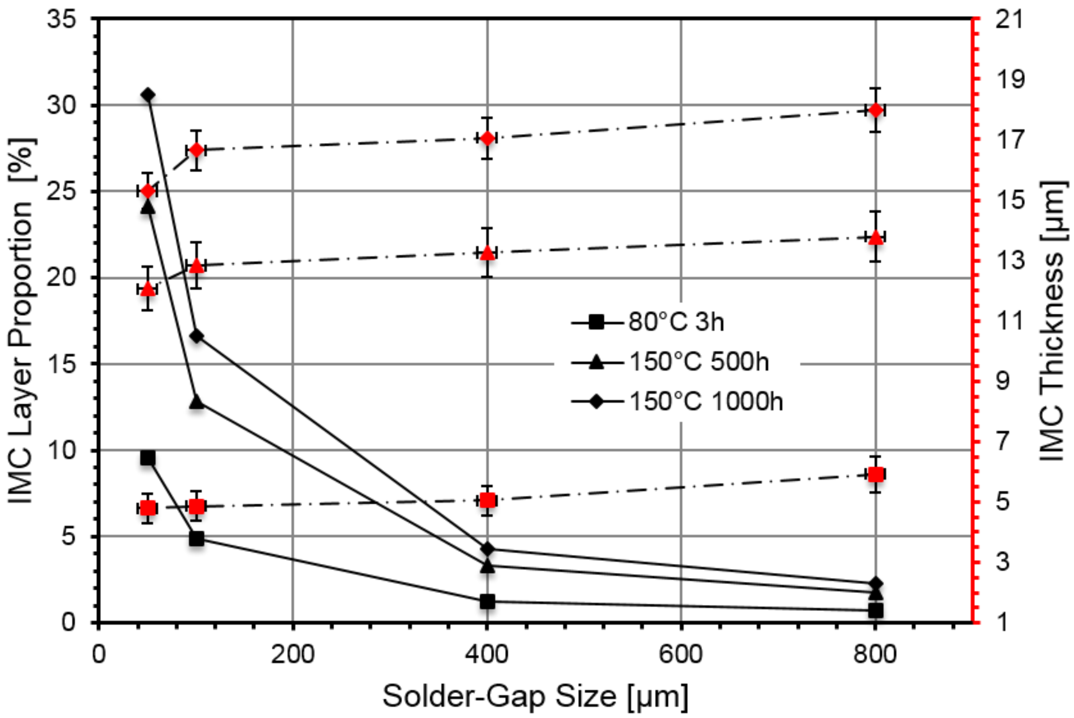

Figure 2.8. Interfacial IMCs layer proportion of different gap sizes with the corresponding totally IMC layer thickness for different heat treatments.

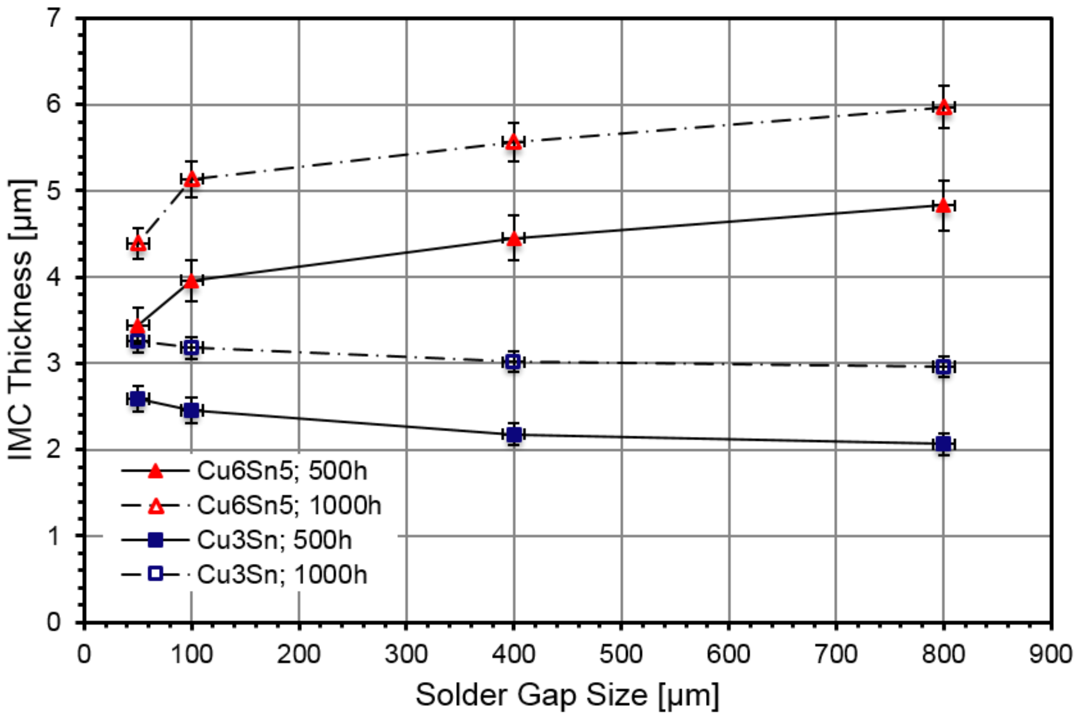

Figure 2.9. Relationship between Cu_6Sn_5 and Cu_3Sn layer thicknesses to the solder gap size after aging at 150°C/500h and 150°C/1000h.

2.4. Tensile Properties of the Cu/Sn3.5Ag0.75Cu/Cu joints

2.4.1. Measurement of Tensile Properties

Tensile experiments were performed using the µ-strain tensile machine ME 30-1 with a crosshead stroke resolution of 0.04 µm and a minimum load resolution of 10 mN of the 500 N load cell (TCA 50kg). The strain was measured by a non-contacting laser speckle video extensometer with a gauge length of about 20 mm and a strain resolution of 10^{-5}. The principle of the video extensometer is based on the evaluation of speckle patterns that are reflected from the sample surface by coherent laser light (660 nm wavelength). The extensometer automatically detects the light-dark transitions on the sample surface and evaluates them by using a fast Fourier transform (FFT) correlation analysis [42]. The stress-strain curves were plotted by using the initial solder gap size of each sample assuming the Cu substrate as rigid in the measured region. Figure 2.10 shows the used tensile setup with a clamped Cu/Sn3.5Ag0.75Cu/Cu solder joint sample.

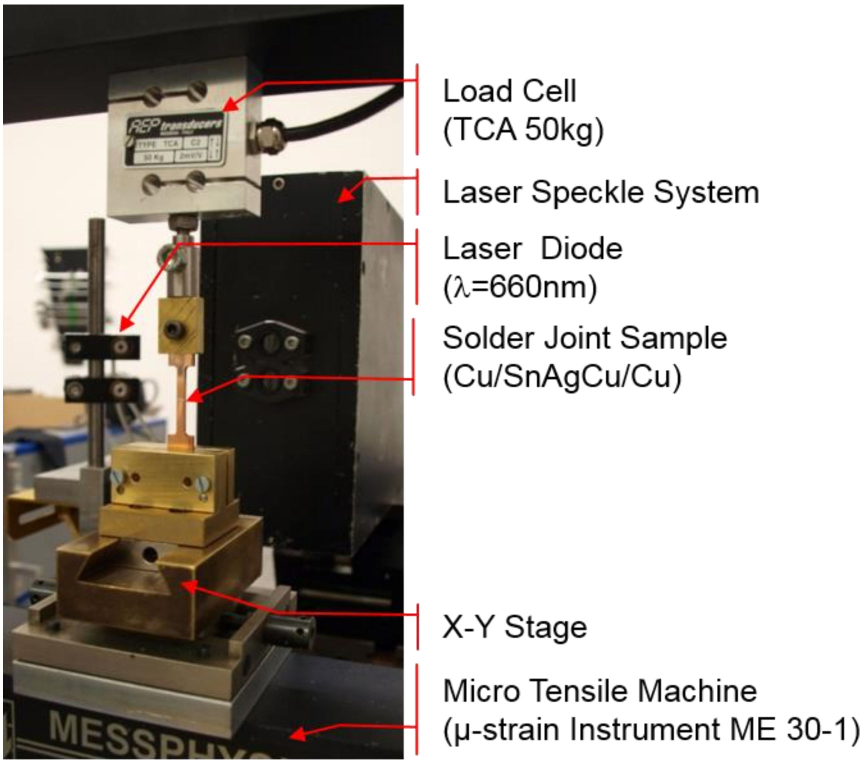

Figure 2.10. Tensile experimental setup consisting of micro tensile machine, 500 N load cell, x-y stage and laser speckle video extensometer with 600 nm laser diodes

The tests were performed displacement controlled on two series of solder joints at room temperature. The first series of tests are conducted using a fixed crosshead speed of 0.2 mm/min for all gap thicknesses. The second series of tests are conducted using a strain rate of $3.5 \times 10^{-3}\ s^{-1}$. The strain rate is referred to a solder gap thickness of 960 µm and is given by,

$$\dot{\varepsilon} = \frac{1}{L}\frac{dL}{dt} = \frac{v}{L} \tag{13}$$

where v is the crosshead velocity and L, the gage length.

2.4.2. Tensile Properties as Function of Solder Gap Thickness

Typical stress-strain curves for Cu/Sn3.5Ag0.75Cu/Cu solder joints with gap sizes of 960 µm, 406 µm, 96 µm, and 58 µm are plotted in Figure 2.11 showing an increase in tensile strength and a decrease in fracture strain with decreasing gap size. The results are in agreement with previous studies on the constraint effect in lead-free solder joints by [35][43][44]. The constraint effect is related to a geometric effect of the joint and is explained by a triaxial state of stress in the interface between substrate and joint which occurs in thin joints [6]. In a study by Hegde et al. [45], this triaxial state of stress was studied and explained in the case of Sn3.8Ag0.7Cu solder joints. During plastic deformation, the solder joint tends to keep its volume constant which results in a 3D stress state defined as the triaxiality ratio with $R_t = {}^{\sigma_h}/_{\sigma_m}$, where σ_h is the volume average of hydrostatic stress in the solder joint and σ_m is the volume average of von Mises or equivalent stress in the solder joint. A decrease of the gap size results in an increase of the normal stress and the hydrostatic stress in the solder results in an increased tensile strength in thinner solder joints. The stress field becomes triaxial in thin solder joints due to the size effect, but the triaxiality decreases when the gap size becomes thicker.

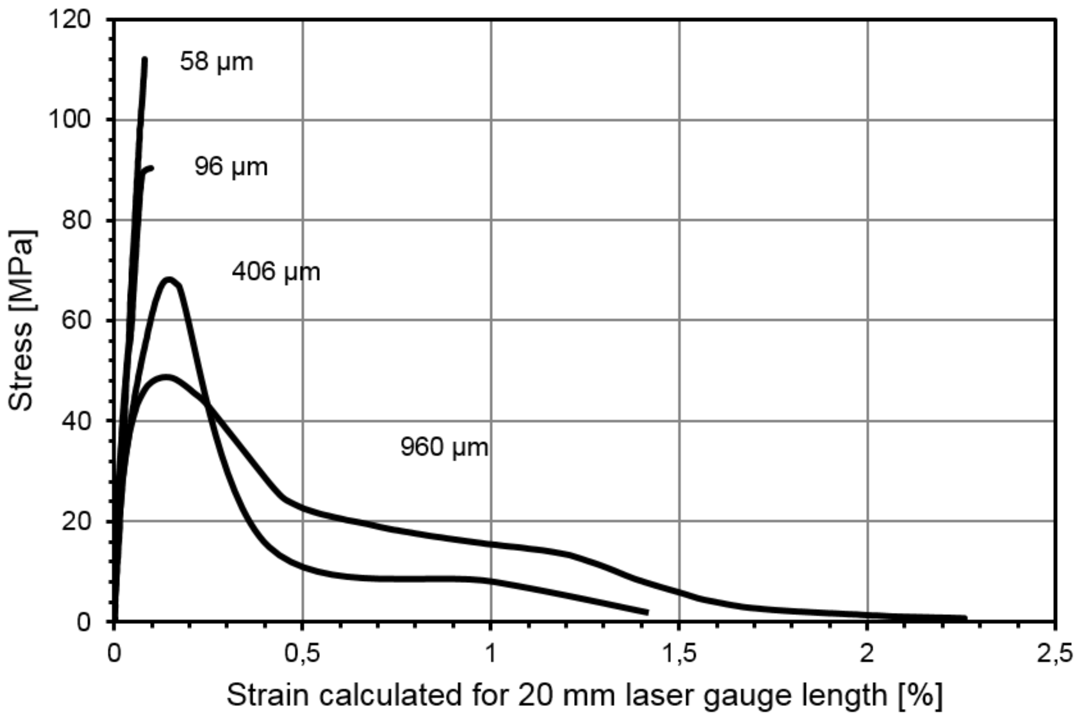

Figure 2.11.Stress-strain curves of Cu/Sn3.5Ag0.75Cu/Cu solder joints with various thicknesses.

Fracture surface analysis of several samples showed a relationship between the fracture strain of the solder and the percentage of voids in the solder volume. Voids in the solder joints are usually formed during the soldering process due to an inhomogeneous flux distribution in the solder paste and outgassing of the flux. These voids were homogeneously distributed in the solder joints and generally lead to a reduction of about 14% of the contact area. The new stress distribution in the solder volume increases the plastic behavior of the solder gap, which resulted in a higher fracture strain. Figure 2.12 shows the dependencies of tensile strength and corresponding fracture strain (a) with no defects and (b) with void formation on solder gap thickness. Higher fracture strain was observed especially for larger solder gaps >200 µm. The fracture strain was increased from 0.14% up to 0.57% for a 400 µm and 0.16% up to 0.94% for a 800 µm solder gap by void formations in the solder volume. The stress level was decreased around 10 MPa for thicker solder gaps. Though in principle void formation is known to reduce the quality of the solder joints [46][47], however these results show that presence of homogeneously distributed voids in the solder leads to a higher ductility of the joints. This effect may be related to the fact that the presence of voids in thicker solder joints results in a redistribution of the stress concentration from the interfacial region to the bulk of the solder with a higher capacity of plastic deformation. Final fracture occurs due to coalescence of the present voids, similar to that occurring in bulk solder subjected to tensile loading. A stress distribution around the void formation is assumed which decreases the UTS level but promotes the ductility, which results in a higher fracture strain. This can be attributed mainly to a smaller cross-sectional area in the bulk than in the interface region, confirmed by elastic-plastic FEM analysis [48].

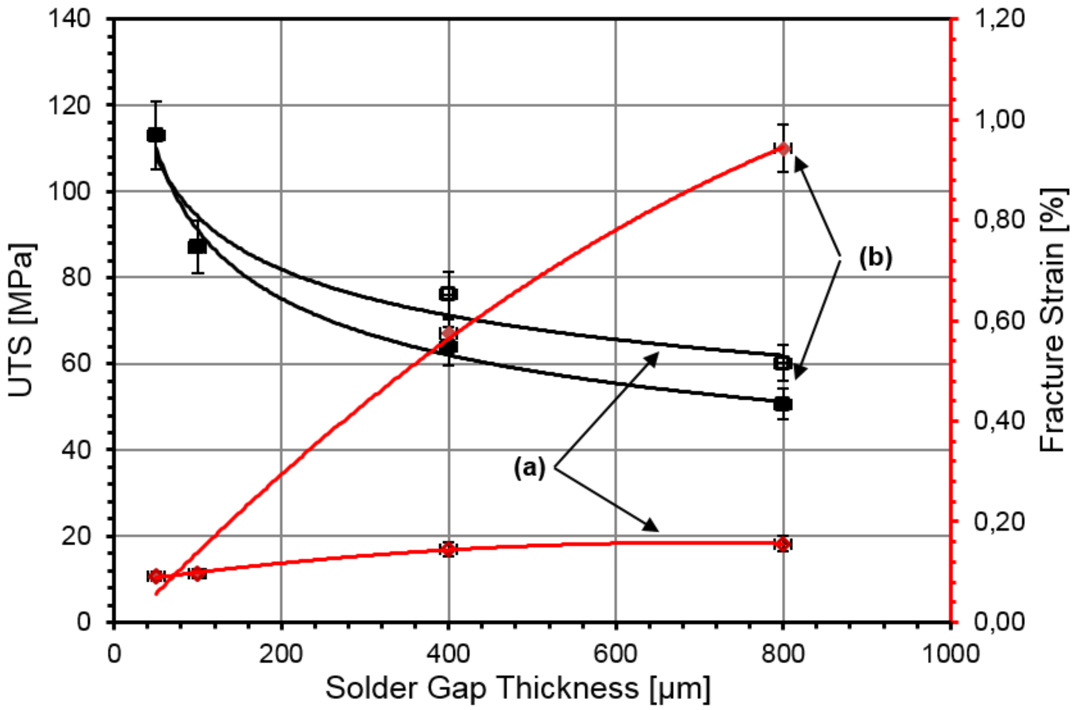

Figure 2.12. Dependencies of tensile strength and fracture strain on solder gap thickness. a) fracture strain behavior without defects, b) fracture strain with voids in the solder due the soldering.

Figure 2.13 shows the values of UTS as a function of solder gap thickness for two series of samples. The data points marked with circles correspond to a constant cross head speed of 0.2 mm/min for all samples and the second data set of points (diamonds) correspond to a constant strain rate of 3.5 x 10^{-3} s^{-1} for each solder gap size. Comparing the corresponding strain rate for a joint of about 1 mm with that of 50 µm, a constant cross head speed of 0.2 mm/min results in a 16 times higher strain rate for the thinnest samples. However, the results show a minor strain rate dependency of the stress-strain response of the solder joints under the present test conditions. In a study by Kim et al. [7] on bulk Sn3.5Ag0.7Cu solders a 100% increase of stress values was observed, independent of the microstructure, for tests conducted at strain rates between 10^{-5} s^{-1} and 10^{-1} s^{-1}. In this study the insignificant strain rate dependency of the solder joints in the range of 3.5 x 10^{-3} s^{-1} (for 960 µm gap size) and 6.6 x 10^{-2} s^{-1} (for 50 µm gap size) can be related to a lower creep rate in thin solder joint [49].

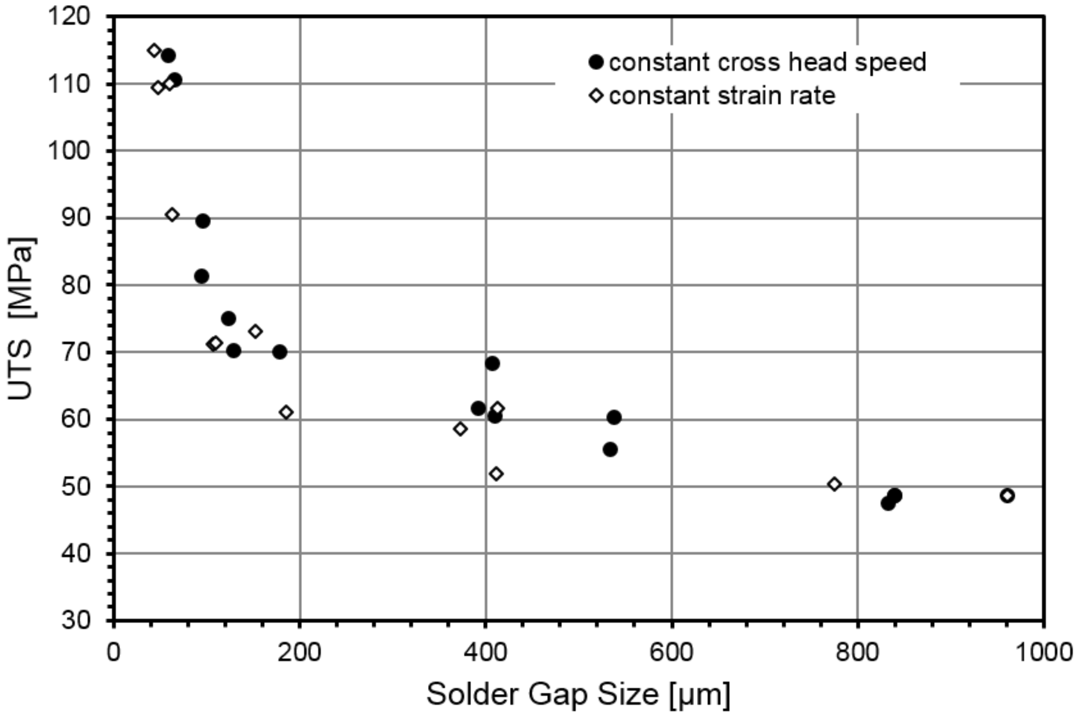

Figure 2.13. Strain rate dependence of the ultimate tensile strength as a function of solder gap thickness.

It was reported that an increase of up to 10^{-4} s^{-1} or a decrease down to 10^{-1} $s^{-1}$of the strain rate leads also to change of the fracture behavior. A combination of strain rate dependency and variety of IMC microstructure on failure mode was demonstrated by An et al. [50] and corresponds well with the obtained results in this work. The failure mode of Cu/Sn3.0Ag0.5Cu/Cu solder joints changes from a ductile fracture in the bulk solder to a brittle fracture in the IMC layer by increasing the strain rate. Therefore a ductile failure mode is expected for thick solder gaps at a strain rate of 10^{-3} s^{-1}. The plane view of the tested non-aged solder joints with a gap size of 50 µm, 100 µm and 800 µm and their respective fracture surfaces is shown in Figure 2.14.

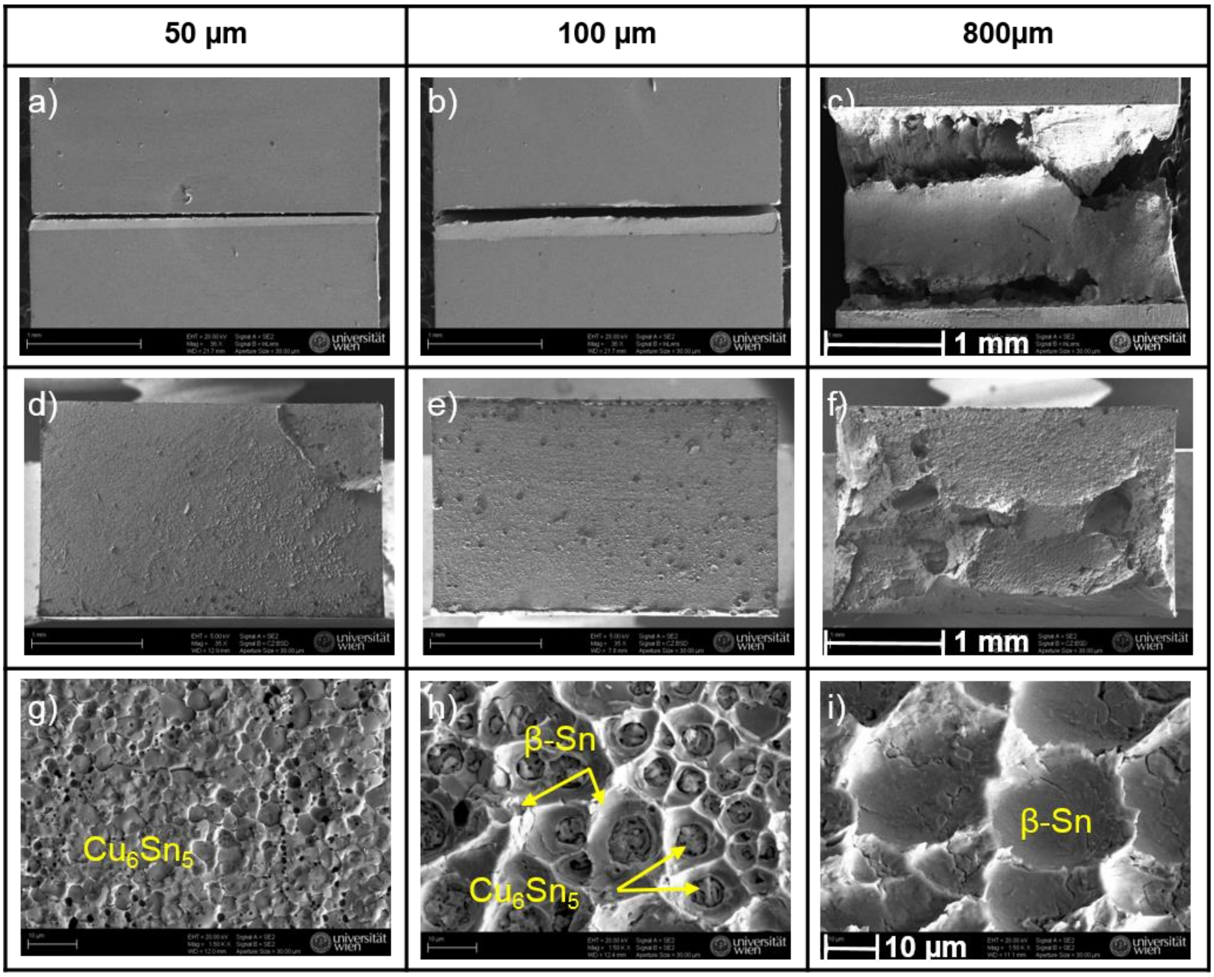

Figure 2.14.Plane view of the tested non-aged solder joints with a gap size of 50 µm, 100 µm and 800 µm (a-c) and their respective fracture surfaces (d-i).

Fracture surface analysis of the tested samples showed three different crack patterns with a transition from a brittle to ductile failure with increasing the solder gap size. For solder joints with a gap size in the range of 50 µm up to 100 µm the crack initiates and propagates in the Cu_6Sn_5 IMC layer resulting in brittle interfacial failure (Figure 2.14 a, d and g). Above this thickness the cracks initiate near the interface and grow along the Sn/Cu_6Sn_5 interface as shown in Figure 2.14 b,e and h. Increasing the solder gap size results in a shift of the crack path from the interfacial region to the bulk of the solder. For solder joints with a gap thickness of above ~400 µm, failure occurred due to crack initiation and necking inside the bulk of the solder. Due to the high stress concentration in the interfacial region cracks were also often observed near the interface of the solder to substrate at the final stage of tensile test (Figure 2.14 c, f and i). The resulting failure can be seen as a mixed failure mode between brittle IMC fracture and ductile solder fracture.

2.4.3. Effect of the IMC Microstructure on Tensile Properties

Long time thermal exposure at 150°C (500h and 1000h) results in a reduction of tensile strength and an increase of elongation of the solder joints. The ultimate tensile strength (Figure 2.15) and fracture strain (Figure 2.16) of aged solder joints show a gap size dependency similar to the samples heat treated at 80°C/3h. The stress-strain response of the aged samples depends on several factors. Thermal aging results in softening of the solder material due to the microstructural changes and grain growth. In the meantime the interfacial Cu_3Sn layer is also formed and an increase of the total thickness of IMC layer is observed. The growth of IMCs contributes to a higher proportion of high-strength but brittle phases in the solder composite. Thus for the aged samples a combined effect of softening of the bulk solder, limited number of grains across the thickness together with the hardening effect of the interfacial IMCs determines the tensile properties of the solder joints. The brittle nature of the intermetallic compounds and the high proportion of IMCs layers in very thin solder joints may contribute to an early fracture and a reduction of the tensile strength and elongation due to a higher rate of degradation, cracking and voiding of the interface [51].

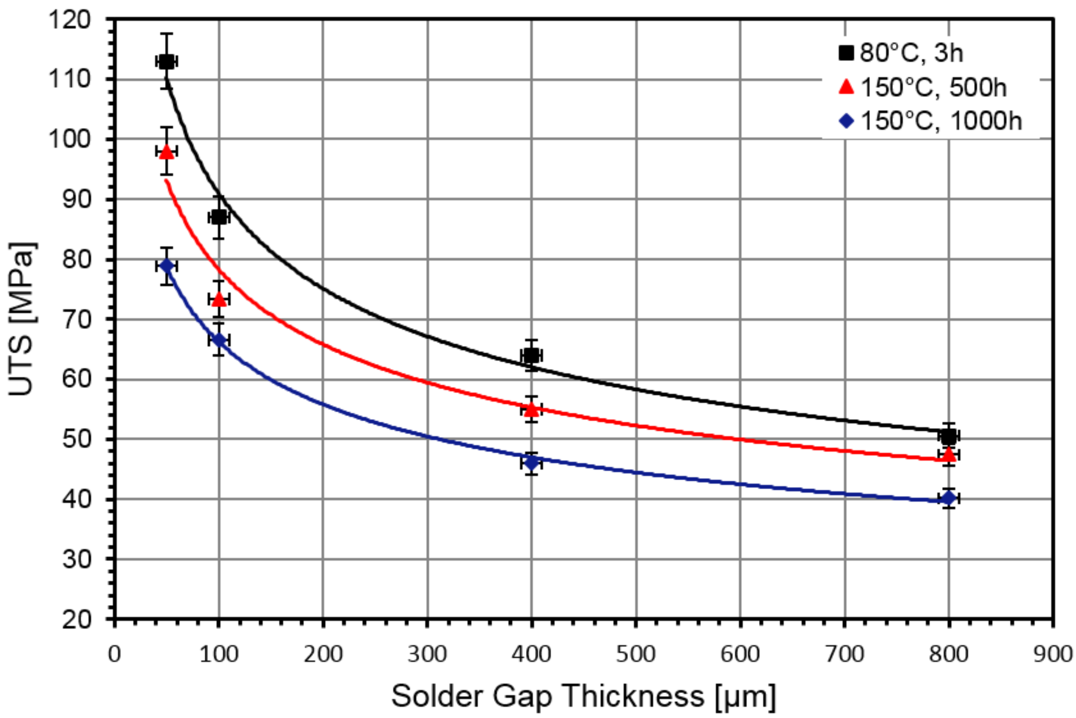

Figure 2.15. Dependency of tensile strength on solder gap thickness for different aging conditions.

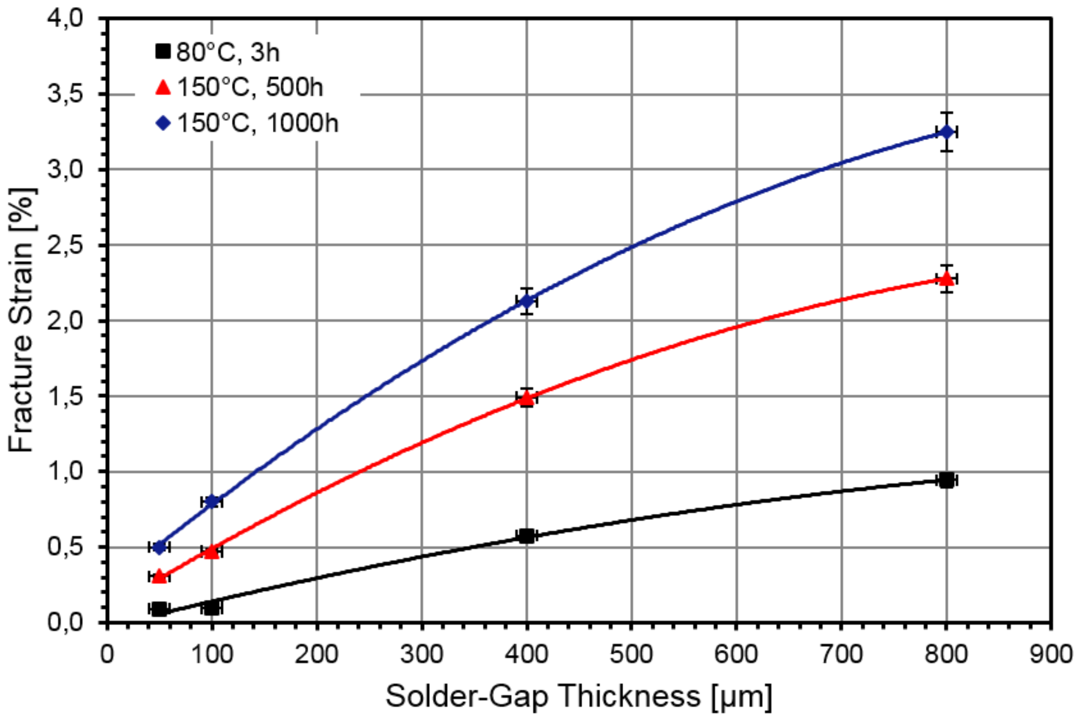

Figure 2.16. Dependency of fracture strain on solder gap thickness for different aging conditions.

In this study decreasing the gap size resulted in a steady increase of tensile strength for the aged samples with a parallel downwards shift relative to the reference solder joints (Figure 2.15). However a more prominent effect of aging on increase in elongation was observed for the thicker solder joints as shown in Figure 2.16. This effect may be related to the limited number of grains resulting in an additional restricted plastic deformation in thinner joints.

Tensile tests were conducted on bulk Cu samples to determine the influence of the Cu substrate on the stress-strain behavior of solder joints. The tests were performed under the same conditions (strain rate and aging conditions) as those used for the solder joint samples. Independent of aging conditions, the yield stress of bulk Cu samples is all above 190 MPa as shown in Figure 2.17. Aging at 150°C up to 1000h resulted in a slight decrease yield and tensile strength and a reduction of about 50% of the fracture strain of the bulk Cu samples (Figure 2.17). The reduction from 270 to 260 MPa has no influence on the measured UTS for solder joints. Even the thinnest solder joints fail at a maximum stress of about 115 MPa, which is still in the elastic region of the Cu stress-strain curve.

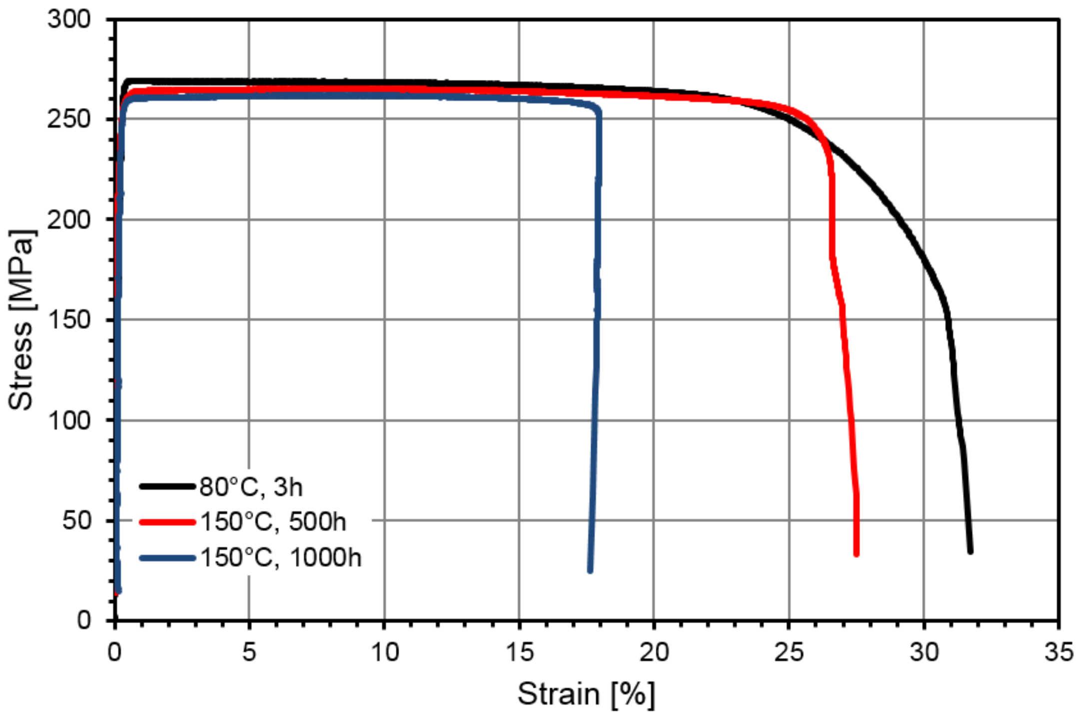

Figure 2.17. Stress-strain curves of bulk Cu samples for different aging conditions.

The aging process affects the fracture behavior of thin solder joints due to the interfacial IMC growth. Figure 2.18 shows the dependency of the fracture type on the IMC morphology for a solder gap size of about 100 µm subjected to different heat treatment conditions. The geometry of the IMC interfacial layer plays a major role in the type of failure. For non-aged samples the protruding regions of scallop shaped Cu_6Sn_5 phase, act as a source of stress concentration as shown in Figure 2.18a-a´ resulting in a fracture surface consisting of broken IMC grains surrounded by solder dimples. Increase in the thickness and the change of IMC shape to a planar morphology leads to crack formation and propagation inside the Cu_6Sn_5, as shown in Figure 2.18b-b´ and c-c´. In this study failure occurred mainly in the Cu_6Sn_5 layer and cracks leading to fracture were not identified in the Cu_3Sn layer. This effect is probably due to the higher internal stresses of Cu_6Sn_5 and the difference in the fracture toughness of the two phases. The fracture toughness of Cu_6Sn_5 and Cu_3Sn are reported to be 2.80 MPa $m^{1/2}$ and 5.72 MPa $m^{1/2}$, respectively [52].

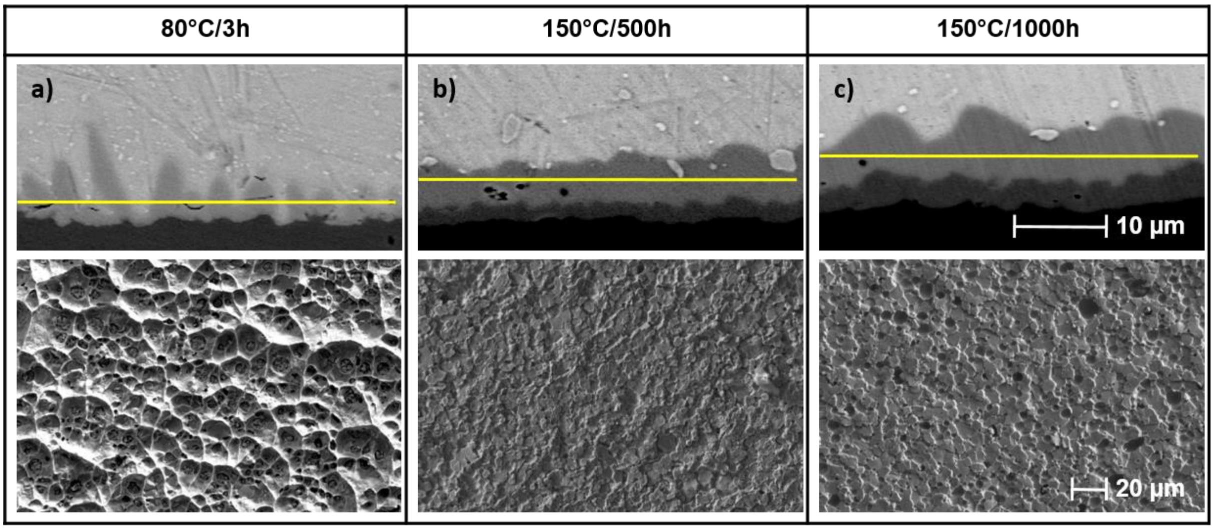

Figure 2.18. Dependency of the fracture type on the IMC morphology for a solder gap size of about 100 µm subjected to (a) 80°C/3h, (b) 150°C/500h and (c) 150°C/1000h heat treatments.

In general, the tensile behavior and failure of the miniaturized solder joints is attributed to the microstructural and constraint effects. The investigations show that in case of non-aged solder joints with similar microstructure and IMC shape the constraint effect plays the dominant role in the tensile response and fracture behavior. Increasing the thickness of the solder joint leads to enhanced plastic deformation in the solder volume and results in a mixed failure mode with ductile type of fracture inside the solder and IMC/solder fracture. With decreasing the solder volume, the cross contraction is restricted and the stress is concentrated in the interfacial region resulting in cracking and failure near the IMC/solder interface. After long time exposure the strength of the joints and the fracture mode is mainly related to the microstructure of the solder joint especially the proportional thickness and shape of the interfacial IMC layer. It was found that a high ratio of IMC layer/gap size (solder volume) in thin joints results in a higher probability of failure as a result of the dominant brittle fracture mode.

2.5. Tensile Properties as Function of Testing Temperature

The influence of temperature on the UTS of Cu/Sn3.5Ag0.75Cu/Cu solder joints with different gap sizes between 50 µm and 800 µm are plotted in Figure 2.19. The solder joints were tested at 80°C and 125°C with the prospect to use the results as input for the stress relaxation in the next step (Chapter 3). The plot of UTS versus solder gap thickness shows a decrease of the UTS with increasing testing temperature, with a 28% to 43% reduction of the UTS for thicker and thinner solder joints respectively. High temperature makes the solder become softer, with regard to the homologous temperature T_h of 0.7 (80°C) and 0.8 (125°C).

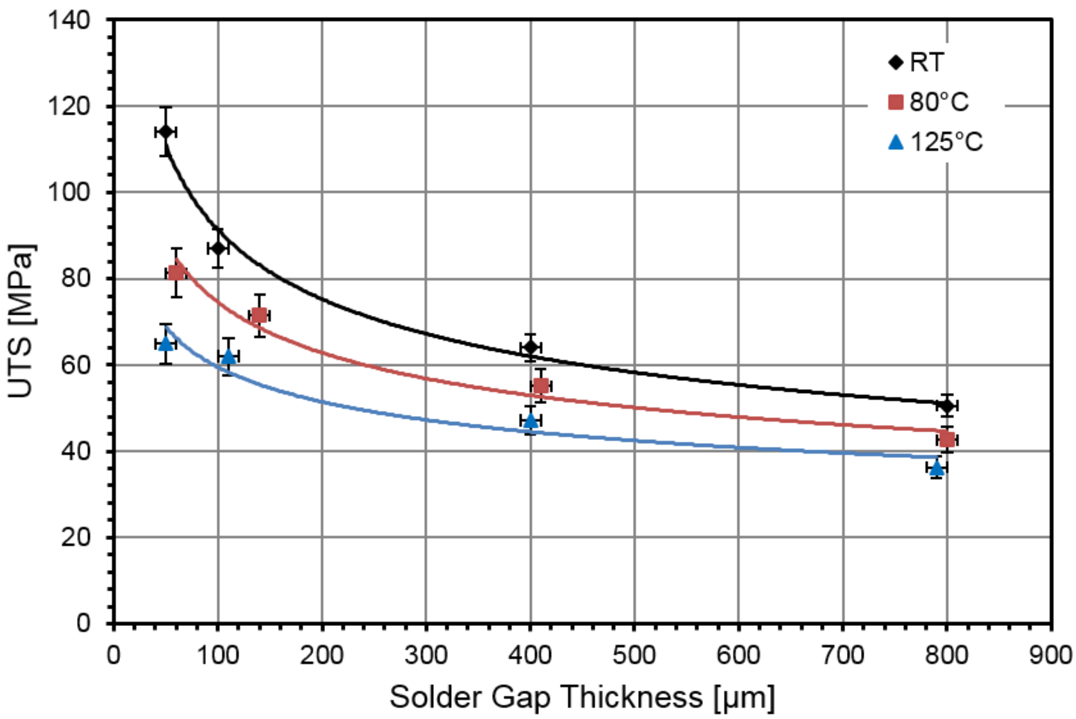

Figure 2.19. Effect of temperature on tensile strength of Cu/Sn3.5Ag0.75Cu/Cu solder joints with different gap thicknesses at RT, 80°C and 125°C.

The solder becomes more ductile and softer when testing temperature increases. A further reduction of the UTS is caused by aging, which was shown in the previous chapter. The effect of temperature in combination with aging at 150°C for 500h and 1000h on tensile strength is shown in Figure 2.20 at 80°C and in Figure 2.21 at 125°C. Aged samples tested at 80°C allow a further reduction in UTS with 9.9% to 18.5% for thicker and thinner solder joints relative to the reference (nonaged, tested at RT). The reduction due to the aging is limited by the size effect and the high proportion of IMCs layers in thinner solder gaps. However, the influence of the microstructure is reduced by testing at 125°C compared to 80°C. The downwards shift of the UTS level is only 14.6% to 7.6% for thicker and thinner solder joints indicating the impact of homologues temperature on the tensile response of solder joints. Figure 2.22 gives an overview over the effect of test temperature (color) and aging at 150°C (area) on the UTS as a function of the solder gap thickness. There is more than one way to achieve certain UTS reductions, which were described by the overlap of temperature and aging effect.

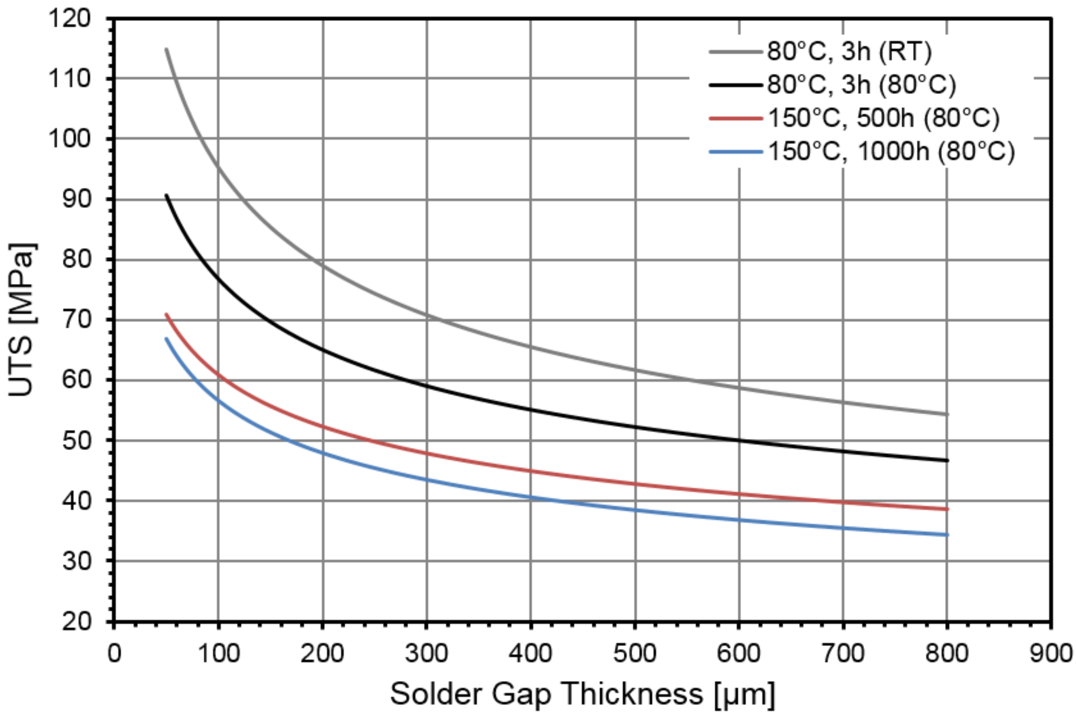

Figure 2.20. Dependency of tensile strength on solder gap thickness at 80°C for different isothermal aging times at 150°C.

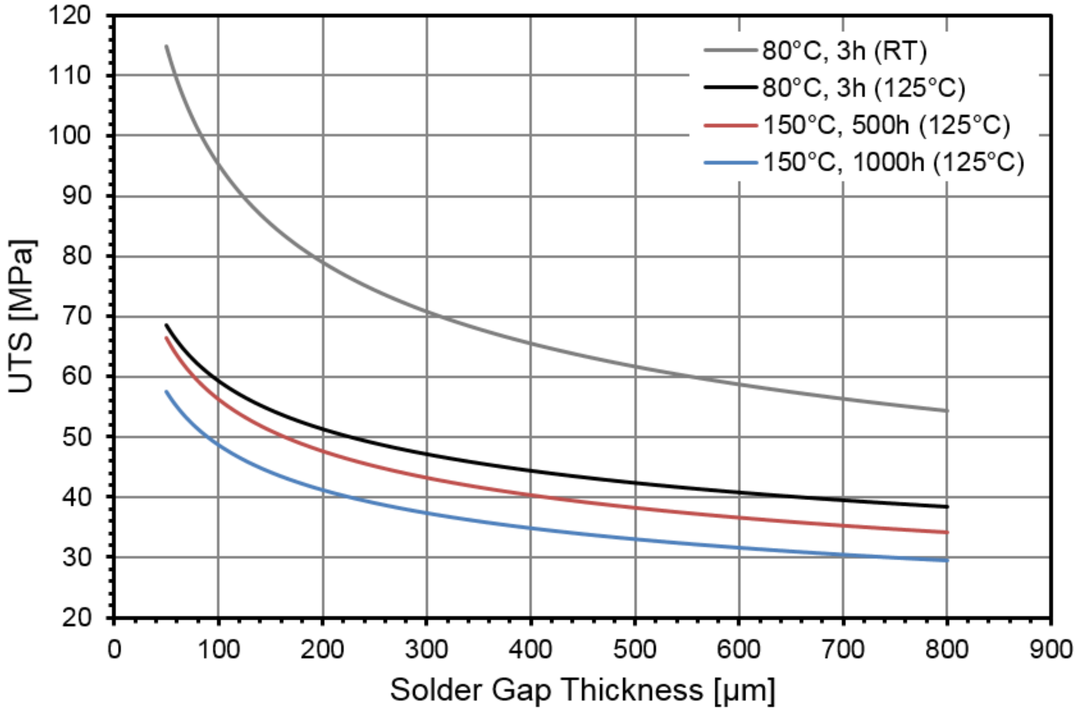

Figure 2.21. Dependency of tensile strength on solder gap thickness at 125°C for different isothermal aging times at 150°C.

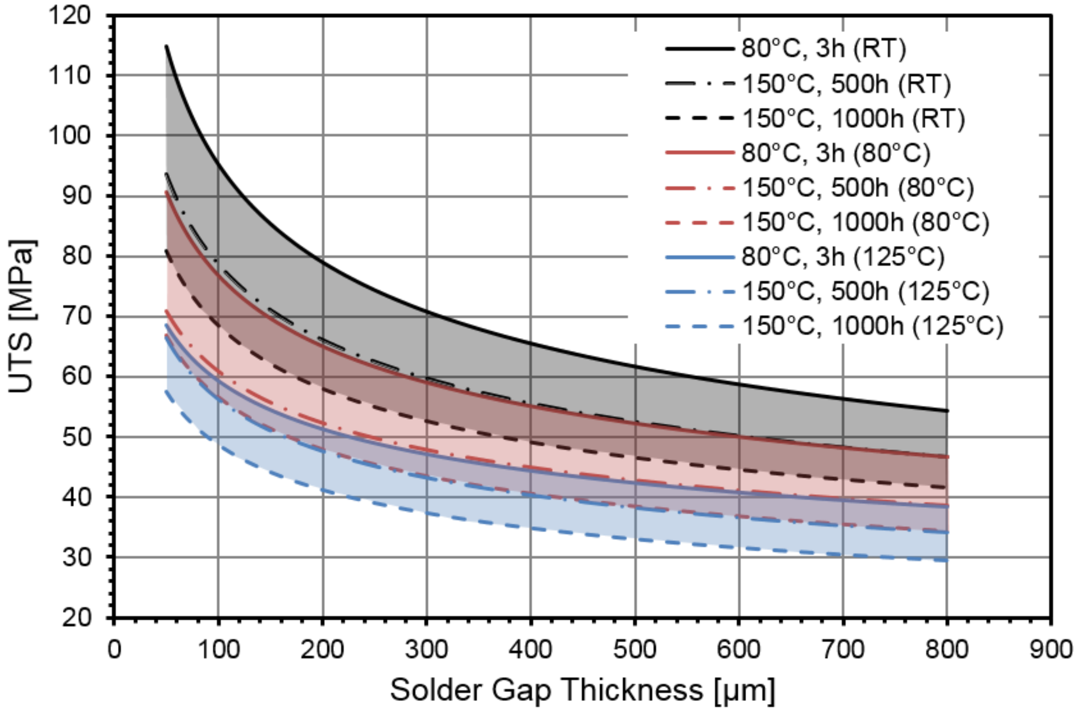

Figure 2.22. Effect of test temperature and the aging conditions on the UTS as a function of solder gap size.

2.5. Strain Distribution

2.5.1. Digital Image Correlation System - VIC 3D

The VIC-3D Micro™ system by Correlated Solutions was used to measure displacement and strain under high magnification. Digital image correlation (DIC) is an optical method for determining strain, displacement, and strain gradients for a sample undergoing deformation. The stereoscopic principle of the setup with two sensitive CCDs collects a series of photographs (speckle patterns) and imports them into the VIC-3D software. Objects contour, displacement and strain is measured contactless and full field with the VIC-3D system with an accuracy of 0.01 pixel for displacement and 0.01% for strain. The speckle patterns movement is measured by determining the first four components of the Lagrange finite strain tensor, in addition to providing a graphical representation of the strain concentration gradient at every point on the specimen surface. The Von Mises strain is used to evaluate the strain distribution on the solder gap surface by using the VIC-3D system. The Von Mises strain is a parameter to determine at which points strain is occurring in the x, y and z axis and will cause failure. The used setup for the tensile tests is shown in Figure 2.23.

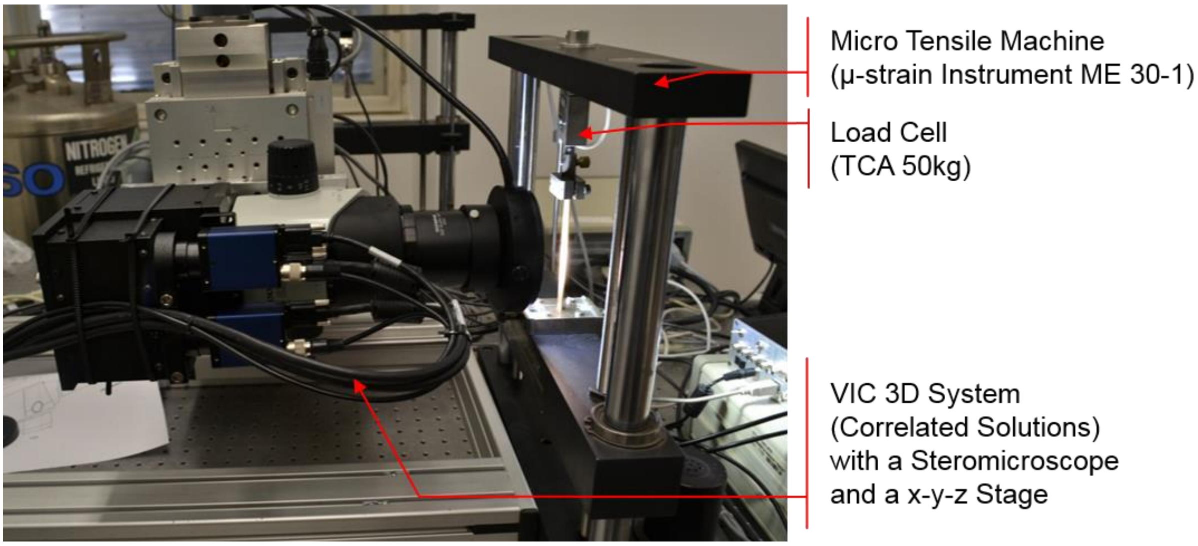

Figure 2.23. Schematical tensile setup including the VIC 3D system in combination with a stereomicroscope.

2.5.2. Strain Distribution in SnAgCu Solder Gaps

Experimental stress-strain curve for nonaged solder joints with gap sizes of 122 µm, 404 µm and 790 µm are presented in Figure 2.24. The strain values are shown up to the start of crack initiation. Especially the crack initiation and propagation influences the calculation of the strain, so that these values cannot be used due to the high inaccuracy of the strain value. The created speckle pattern is unusable in the region of the crack initiation and the image processing (DIC) leads to inaccuracy (high strain values).

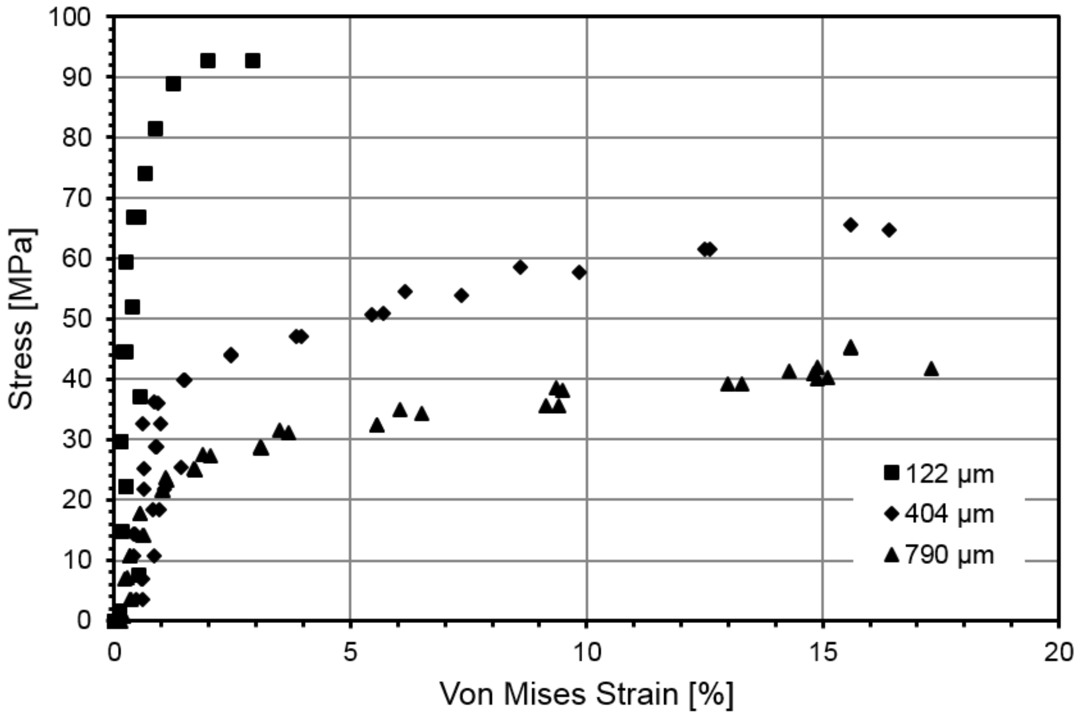

Figure 2.24.Stress-strain curves of Cu/Sn3.5Ag0.75Cu/Cu solder joints with various thicknesses measured with the VIC 3D system.

The results show an increase in tensile strength with decreasing gap size and higher strain level for thicker solder joints. The strain level until fracture was 2.9% for the 122 µm, 16.4% for the 404 µm and 17.3% for the 790 µm solder gap. The shown Von Mises strain in the plot (Figure 2.24) represents the maximum of the strain distribution over the solder gap surface. The relationship between the measured strain value and the solder joint thickness corresponds to the measurements done by the laser speckle system (Figure 2.12). However, the strain values measured by VIC-3D refer to the ductility of the solder joint and represent the true strain distribution of the joint under tensile deformation.

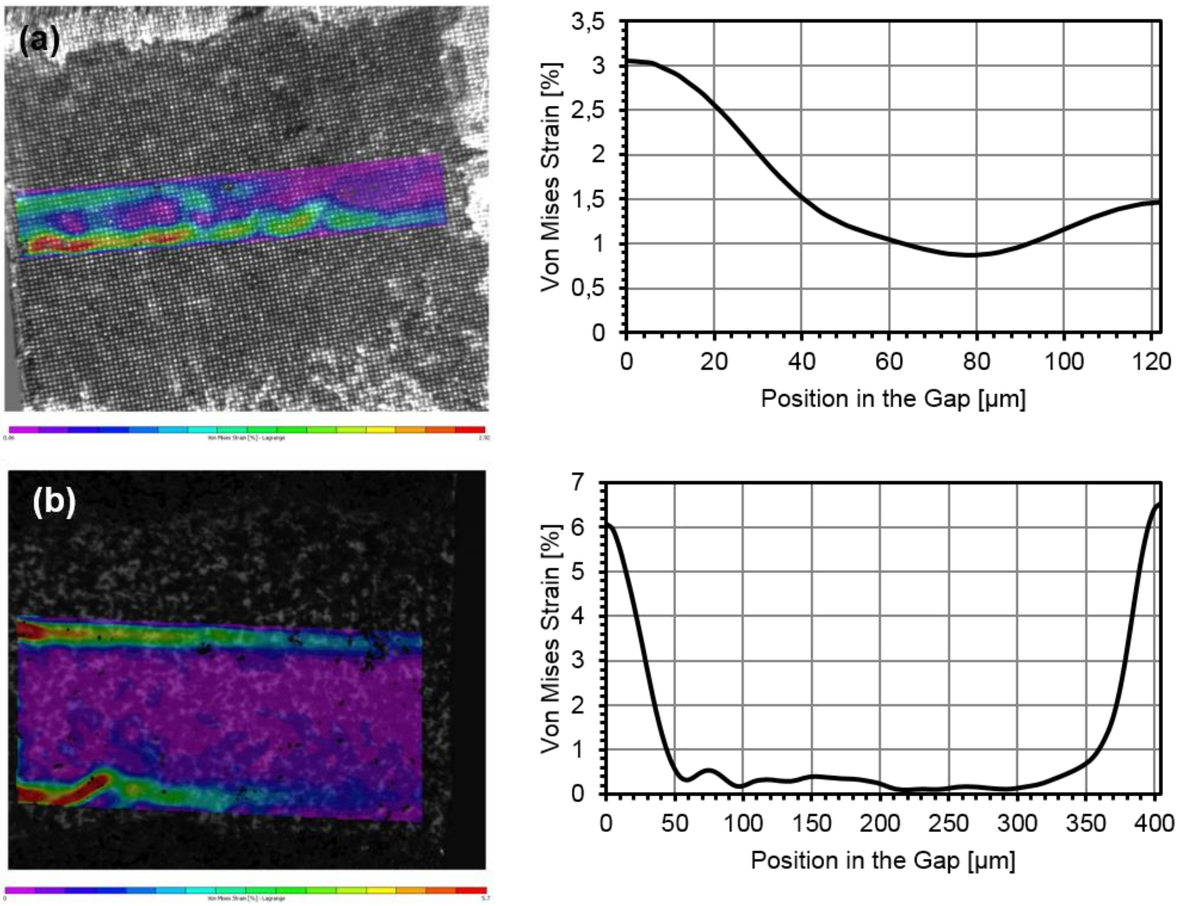

Figure 2.25. VIC-3D measurement of two solder gaps with the thickness (a) 122 µm and (b) 404 µm with corresponding Von Mises strain distribution across the solder joint at 92 MPa and 54 MPa before crack initiation.

The typical distribution of the strain for the two solder gaps is shown in Figure 2.25a,b. The location of strain concentration is close to the interface at both sides of the solder joints for all gap sizes. The strain decreases from the upper side of the gap (corresponding to the left side of the plot) to the midsection and increases again towards the lower side of the solder joint. The distribution is inhomogeneous across the solder joints, but the maximum of the strain distributions occurs always at or near the interface. The locations of the maximum strain correspond to initiation of cracks during the tensile deformation leading to near interface fracture as observed previously (Figure 2.14 & 2.18).

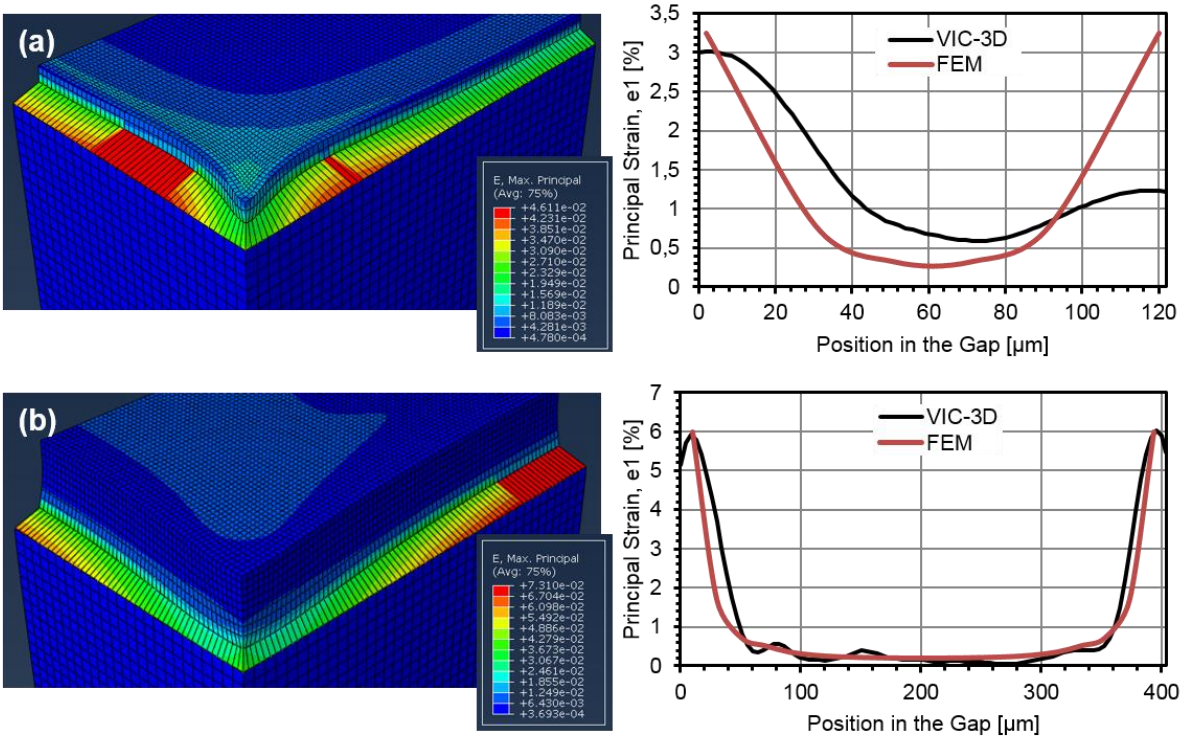

Figure 2.26. Comparison of measured and simulated strain distribution across the solder (a) 122 µm at 92 MPa, (b) 404 µm at 54 MPa and (c) 790 µm at 34 MPa before crack initiation with corresponding FEM model. [1]

With the obtained data on the strain distribution in solder gaps ≤ 800 µm, a constitutive model for finite element simulations can be created, as proposed by Khatibi et al for a SAC307 solder [36]. A pressure dependent fracture criterion was used, which corresponds with the U-shaped strain distribution across the thickness of the solder joints. As part of a COMET project, supported by the Material Center Leoben GmbH, M. Lederer used the referred constitutive model and created a Finite Element Model for the Sn3.5Ag0.75Cu alloy with a high correspondence of the U-shaped strain distribution. Figure 2.26 shows the distribution of the first principle strain *e1* across the solder joints as obtained by VIC 3D measurement and simulations with the associated FEM plots for each solder joint thickness. These plots represent the strain distribution at a load step of 92 MPa for 122 µm (a) and 54 MPa for 404 µm (b) solder gap thicknesses near the UTS of each sample before crack initiation. Since the strain distribution in the real solder joints is not always perfectly symmetrical (Figure 2.26a) deviations between the measured and calculated plots can be expected. In the present

[1] Project A.7-11 „Life time of functional multilayer ceramic systems“
Material Center Leoben GmbH, M. Lederer

experiments the best correlation between the simulated and measured values was obtained for the 404 µm solder joint in which the cracks were initiated almost simultaneously at both sides of the solder gap Figure 2.26.

Further three dimensional elasto-plastic simulations were performed by Lederer et al. [53] to characterize the strain singularity in the material transition between copper and solder. The mesh refinement was improved until the best possible agreement with the result of the VIC-3D measurements was achieved. In this work it is suggested to apply models based on SGT in order to avoid strain singularity at the surface of the material transitions at interface, which occur by the modeling of solder joints using classical continuum mechanics. A strain gradient theory is under development by Lederer for 3D FEM simulations to solve the singularity [53].

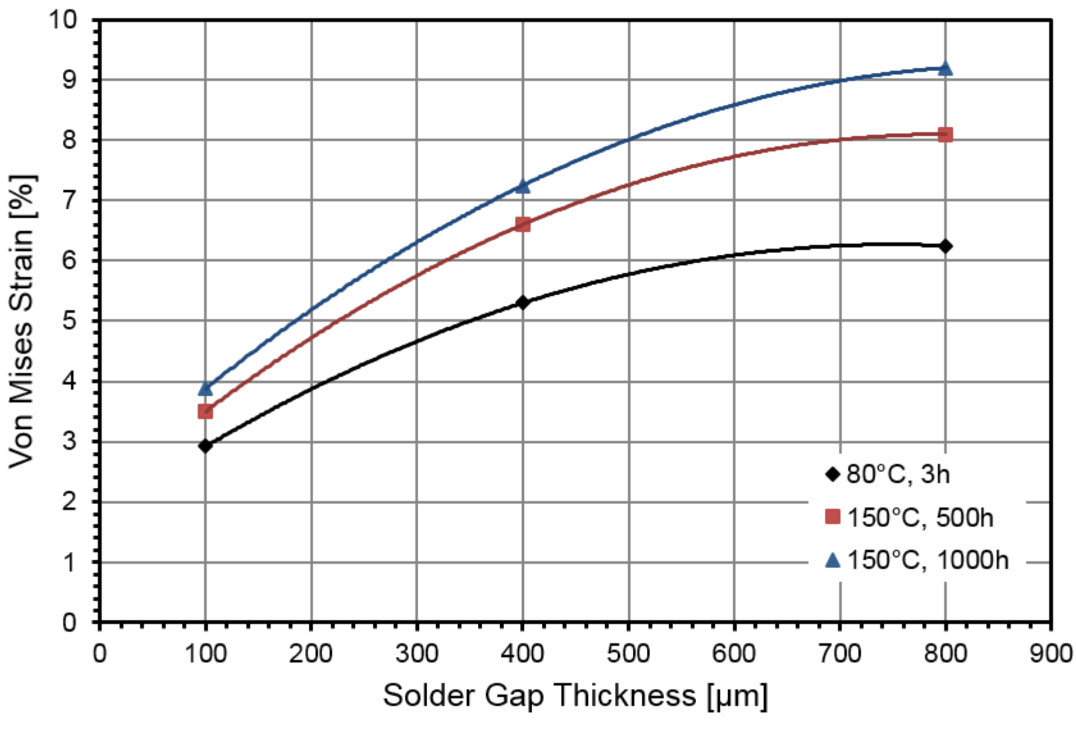

Figure 2.27. Dependencies of Von Mises strain on solder gap thickness of different aging conditions before crack initiation.

The same measurements were performed on heat treated samples (Figure 2.27). The Cu/Sn3.5Ag0.75Cu/Cu samples were aged at 150°C (500h and 1000h) resulting in an increase of the ductility of the solder body and a growth of the IMC volume proportion. The maximum value of Von Mises strain required for crack initiation for each exposure time and solder gap thickness is shown in Figure 2.27. These values correspond to the stress levels listed in Table 5. Long time thermal exposure resulted in an increase of the maximum strain at the interface, with a high decrease in thick solder gaps as expected. The maximal strain level increases from 2.9% up to 3.9% for a 100 µm thin solder gap and from 6.3% up to 9.2% for a 800 µm thick solder gap. The locations of the maximum strain at the interface correspond to the site of fracture initiation and propagation in the Cu_6Sn_5 IMC layer of aged solder joints.

Table 5. Stress level until crack initiation for different aging conditions.

	100 µm	400 µm	800 µm
80°C, 3h	88.1 MPa	71.0 MPa	46.8 MPa
150°C, 500h	77.3 MPa	63.5 MPa	41.7 MPa
150°C, 1000h	65.9 MPa	59.9 MPa	32.8 MPa

2.6. Summary

The influence of microstructure on mechanical properties of Cu/Sn3.5Ag0.75Cu/Cu solder joints with various gap sizes was studied. It was found that the stress-strain response of solder joints is not only related to the constraint effect but is also highly dependent on the microstructure and especially the IMC layer thickness of the joints. An increase in tensile strength and a decrease in fracture strain with decreasing gap size were observed with a stronger effect for thinner joints due to their finer initial microstructure and the higher proportional IMC/thickness ratio. Solder joints with gap sizes in the range of 50-1000 μm did not show a high strain rate dependency of their stress–strain response. Increasing the gap size for non-aged solder joints resulted in a transition from brittle to ductile fracture mode. In the case of very thin solder gaps (<100 μm) independent of the aging time and temperature the crack occurred always in the IMC layer. Aging at 150°C for a period of 500h up to 1000h resulted in a reduction of the stress and an increase of the elongation of the solder joints with stronger effect of the latter for thicker joints. Transformation of the scallop shaped morphology of the Cu_6Sn_5 phase to a planar type in solder joints with an intermediate thickness (>100 μm) resulted in a cracking and failure in the Cu_6Sn_5 layer independent of the thickness of the layer. In case of the presence of both IMC phases failure occurred only in the Cu_6Sn_5 phase, due to the higher fracture toughness of the Cu_3Sn phase. The principal failure in the IMC region was also detected by the VIC-3D system by studying the Von Mises strain distribution on the solder joint surface. Independent of the solder gap size, an increased strain level was observed at the interface, which matches with the resulting fracture behavior.

CHAPTER 3
Creep Behavior of SnAgCu Lead-Free Solder System

3.1. Introduction

The miniaturization of electronic devices is the developing trend in the industry. The trend is smaller device size and higher functionality. Lifetime estimation and fatigue life prediction models of microelectronics depend on the study of the complex thermo-mechanical properties of miniaturized lead-free solder joints. Therefore, the characterization of the mechanical and thermal behavior of solder joints is a key issue, in order to support the design development for different reliability considerations. Further interest is the fact to analyze and study existing solder joint designs under mechanical and thermal loads until fracture. Stress relaxation is an important behavior, which leads to a better understanding what happened in solder joints under thermal and mechanical loads.

The stress relaxation test is a time dependent deformation method to determine creep behavior at high homologous temperatures. However, it is known that solder joints in electronic applications must survive a combination of mechanical and thermal stress under service. It is necessary to understand how heat treatments of solder joints, which happened under thermal testing and result in a change of the microstructure, may influence the stress relaxation process. The SnAgCu alloy is one of the most important lead-free solder systems used in electronic packages. Therefore, Sn3.5Ag0.75Cu model samples are used to study the miniaturization effect and the potential effect of aging.

The present chapter includes investigation of the stress relaxation behavior of Cu/Sn3.5Ag0.75Cu/Cu model solder joints with different ratios of IMC to the gap size. The IMC growth is realized by heat treatments at 150°C up to 1000 hours. Stress relaxation test is a particularly simple and attractive way to study the influence of the constraint effect on the creep behavior of solder joints. The results show the influences of size, temperature and aging effect with a significant influence on the creep properties of SAC solder joints.

3.2. Creep Properties of Selected Lead-Free Solders

3.2.1. Measurement of Stress Relaxation

Relaxation tests were performed using the µ-strain tensile machine ME 30-1 with a crosshead stroke resolution of 0.04 µm shown in Figure 3.1. The force was measured with a TCA load cell of 500 N capacity with a minimum load resolution of 10 mN. A hot air furnace was designed to heat the specimens with an accuracy of ± 1°C. The strain was measured by a non-contacting laser speckle video extensometer with a gauge length of about 20 mm and a strain resolution of 10^{-5}. The principle of the video extensometer is based on the evaluation of speckle patterns that are reflected from the sample surface by coherent laser light (660 nm wavelength). The extensometer automatically detects the light-dark transitions on the sample surface and evaluates them by using a fast Fourier transform (FFT) correlation analysis [42]. In order to assess the relaxation behavior of the Cu/Sn3.5Ag0.75Cu/Cu joints with various gap thicknesses, the samples were loaded with a constant strain rate of 3.5×10^{-3} s^{-1} to 30% below the ultimate tensile strength (UTS) corresponding to 0.3% strain in the plastic range between yield strength and UTS and then the load drop was recorded as a function of time for at least 1 hour. The stress relaxation tests were performed at RT, 80°C and 125°C to obtain the creep parameters.

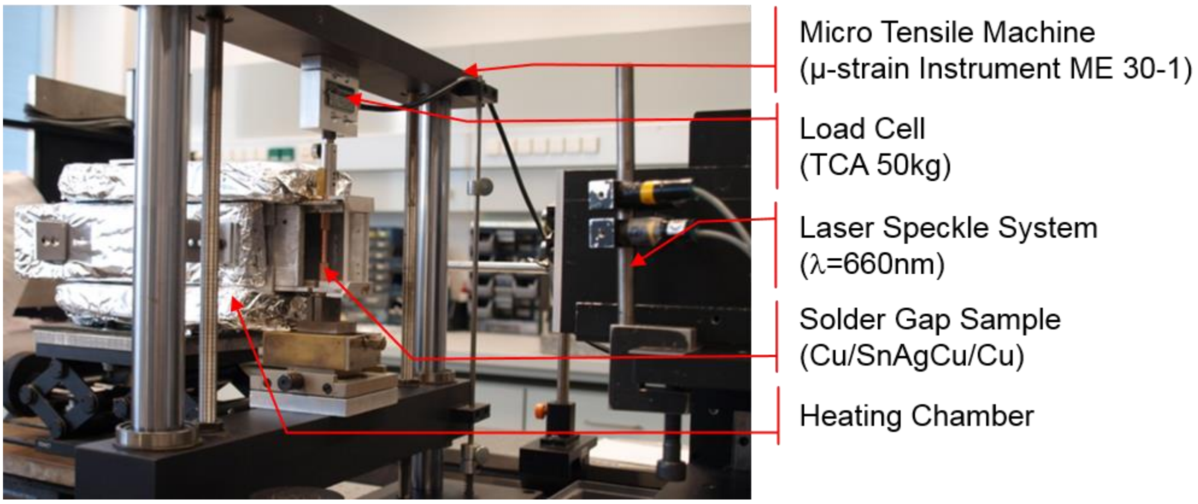

Figure 3.1. Tensile setup for the stress relaxation experiments with heating chamber

3.2.2. Creep Properties as Function of Solder Gap Thickness

The stress relaxation tests for Cu/Sn3.5Ag0.75Cu/Cu solder joints with gap thicknesses of 800 µm down to 100 µm were carried out in the plastic region between the yield strength and UTS. The testing point of 30% below the UTS is verified by tensile test at RT, 80°C and 125°C. The influence of temperature on the UTS is shown in Figure 2.19, with a 28% to 43% reduction of the UTS for thicker and thinner solder joints respectively. Figure 3.2 shows the normalized stress relaxation curves for various solder gap sizes at RT. After one hour, a stress drop of 15%, 7%, 5% and 3% are obtained for the solder gap thicknesses of 830µm, 450µm, 200µm and 130µm. Further it can be observed that the steady state (saturation) has not been reached during the testing time of one hour. The thicker SnAgCu joints show a large stress drop in comparison to the reduced stress drop observed for thinner solder gap, which is based on the size effect. Firstly the stress drop is dependent on the ductile solder volume, which supports the transition of the elastic strain into the plastic strain. Secondly thin solder joints have a decreased transition of the elastic strain into the plastic strain due to a higher proportion of high-strength but brittle IMC phases in the solder composite. VIC-3D measurements of tensile test (Chapter 2.5) confirm the strain concentrations located close to the brittle interface at both sides of the Sn3.5Ag0.75Cu solder gaps. Figure 3.3 and 3.4 show the normalized stress relaxation curves for various solder gap sizes at 80°C and 125°C. After one hour, a stress drop of 44%, 18%, 8% and 4% are obtained for thicker to thinner solder gaps at a testing temperature of 80°C. A further increase of the temperature to 125°C resulted in a stress drop of 60%, 22%, 16% and 7% for the solder gap thicknesses of 830µm, 430µm, 200µm and 130µm. A sum up of the stress drops depending on solder gap thickness and testing temperature is listed in Table 6.

Table 6. Stress drop after 1h for different solder gap thicknesses at RT, 80°C and 125°C.

	~130 µm	~200 µm	~450 µm	~800 µm
RT	3%	5%	7%	15%
80°C	4%	8%	18%	44%
125°C	7%	16%	22%	60%

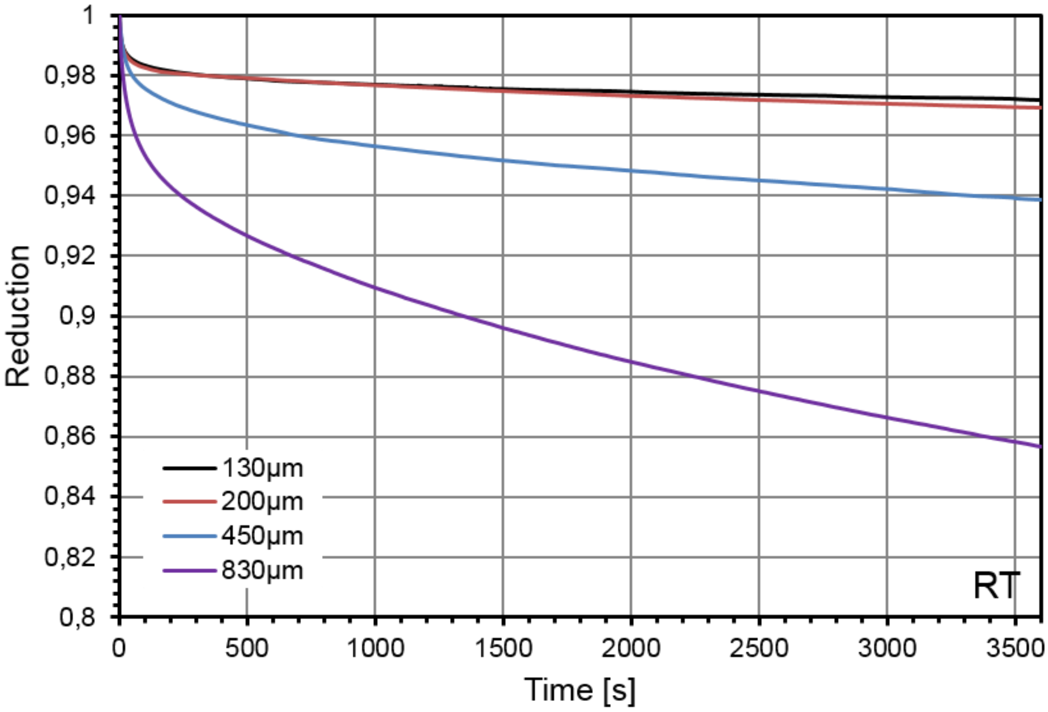

Figure 3.2. Stress relaxation over 1 hour for different solder gap thicknesses at RT.

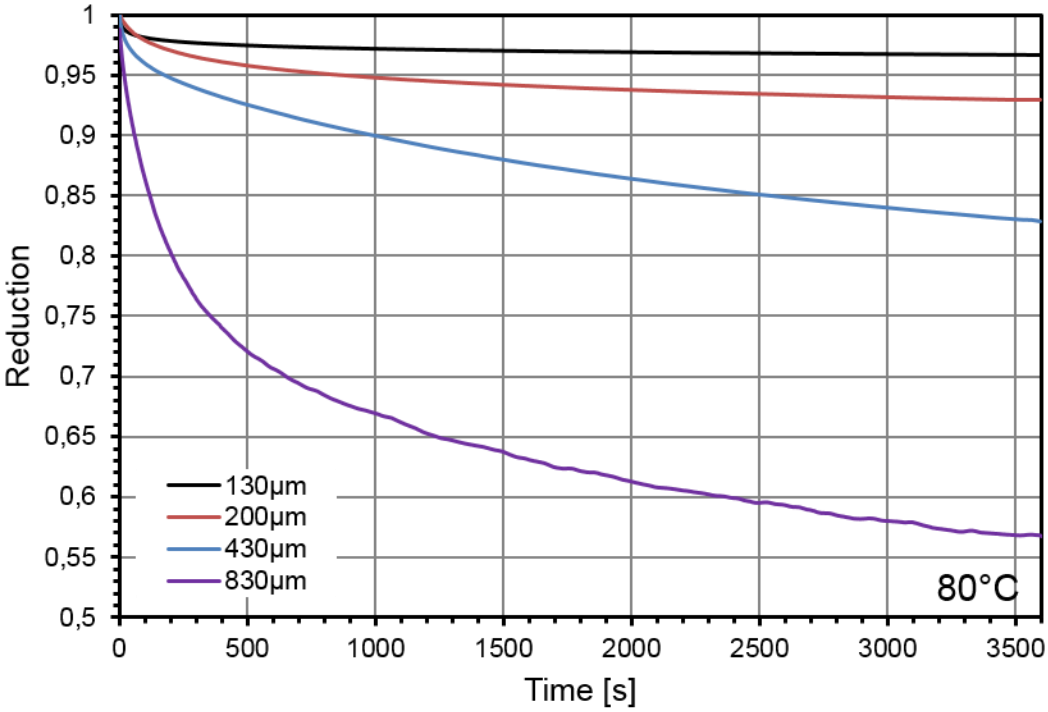

Figure 3.3. Stress relaxation over 1 hour for different solder gap thicknesses at 80°C.

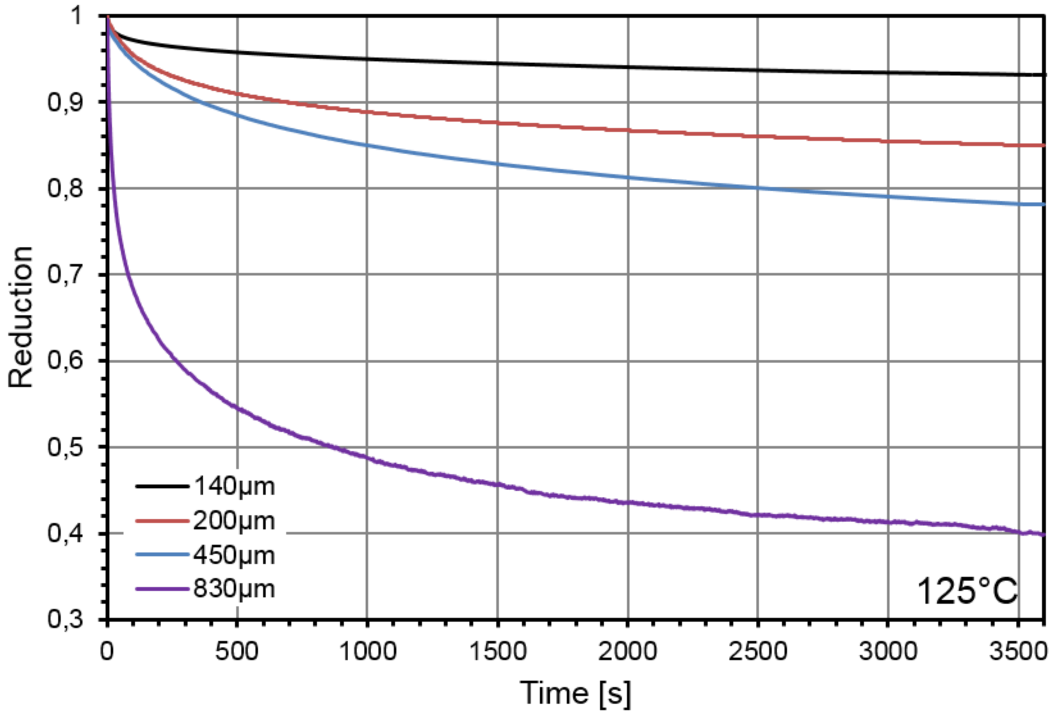

Figure 3.4. Stress relaxation over 1 hour for different solder gap thicknesses at 125°C.

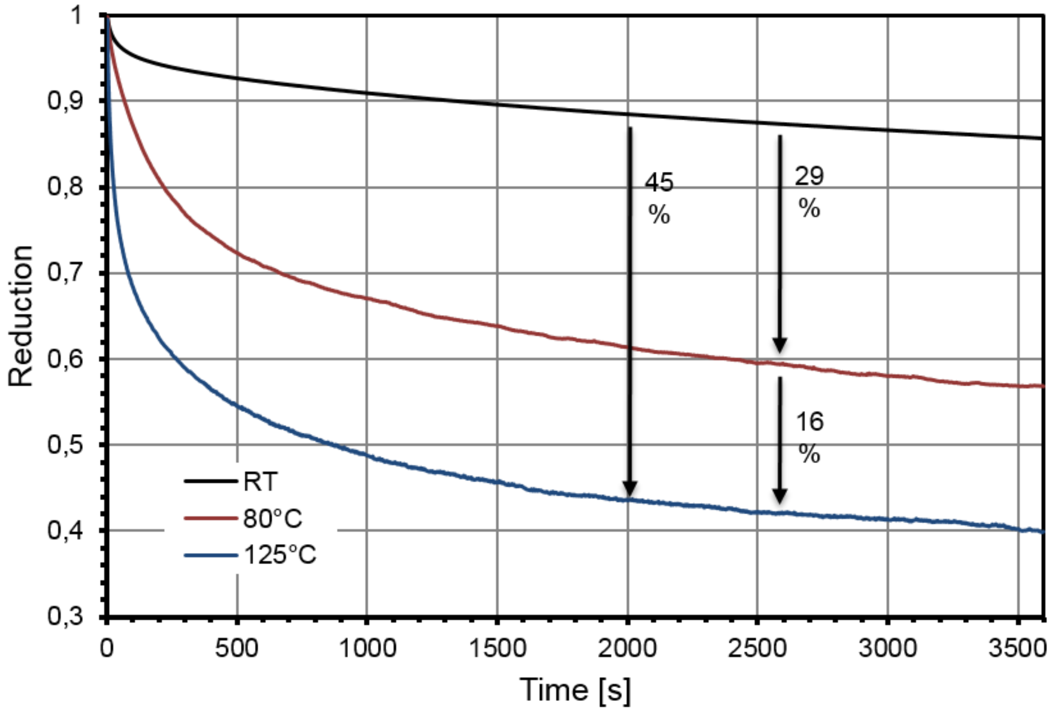

Figure 3.5. Stress reduction of a 830 µm thick solder gap at RT, 80°C and 125°C.

Figure 3.5 shows the normalized stress reduction plots for a 830 µm solder gap at RT, 80°C and 125°C. Testing at an increased constant temperature resulted in an increased reduction of stress over time due to the thermally activated plastic flow in the solder. The 830 µm solder gap has an increase of 45% of the stress reduction due to the influence of the testing temperature of 125°C. For solder materials, the mechanisms of stress relaxation or creep usually include bulk diffusion, dislocation climb/glide and grain boundary diffusion. The dominant deformation mechanism can be reflected by the values of the stress exponent n and the activation energy Q compared with values in the literature.

The typical creep behavior of Sn3.5Ag0.75Cu solder joints with a thickness of 830 µm and 130 µm at temperatures of RT, 80°C and 125°C are shown in Figure 3.6 and Figure 3.7. The stress exponent is determined by a simple power law (5), by plotting the creep rate against the stress in a double logarithm coordinate. Different stress exponents at different temperatures for various solder gap thicknesses are obtained. The stress exponents for a thick solder gap of 830 µm decreases from $n = 14$ down to $n = 5$ for a change of the test temperature from RT up to 125°C. The creep behavior found for thinner solder joints at RT, 80°C and 125°C have values of $n = 255$, $n = 170$ and $n = 78$ respectively. The absolute creep strength of thin gaps is higher than that of thicker gaps. This was expected since thin solder model gaps are showing almost no stress relaxation, which comes from the constraint effect in combination with the high occurrence of brittle IMC phase on the interface and in the solder volume, which does not allow plastic deformation. The temperature and the size effect on the stress exponent values of Sn3.5Ag0.75Cu solder joints with decreasing gap thickness are shown in Figure 3.8. The strong effect of the solder gap size on the stress exponent (creep properties) which was found in this study, has scarcely been reported by other investigators [9][10]. For example Sn3.5Ag solder joints show only a constraint effect resulting in a low increase of the exponent from $n = 5.8$ for 750 µm gap thickness up to $n = 10.5$ for 150 µm gap thickness [49]. The creep behavior is strongly dependent on the solder alloy with corresponding microstructure due to the sample production.

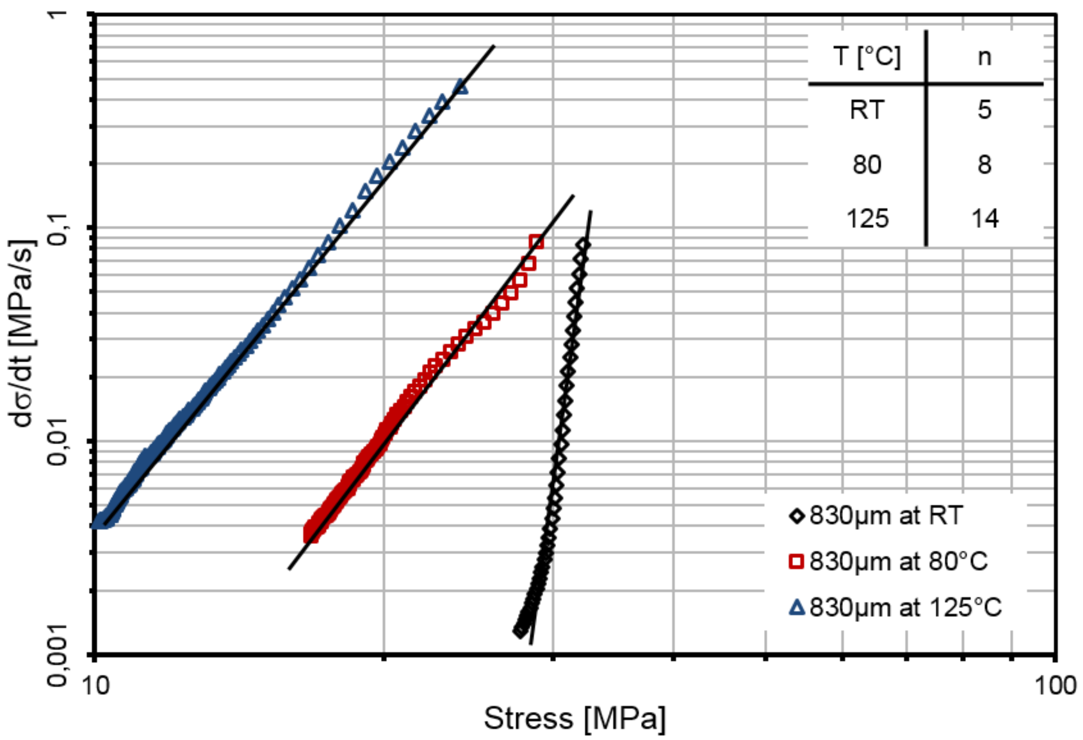

Figure 3.6. Stress relaxation data for Sn3.5Ag0.75Cu solder gap thickness of 830 µm at test temperatures of RT, 80°C and 125°C.

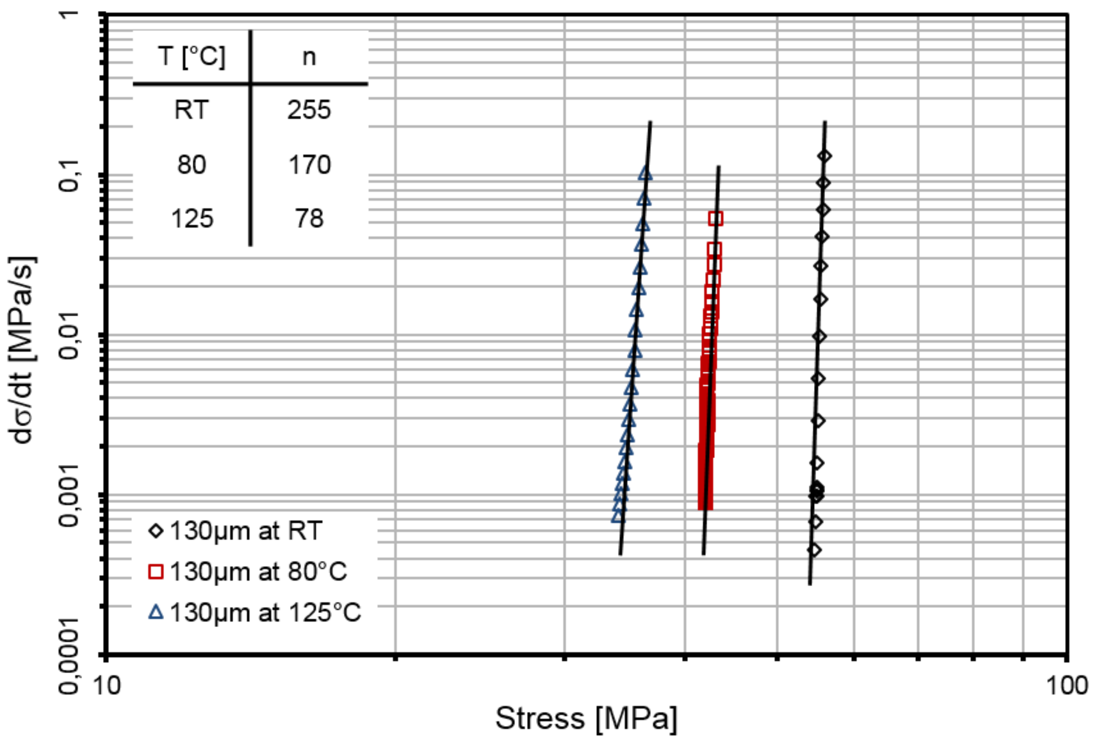

Figure 3.7. Stress relaxation data for Sn3.5Ag0.75Cu solder gap thickness of 130 µm at test temperatures of RT, 80°C and 125°C.

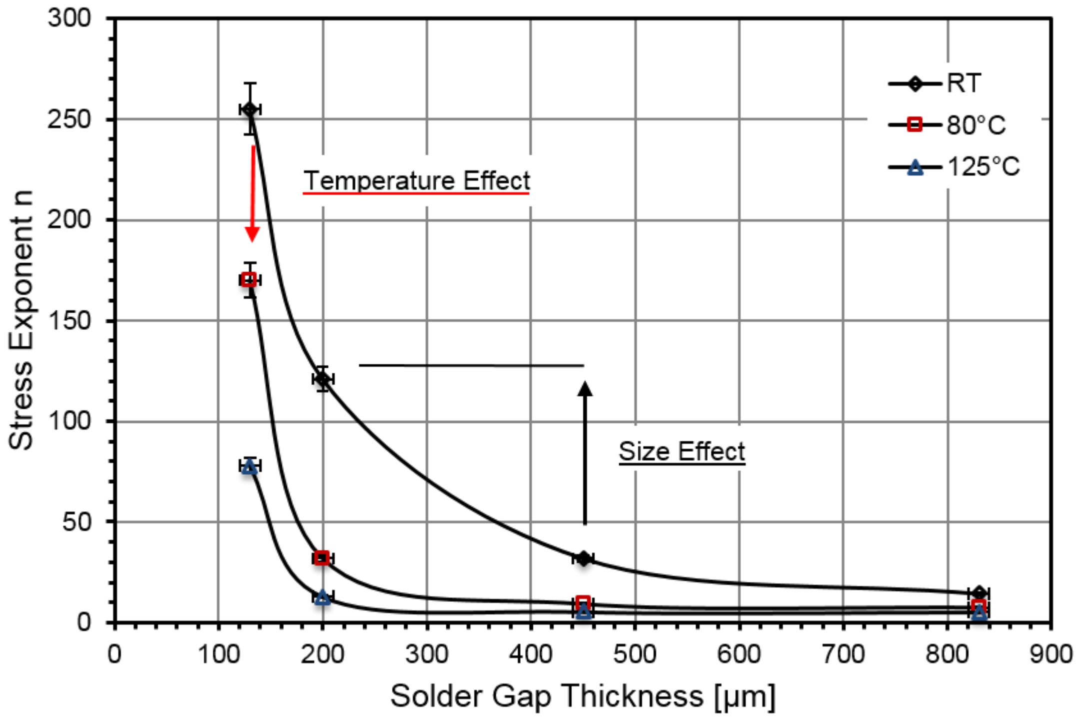

Figure 3.8. Dependency of the stress exponent n_2 on solder gap thickness of different isothermal boundary conditions RT, 80°C and 125°C.

The activation energy as determined by the slope of the plot $\ln(\dot{\sigma})$ versus the reciprocal temperature is about 55.4 kJ/mol and 72.9 kJ/mol for the solder gap thicknesses 830 µm and 130 µm. A summary of stress relaxation data for Cu/Sn3.5Ag0.75Cu/Cu joints with various gap thicknesses is listed in Table 7. The values for the activation energy of Sn3.5Ag0.75Cu solder joints are close to other creep investigations found in the literature. Shohji et al. [54] has achieved an activation energy of 47.3 kJ/mol (Sn3.5Ag0.75Cu) and Lang et a.l [55] an activation energy of 78.0 kJ/mol (Sn3.5Ag). The values for the activation energy investigated in this study are very close to that for the creep of tin controlled by pipe diffusion (70 kJ/mol) [56]. Thus, the creep behavior can be related to a slip creep mechanism controlled by pipe diffusion.

Table 7. Stress exponent n and activation energy Q for different Sn3.5Ag0.75Cu solder gap thicknesses.

n	*RT*	*80°C*	*125°C*	*Q [kJ/mol]*
830 µm	14.4	7.6	5.3	55.4
450 µm	31.9	9.4	5.5	61.9
200 µm	121.0	32.0	13.0	69.6
130 µm	255.0	170.0	78.0	72.9

A comparison with activation energies of Sn3.5Ag investigation of Zimprich et al. [49] is shown in Figure 3.9. For thinner solder gaps both alloys show similar values of *Q*. However while a steady decrease in the activation energy of Sn3.5Ag0.75Cu solder joints is observed, this value decreases only for thick solder joints of the Sn3.5Ag alloy. SnAgCu has a higher IMC proportion in the solder volume than SnAg, due to the addition of copper in the alloy. This leads to a change in the stress relaxation behavior for thicker joints.

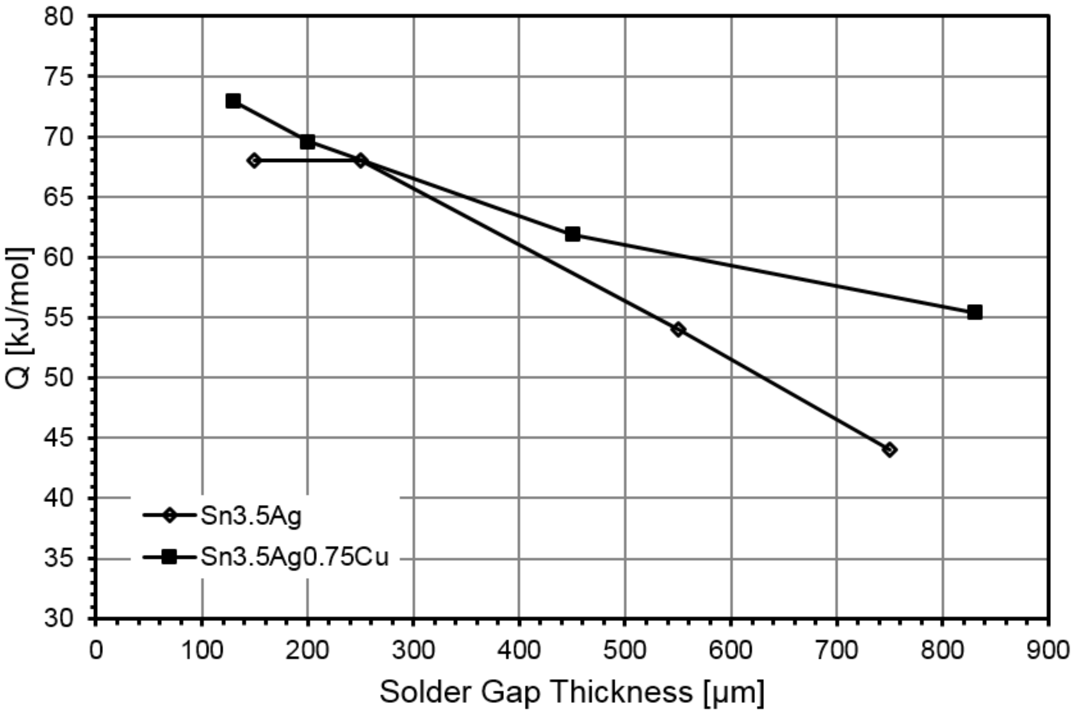

Figure 3.9. Activation energy versus solder gap thickness of the solder alloys Sn3.5Ag0.75Cu and Sn3.5Ag [49]**.**

3.2.3. Creep Properties as Function of Microstructure

Thermal aging results in the softening of the solder material due to the microstructural changes from finer to coarser IMCs and grain growth. The Cu_3Sn interfacial phase is formed and an increase of the total thickness of IMC layer is observed. The growth of IMCs contributes to a higher proportion of high-strength but brittle phases in the solder composite. Long time thermal exposure at 150°C (500h and 1000h) results in a reduction of ultimate tensile strength and a further decrease in the tensile strength is obtained by testing at temperatures of 80°C and 125°C. Figure 2.22 shows the aging effect on the UTS for each test temperature, which is necessary to determine the testing point 30% below the UTS for the stress relaxation.

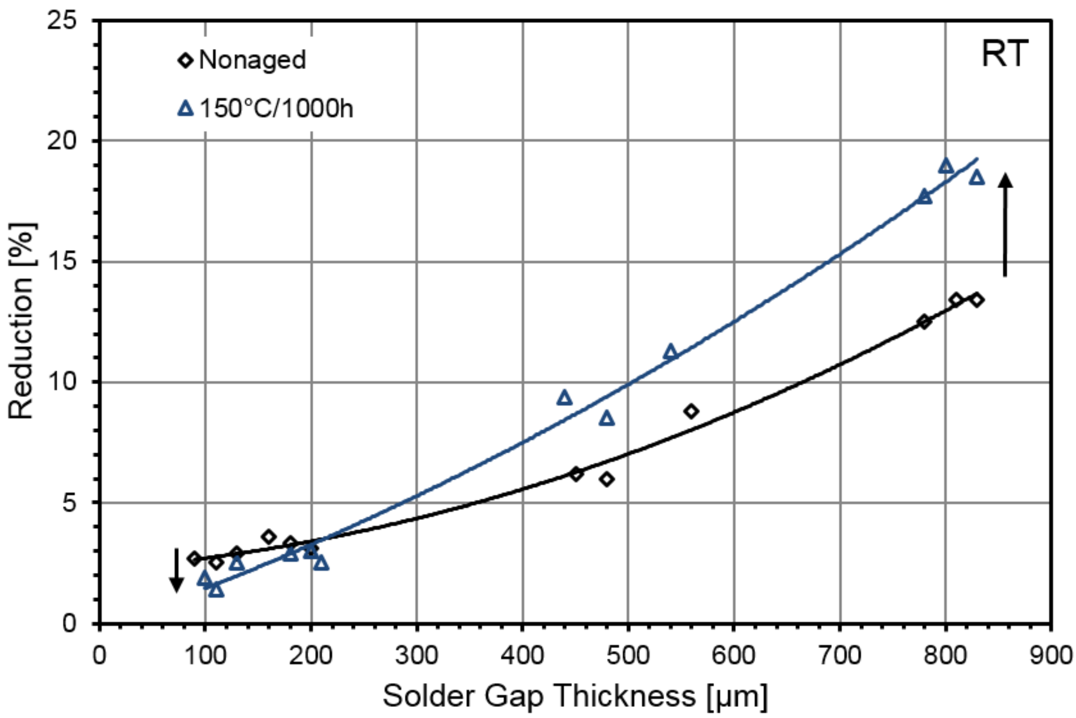

Figure 3.10. Dependencies of stress reduction on solder gap thickness of different aging conditions at RT.

Figure 3.10 shows the stress reduction in % depending on the solder gap thickness for nonaged and aged (150°C for 1000h) samples at RT. As expected, an increase of the stress relaxation for thick solder joints is obtained due to the softening effect by aging. Thin Sn3.5Ag0.75Cu solder gaps < 200 mm show an opposite effect. A decrease of the stress relaxation is obtained due to higher proportion of high-strength but brittle

IMC phases in aged thin solder gaps. Through this size behavior on stress relaxation an intersection point occurs where the aging effect has no influence on the relaxation. The softening effect and the brittle phase growth neutralize each other and no effect is achieved. Figure 3.11 and 3.12 show the dependency of the heat treatments of 150°C for 500h and 1000h for test temperatures of 80°C and 125°C. The aging effect results in an increase of the stress reduction together with the temperature effect and results in a higher transition of the elastic strain into the plastic strain in the solder gap. However, the effect of aging is minimized with increasing the temperature due to the dominant plastic flow. Especially thin solder gaps are dominated by the temperature controlled stress reduction. The temperature of 125°C is high relative to the melting point (T_h = 0.8) which results in a significant creep behavior under stress. This means that with increasing test temperature, the stress relaxation cannot be influenced further more by the aging effect.

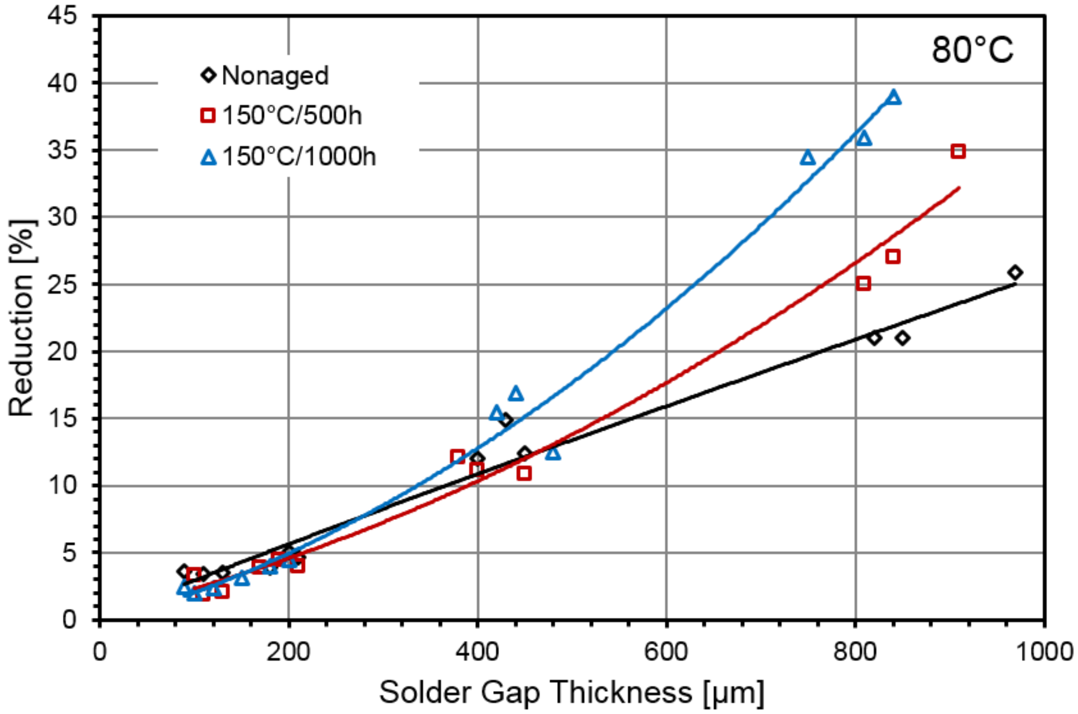

Figure 3.11. Dependencies of stress reduction on solder gap thickness of different aging conditions at 80°C.

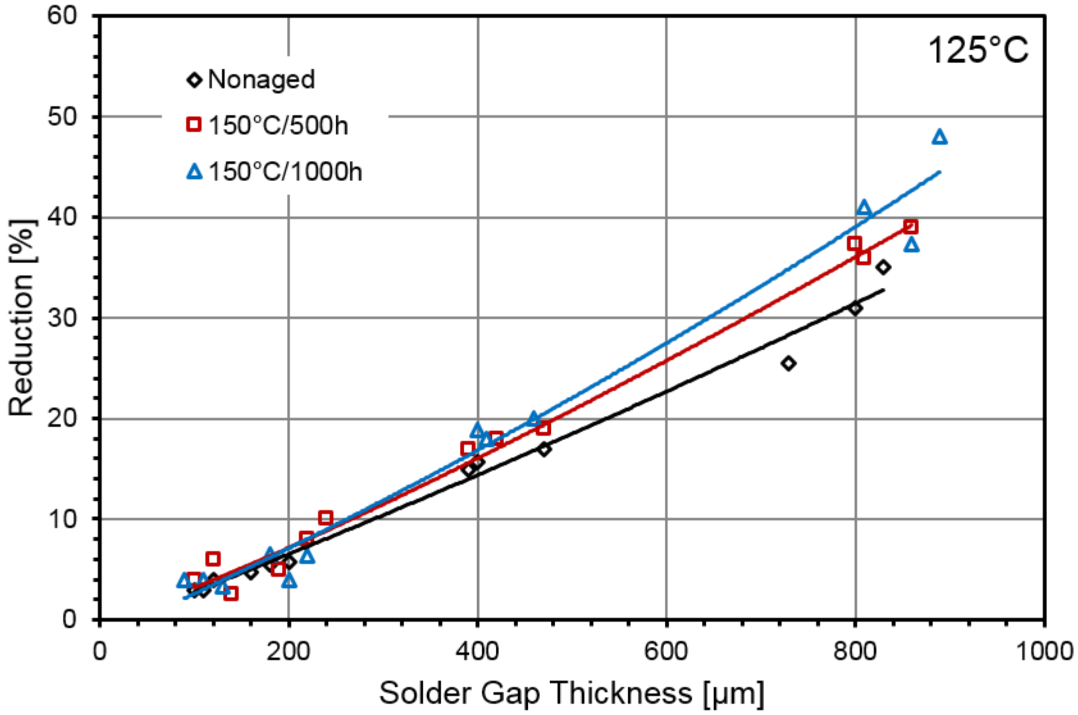

Figure 3.12. Dependencies of stress reduction on solder gap thickness of different aging conditions at 125°C.

3.4. Summary

Stress relaxation tests were performed for 830, 450, 200 and 130 µm eutectic Cu/Sn3.5Ag0.75Cu/Cu solder joints. A higher stress drop for thick solder gaps in comparison to thin gaps is obtained due to the constraint effect and the higher proportion of high-strength but brittle IMC phases in thin solder joints. The stress exponents and activation energies are determined by employing a simple creep power law equation. The stress exponent is temperature dependent and decreases with the increase of temperature for thick solder (830 µm) from $n = 14.4$ at RT down to $n = 5.3$ at 125°C. On thin solder gaps <200 µm, very high stress exponents are detected which depends on the amount of brittle IMC resulting in highly reduced stress relaxation. This context is also demonstrated by the growth of the IMC phase due to aging resulting in a further reduction of the relaxation. For a homologous temperature $T_h = 0.8$, heat treatments at 150°C up to 1000h show no significant relaxation increase for thick joints and decrease for thin joints due to the temperature resulting in dominant plastic flow. The activation energy is dependent on the solder gap thickness and is 55.4 kJ/mol for a gap thickness of 830 µm and 72.9 kJ/mol for a 130 µm thin solder joint. The value for the activation energy of the thick and thin SnAgCu solder joints can be related to a slip creep mechanism controlled by pipe diffusion and is consistent with results from the literature [11][54][55]. Aging at 150°C for a period of 500h up to 1000h together with the temperature effect resulted in a higher transition of the elastic strain into the plastic strain in the solder gap. But the aging effect is minimized with increasing the temperature due to the dominant plastic flow ($T_h = 0.8$), especially for thinner solder gaps there is no significant difference between aged and nonaged. The stress relaxation cannot be influenced further more by the aging effect at homologous temperatures ≥ 0.7 for Sn3.5Ag0.75Cu solder joints < 400 µm and > 0.8 for solder gaps > 400 µm. Therefore the size effect on creep behavior as well as the dependence on the content of brittle IMC phase is significant for miniaturized solder joints.

CHAPTER 4
Coefficient of Thermal Expansion of Miniaturized SnAgCu Solder Joints

4.1. Introduction

Thermal expansion coefficient is a characteristic material property, is partly responsible for the functionality and the durability of the system components. There are comprehensive sets of rules and recommendations for the determination of thermal expansion with a variety of methods by ASTM international, but the resulting determination of the coefficient of thermal expansion is not yet standardized.

Microelectronic devices are composed of a variety of materials with different physical and mechanical properties. Mismatch between the coefficients of thermal expansion of the constituent materials is the primary source of stress or strain in these complex structures. Furthermore thermal exposure during the operational life results in formation and growth of brittle intermetallic compounds in the interface between the solder and the substrate. Solder joint failure due to thermal mismatch has been reported to be one of the main reliability issues in microelectronic devices. The interest in recording the deformation characteristics of miniaturized interconnects has continuously grown during the last decade. This rapid growth has pushed the development of new technologies, and also the adaptation of existing techniques to meet the new measurement requirements. The determination of local strain in miniaturized interconnects with high accuracy and resolution in a non-contacting way often represents a challenge for modern material science methods. Promising results have been obtained by using optical methods to measure local thermal and mechanical strains at high temperatures [57][58].

In the present chapter the influence of microstructure on thermal response of miniaturized lead-free solder joints was investigated. The focus of the study was the change of the overall coefficient of thermal expansion of Cu/Sn3.5Ag0.75Cu/Cu solders joints with different ratios of IMC. A laser interferometric sensor (LIS) was used to measure the coefficient of thermal expansion of the solder joints.

4.2. Thermal Properties of Selected Lead-Free Solder System

4.2.1. Measurement of Thermal Expansion

In this investigation a laser interferometric system (LIS) was used to determine the deformation behavior of miniaturized solder interconnects subjected to thermal loading. The LIS is an optical system for measuring the displacement between two Vickers indentations marks with a maximum distance of 200 µm. The basic optical principle of the non-contacting strain sensor is the modified Young's double slit phenomenon, which was first used by Sharpe [59]. The diffraction patterns which are formed by the reflected laser beams from the two indentations overlap and form interference fringes at an angle of approximately 42°. The indents size and distance on the specimen surface must be small enough to create sufficient diffractions and interference from the incident coherent monochromatic light. Application of thermal or mechanical stress to the sample results in change of the distance between the markers and movement of the fringes. The resulting change between the two indentations is measured interferometrically by changes of the interference patterns. In all loaded systems rigid body motion and out-of-plane movements of the specimen surface occurs. To minimize the effect of the out-of-plane and to average the effect of the in-plane movements, two shutters direct two laser beams under equal angle of 42° into the indentations. The produced interference fringes, which are reflected plane parallel to the specimen surface, are recorded by a CCD camera and are analyzed in a signal processing unit (Figure 4.1). A detailed description of this system is given in [60]. Finally the relative displacement is calculated by the following equation,

$$ds = \frac{\lambda}{2 \sin \phi} (\Delta m_{upper} - \Delta m_{lower}) \qquad (14)$$

where *ds* is the change between the Vickers indentations, *Δm* is the relative fringe motion, λ is the wavelength of the laser light (He-Ne laser with λ=632 nm) and ϕ the angle between direction of illumination and of observation being 42°. The laser interferometer allowed, in the current state of development, measurements of local changes in length of a sample, under both mechanical and thermal stress of less than 200 µm. The interpolation between adjacent fringes provides the LIS a displacement resolution of about 2 nm. This value is smaller than 1/100 of the used wavelength λ=632 nm. [61][62]

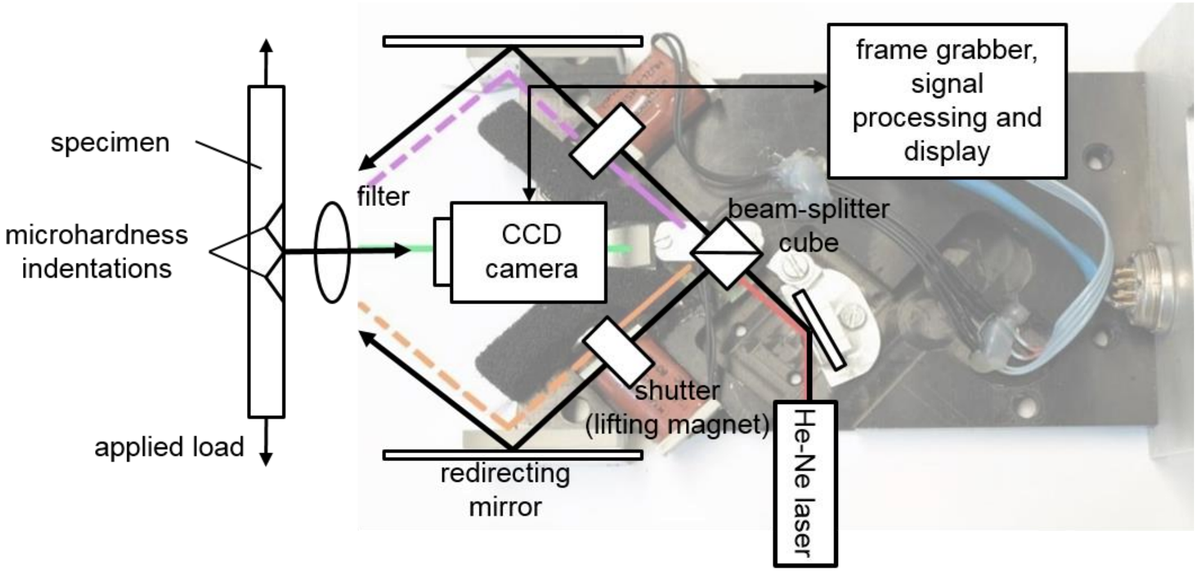

Figure 4.1.Schematic illustration of the laser interferometric measurement system.

Figure 4.2.Kammrath& Weiss heating unit with a PID controller.

Figure 4.2 shows the used heating chamber from Kammrath & Weiss. The heating unit uses a PID control in the temperature range between room temperature (RT) and 300°C. The maximum heating voltage of the module is specified with 0-30 V and a temperature resolution of 0.1°C. To ensure thermal contact between heating unit and measured sample, a thermal paste was used.

The calibration of the strain sensor was performed using an aluminum bulk sample. The calculated CTE of 24.4 ppm/°C in comparison to 23.6 ppm/°C, measured by the National Institution of Standards and Technology (NIST) [63], gives a measurement difference of 3% for the thermal expansion. A linear fit was used to determine the thermal strain data resulting in a linear course of the thermal expansion coefficient for aluminum in the measured range (Figure 4.3).

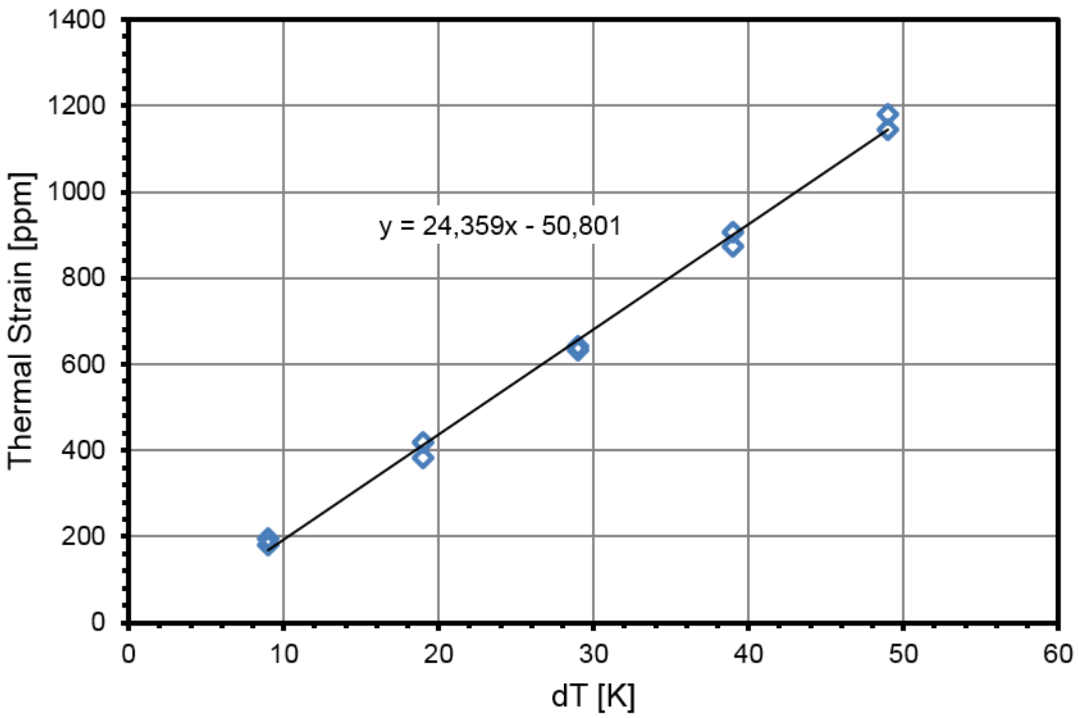

Figure 4.3. Thermal strain measurements using an Aluminum NIST sample for calibration of the LIS.

4.2.2. Thermal Expansion of Miniaturized Solder Gap

In this study the influence of the IMC layer thickness on local thermal expansion of miniaturized lead-free solder joints with a gap size of about 80 µm and 120 µm is investigated. Figure 4.4 shows a picture of two pyramidal-shaped indentations introduced into the copper substrate of the Cu/solder/Cu solder joint, which are necessary to measure with the LIS. The width of the indentations is about 20 µm and the distance is in the order of 100 µm to 175 µm. The measurable solder gap sizes are limited to the LIS measuring range of 200 µm. For this reason, a thinner solder joint was chosen to study the size effect. To increase the reflectivity of the surface, the specimens were mechanically polished. The sample was heated by a PID controlled heating unit to three different temperatures with a stabilization phase of 3 min up to 124°C as shown in Figure 4.5. Starting from RT and with a total temperature difference (*ΔT)* of 102°C, thermal strain was measured at 40, 84 and 124°C. The change of distance between the two indentations was measured by using the LIS.

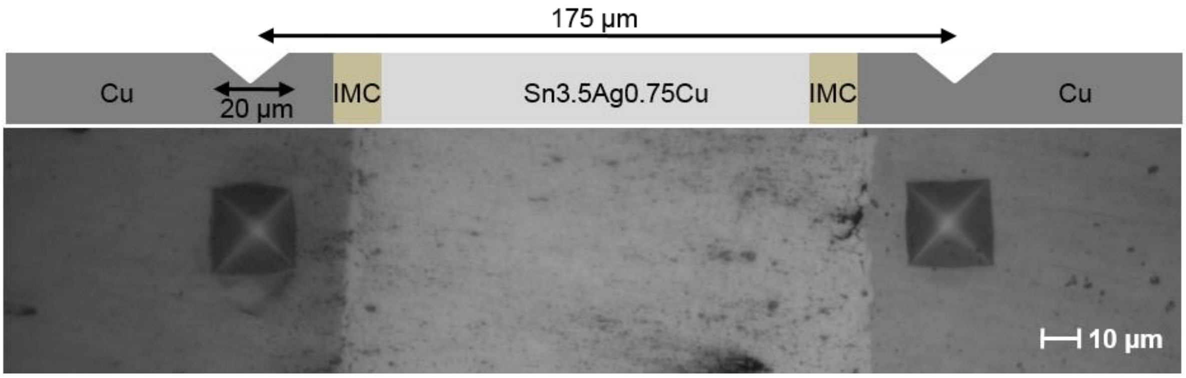

Figure 4.4. Illustration of two Vickers indentations pressed into the copper boundary of the SnAgCu gap.

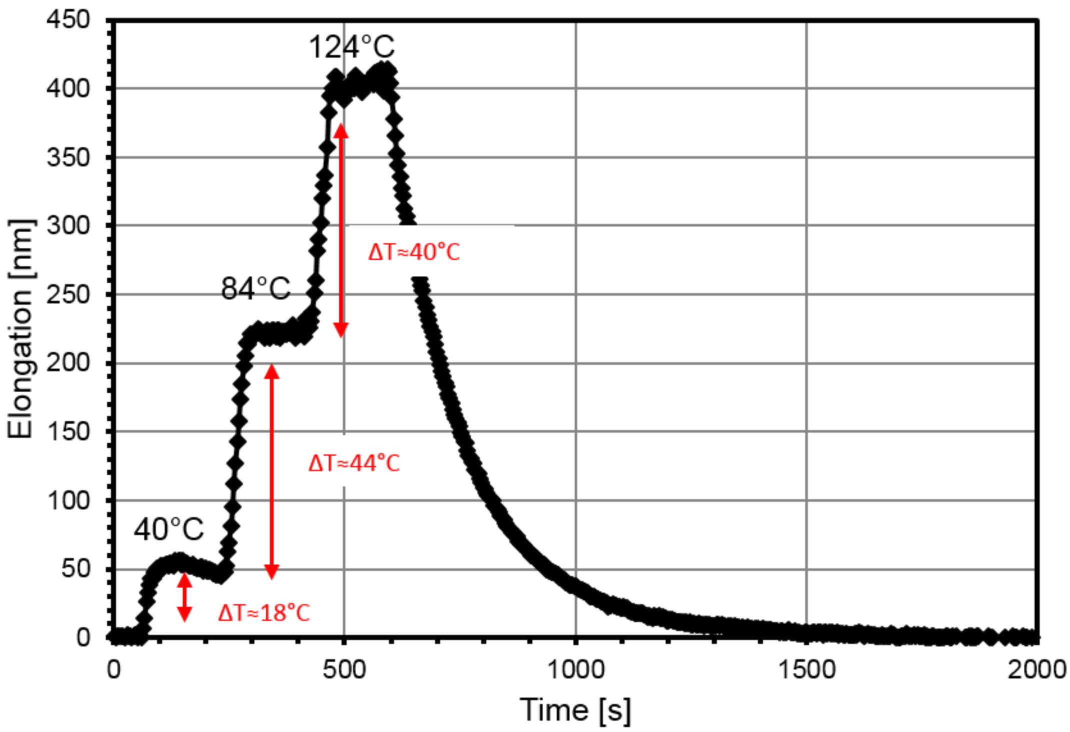

Figure 4.5.Change of distance dL at three temperatures and cooling phase for a solder gap of 120 µm with an indentation distance of 175 µm

Figure 4.6 shows the calculated thermal strain of two solder gap sizes from room temperature up to 124°C. The 2nd degree polynomial fit results in a CTE value 26.2 ppm/°C for the 80 µm and 25.9 ppm/°C for the 120 µm solder joints. The reported CTE values for Sn are in the range of 15 ppm/°C to 30 ppm/°C, depending on the microstructure and in particular the grain orientation of the solder [64]. The CTE value of the Cu_6Sn_5 layer is reported to be 19.0 ppm/°C [65]. The calculated average value of 26.1 ± 0.2 ppm/°C is plausible and can be assumed for small Sn3.5Ag0.75Cu gaps. The existing IMC phase Cu_6Sn_5 has probably no influence on the thermal expansion for gap thicknesses down to 80 µm. In non-aged samples the volume ratio of the IMC in the joint is still too small to affect the thermal expansion.

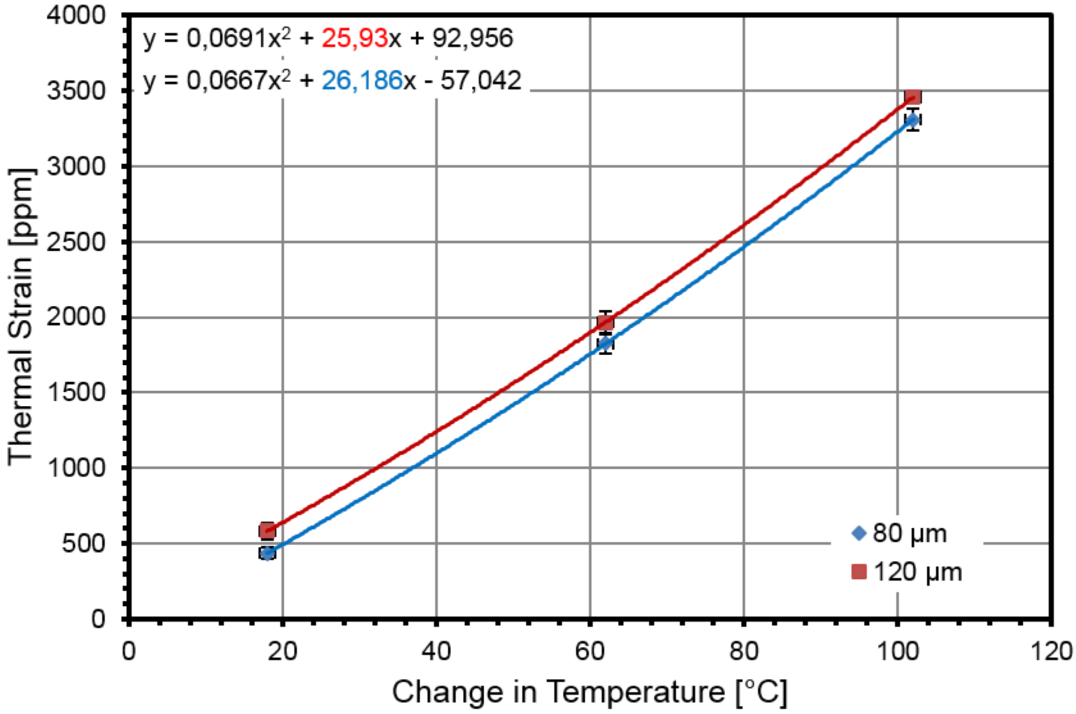

Figure 4.6. Thermal strain versus temperature change of 80 µm and 120 µm solder gap starting from room temperature up to a temperature difference of 102°C.

4.2.3. Thermal Expansion as Function of Microstructure

In order to investigate the relationship between the IMC growth and the global thermal expansion of the joints, CTE measurements were conducted on 120 µm and 80 µm Cu/Sn3.5Ag0.75Cu/Cu solder gap sizes after thermal aging at 150°C/500h and 150°C/1000h. Figure 4.7 and Figure 4.8 show the change in the thermal strain depending on the heat treatment conditions for the two solder gaps. For example, the total thermal expansion of a 120 µm solder gap was reduced from 25.9 ppm/°C to 21.2 ppm/°C and finally to 15.8 ppm/°C for samples subjected to heat treatments, respectively. The same reduction of the CTE over the aging time was observed for the 80 µm solder gap with a CTE reduction down to 18.6 ppm/°C.

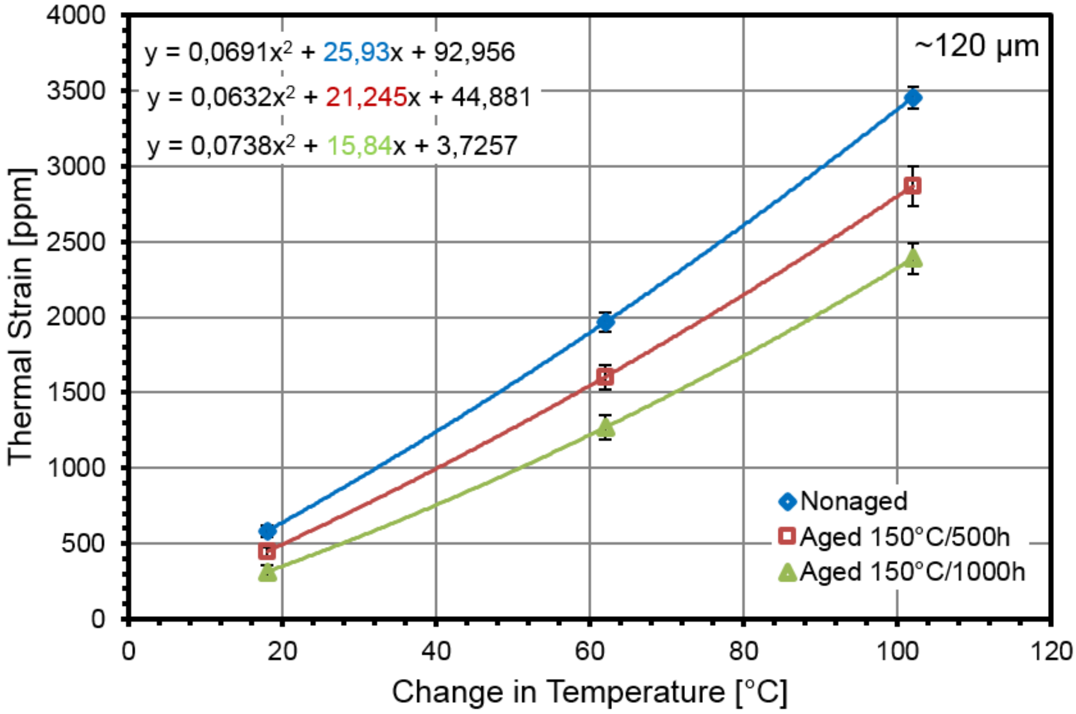

Figure 4.7. Thermal strain versus temperature change of a 120 µm solder gap starting from room temperature subjected to 80°C/3h, 150°C/500h and 150°C/1000h heat treatments.

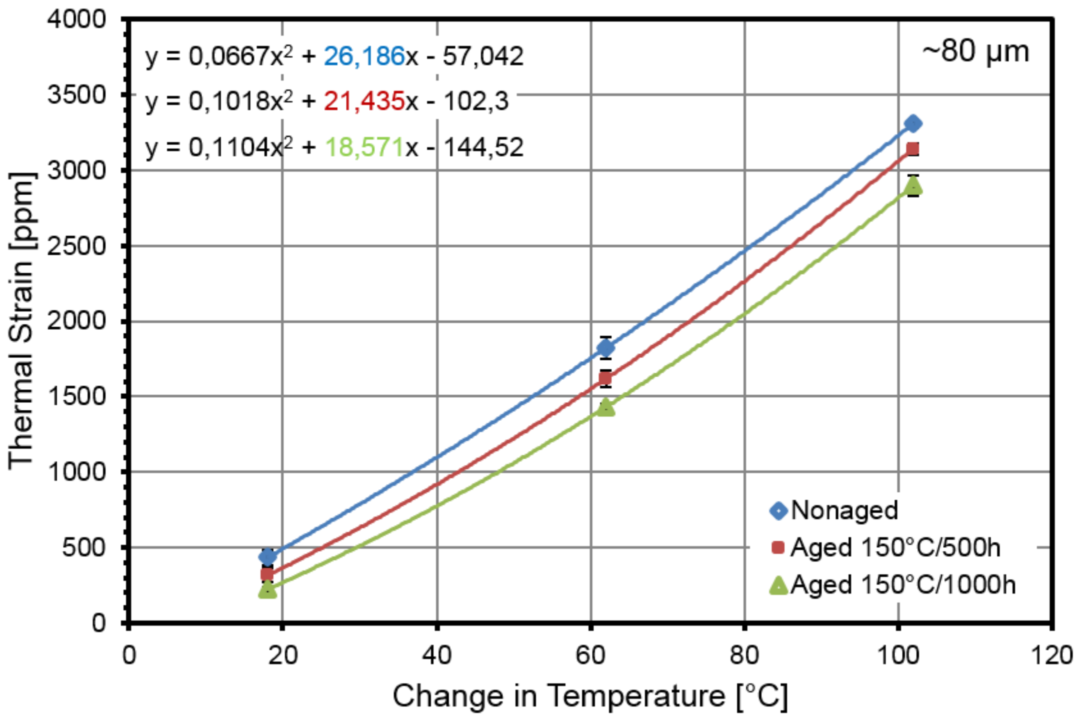

Figure 4.8. Thermal strain versus temperature change of a 80 µm solder gap starting from room temperature subjected to 80°C/3h, 150°C/500h and 150°C/1000h heat treatments.

When the solder gap becomes smaller the IMC thickness gets more and more important. An increase of the IMC layer from 2.5 µm to 8.4 µm after thermal aging will influence the resulting CTE value especially in thin solder gaps. According to literature data the values of thermal expansion for the IMC phase Cu_6Sn_5 and Cu_3Sn are found to be 19.0 ppm/°C and 16.3 ppm/°C [65]. These results show that with increasing aging time the overall CTE of a thin solder joint (80 µm) resembles more the CTE value of their IMC, due to the increase of the IMC volume proportion. A thicker solder gap (120 µm) shows that with increasing aging time the CTE of the joints are close to their associated Cu substrate with a CTE of 16.9 ppm/°C [66]. The results of the present investigation indicate that the growth of the IMC layer decreases the overall CTE value with a more prominent effect in thinner joints (Figure 4.9). However this effect is concurrent with increased brittleness, Kirkendall voiding and general inferior tensile properties.

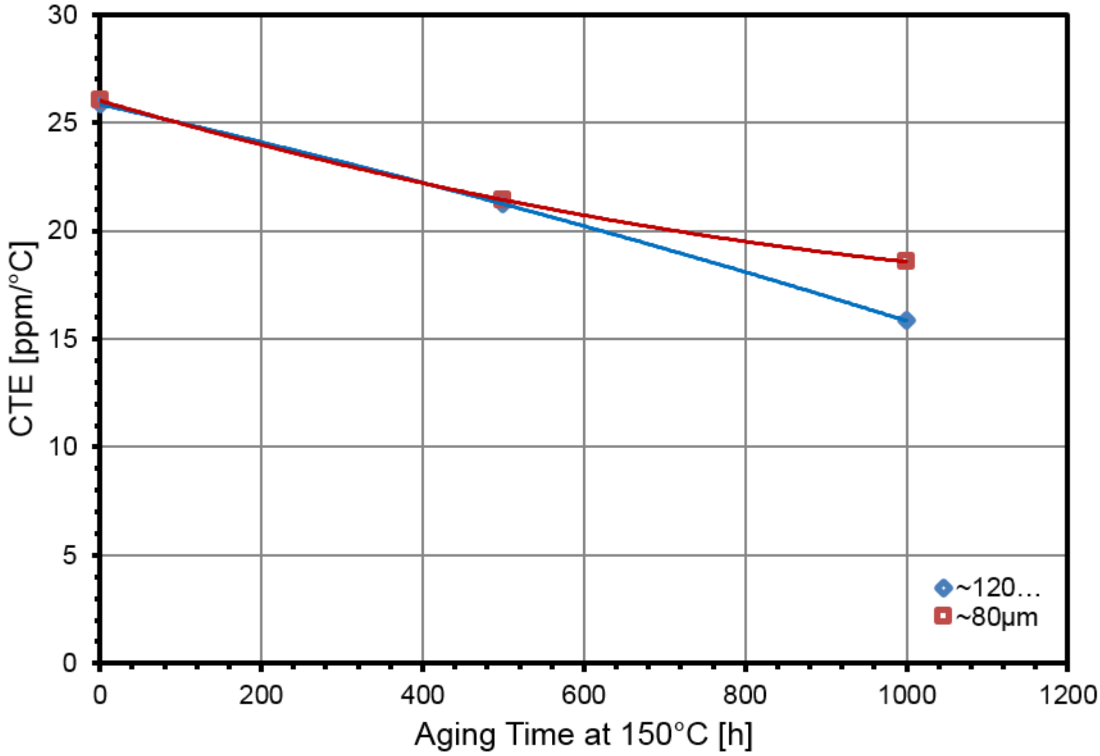

Figure 4.9. Calculated CTE values of two SnAgCu gap thicknesses (80 µm and 120 µm) with respect to their aging time at 150°C.

4.3. Summary

A laser interferometric system was applied to measure the local thermal strain of miniaturized Sn3.5Ag0.75Cu joints with a thickness of 80 µm and 120 µm. An overall CTE of 26.1 ± 0.2 ppm/°C was observed for miniaturized solder gaps. A fundamental knowledge of the relationship between the intermetallic compound and the solder gap thickness is essential to interpret change of the calculated overall CTE of a solder gap by aging. The measurements showed a decreasing trend of thermal expansion of the solder joints with increasing aging time up to 1000h at 150°C. It can be observed that the growth of the IMC layer with increasing aging time resulting in an increased ratio of IMC thickness to the gap size results in a decrease of the overall CTE of the miniaturized solder joints. The result has shown that it is necessary to determine thermal properties of the used elements in the actual dimensions and geometries.

CHAPTER 5
Development of a Low Cycle Mechanical Fatigue Setup for Shear Loading

5.1. Introduction

Lifetime modeling and prediction of fatigue life of microelectronic devices requires the study of the complex thermo-mechanical properties of their constituent multilayered material systems. Especially miniaturized solder joints, which count as critical sites in the devices are continuously subjected to further miniaturization and harsher environmental and loading conditions. Reliability of solder joints in microelectronics is commonly assessed under following loading conditions: firstly thermal cycling (typically from -40°C to 125°C) and secondly mechanical vibration and shock loading based on standard procedures (e.g. JEDEC, MIL …).

Thermal cycles are normally handled at a very low frequency level, which may require extremely long testing times to failure. For example, for SMDs used in automotive applications a temperature range is chosen between -40°C and 125°C with a required time of 1h per cycle. Thermal cycling testing procedures are designed to reproduce the failure modes, which may occur during the operational life. Reduction of testing time is achieved by accelerated thermal tests, which are commonly conducted at high ΔT_S to induce early failure in the devices. Another approach is application of accelerated mechanical testing to replace the thermally induced strains by means of equivalent mechanical strains in order to reduce the testing time. The aim is to induce failure modes, which resemble those occurring during the thermal cycling procedures and under service conditions in automotive applications. For this purpose an isothermal mechanical fatigue testing set-up for selected types of solder joints was designed and developed as described in the following section.

5.2. Specimen Characteristics of Selected Solder Joints

Isothermal low cycle mechanical fatigue experiments were conducted on two types of solder joints. For the first set of tests commercial Bi-polar ceramic capacitors with Sn3.5Ag0.75Cu meniscus type solder joints as mounted on PCB substrates were used. The samples were designed and fabricated for shear fatigue loading mode as shown schematically in Figure 5.1. The configuration of the sample allows inducing cyclic shear strain in the solder joints by using a displacement controlled mechanical fatigue testing set-up. The symmetrically arranged SMD capacitors, which were soldered on the Cu pads of the two PCB strips, were subjected to cyclic loading by mounting the PCB strips into a specially developed precision tensile stage, which was placed into the tensile machine. Figure 5.2 shows the details of the SMD sample design (PCB), which will be clamped into the precision micro-tensile stage, which was used for careful mounting of the delicate ceramic devices. After fixation, the marked points (black line in Figure 5.2) are cut through so that the applied load can only act on the meniscus type solder joints. FEM simulations were conducted to determine the amount of cyclic displacements d_c required for inducing a certain amount of shear strain in the solder joints as described in the following section.

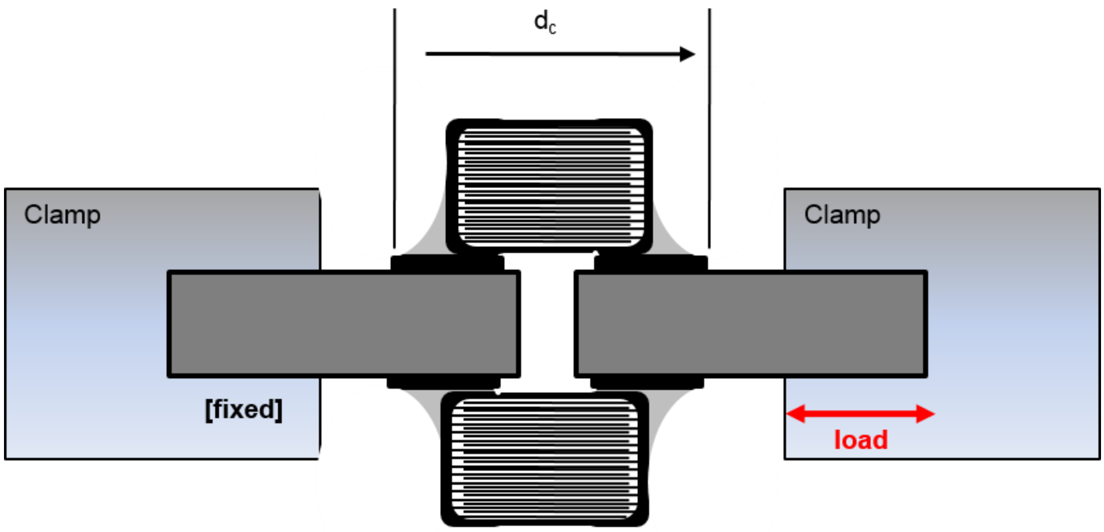

Figure 5.1. SMD capacitor design for low cycle fatigue testing.

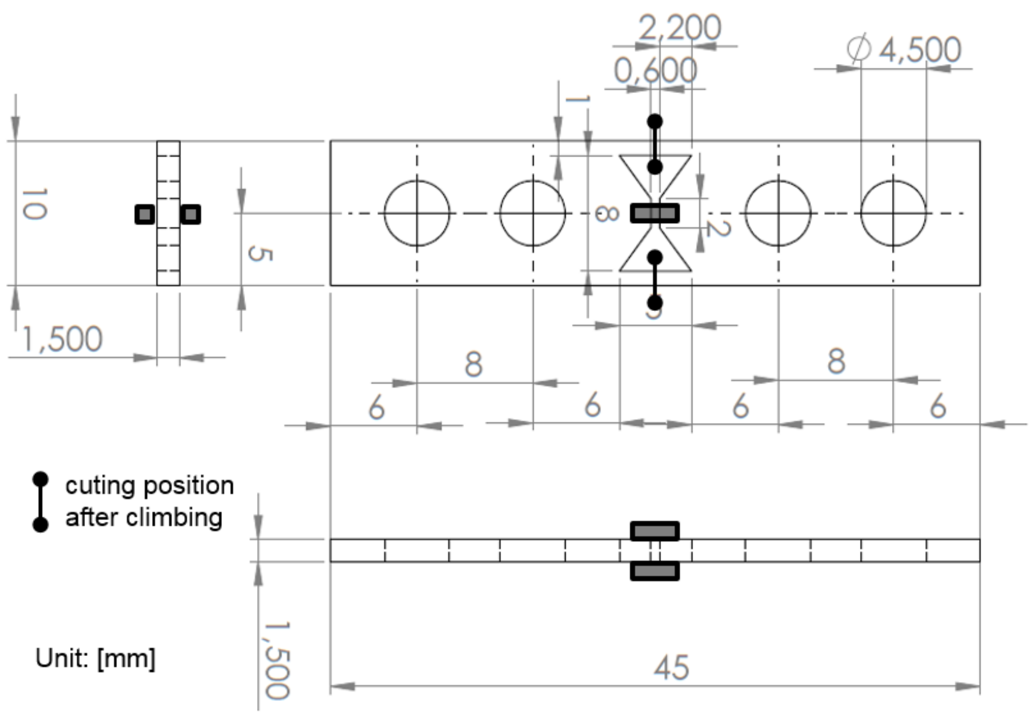

Figure 5.2. PCB designed for shear fatigue loading.

For the second test series ball grid array type (BGAs) solder joints were chosen with a tin-lead solder ball diameter of 600 µm and Cu electrodes on both sides. The test samples were prepared out of commercial BGAs and consisted of 6 solder balls. As shown in Figure 5.3, the PCB was divided into two parts to allow a displacement controlled relative movement of the three solder balls at each side of the sample (Figure 5.3). The samples were subjected to cyclic shear loading by placing and fixing the PCB into the above described precision micro-stage.

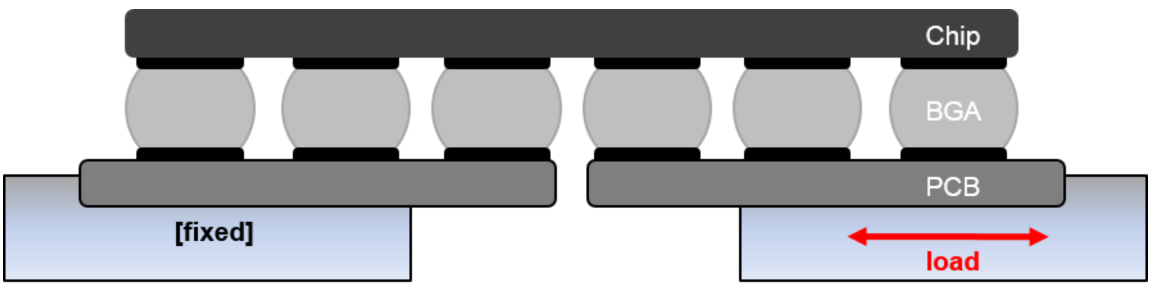

Figure 5.3. BGA testing design for the low cycle fatigue setup.

5.3. Low Cycle Mechanical Fatigue of Selected Samples

5.3.1. Thermal vs. Mechanical Cyclic Loading of SMD

In the framework of the Project A.7-11 “Life time of functional multilayer ceramic systems“, Sevecek designed a FE model based on the SMD component geometry (Figure 5.4) to define the boundary condition for the mechanical cycles based on thermal cycles.

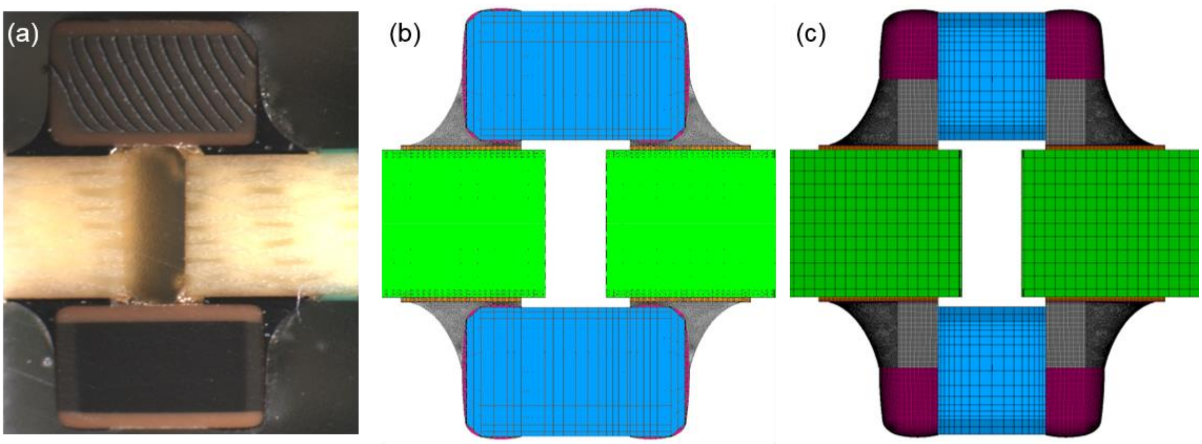

Figure 5.4. FE model based on the SMD component geometry: (a) section through the SMDs, (b) section through the FE model and (c) sideview of the FE model.[2]

The load steps for thermal cycling are -40°C up to 125°C with a dwell time of 23 min at peak loads as used in the automotive industry. The accumulated effective creep strain $\varepsilon_{\mathrm{eq,acc}}^{\mathrm{cr}} = \sum \Delta\varepsilon_{\mathrm{eq}}^{\mathrm{cr}}$, defined by the von Mises Equation, was used to compare thermal and mechanical cycles. The values of accumulated creep strain were compared with the focus on the solder volume under the ceramic component. The simulations showed that isothermal cyclic mechanical testing at 80°C is required in order to obtain the equivalent creep strain in the solder joints subjected to thermal cycling with a ΔT of 165K. Figure 5.5 shows a comparison between the calculated amount of the creep strain after 5 thermal (a) and isothermal mechanical (b) cycles as well as the strain distribution in the solder joint in both loading conditions.

[2] Project A.7-11 „Life time of functional multilayer ceramic systems“
Material Center Leoben GmbH, O. Sevecek

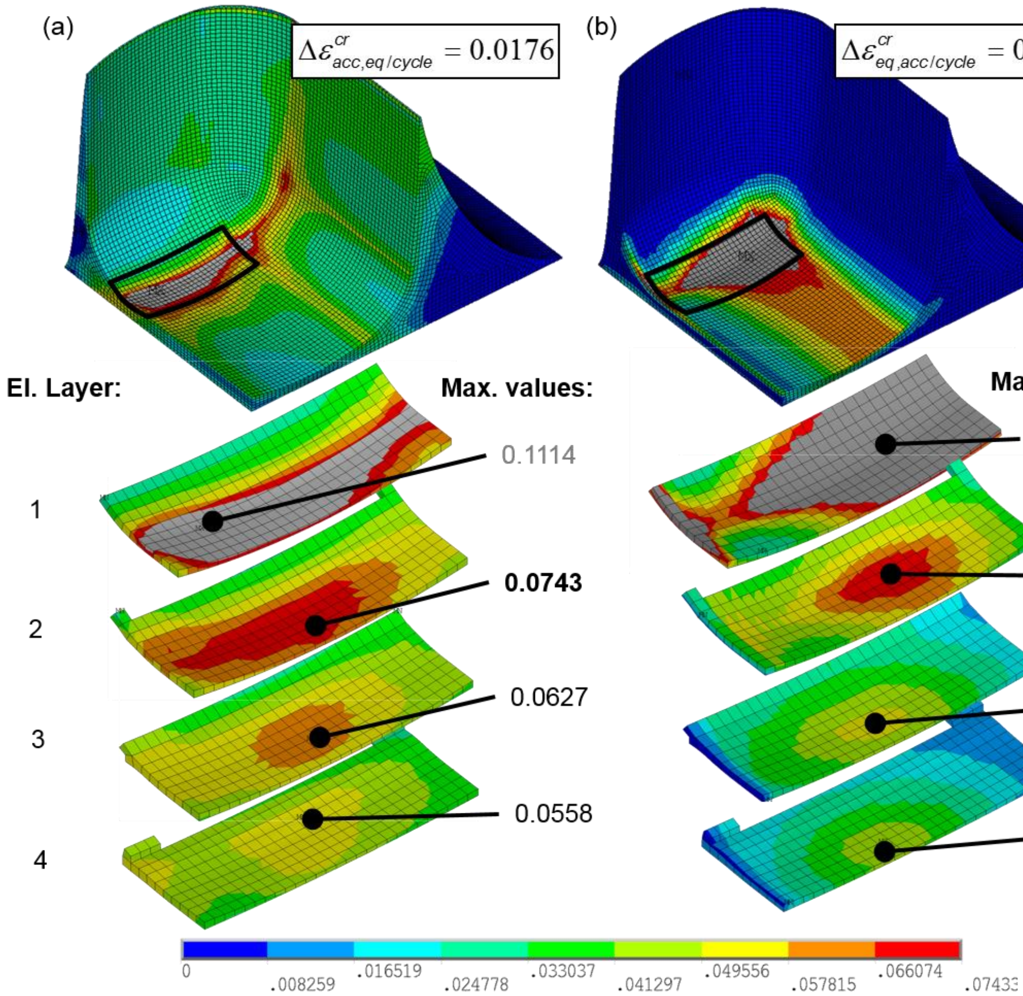

Figure 5.5. Accumulated creep strain in the solder volume. Comparison 5 cycles of (a) thermal loading between -40°C up to 125°C vs. (b) thermo mechanical loading (4.5µm) at 80°C.[3]

A nearly similar creep strain distribution in both loading scenarios was found by comparing the maximum accumulated creep strain values. Finally a total displacement amplitude of 9 µm at a frequency of 10 mHz and test temperature of 80°C (4.5 µm for the ¼ FE mode) was determined to produce the same amount of thermally induced accumulated creep strain per cycle during the mechanical loading. Based on these results the testing conditions for mechanical fatigue testing of solder joints in SMD capacitors were defined.

[3] Project A.7-11 „Life time of functional multilayer ceramic systems“
Material Center Leoben GmbH, O. Sevecek

5.3.2. Cyclic Mechanical Shear Fatigue Measurements

Low cycle fatigue tests were performed using a micro tensile testing machine (µ-strain instrument ME30-1 from Messphysik, Austria) shown in Figure 5.6. The force was measured with a load cell of 100 N capacity. Displacement controlled fatigue tests were performed by using a sinusoidal wave profile and tension-tension loading mode. All tests were conducted at 80°C and without a dwell time at peak loads by using a hot air blower to heat the specimen with an accuracy of ± 1°C.

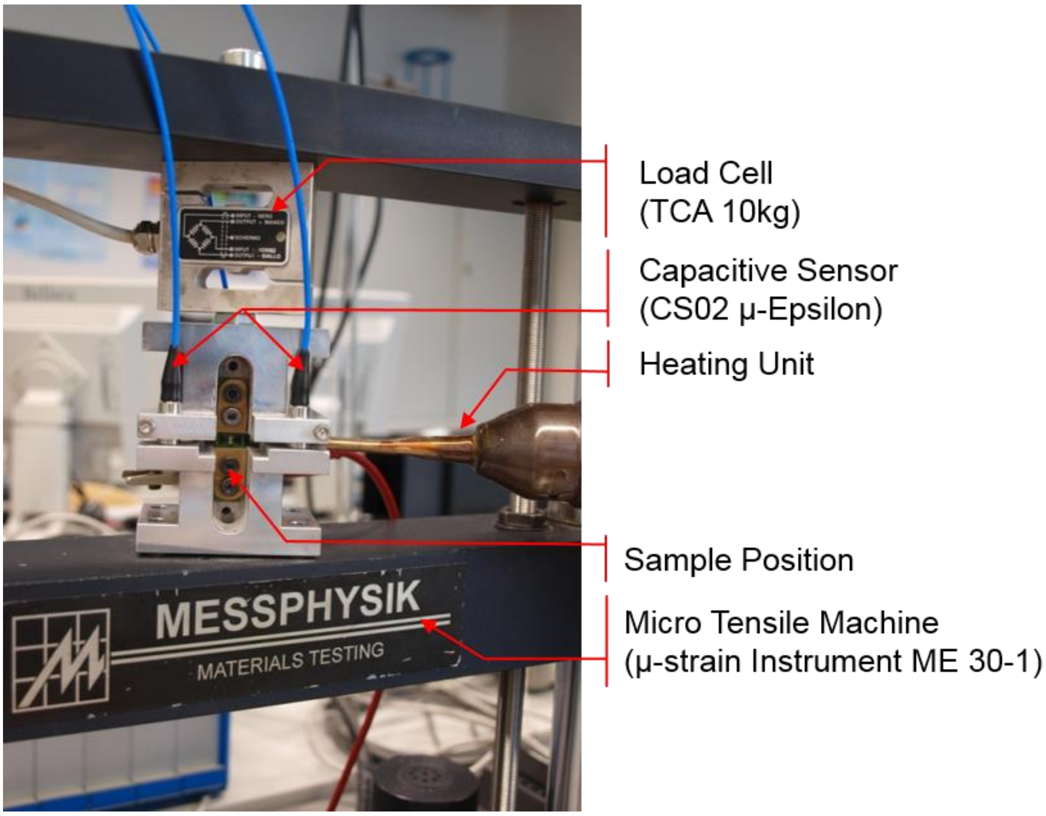

Figure 5.6. Low cycle mechanical fatigue testing setup.

The sinusoidal displacement profile was measured and controlled by three capacitive sensors (CS02 from µ-Epsilon) with a dynamic resolution of 4 nm (Table 8). The three sensors are placed round the specimen in a 120°C arrangement to adjust possible tilting moments during the cyclic loading. The displacement is measured with a maximum distance of 200 µm from the edge of the solder meniscus. According to the FEM calculations the lowest displacement range for mechanical cyclic loading was 9 µm. The high resolution capacitive sensor was selected to achieve the best performance during cyclic loading. Figure 5.7 shows the precision micro tensile stage with the integrated capacitive sensors (CS01).

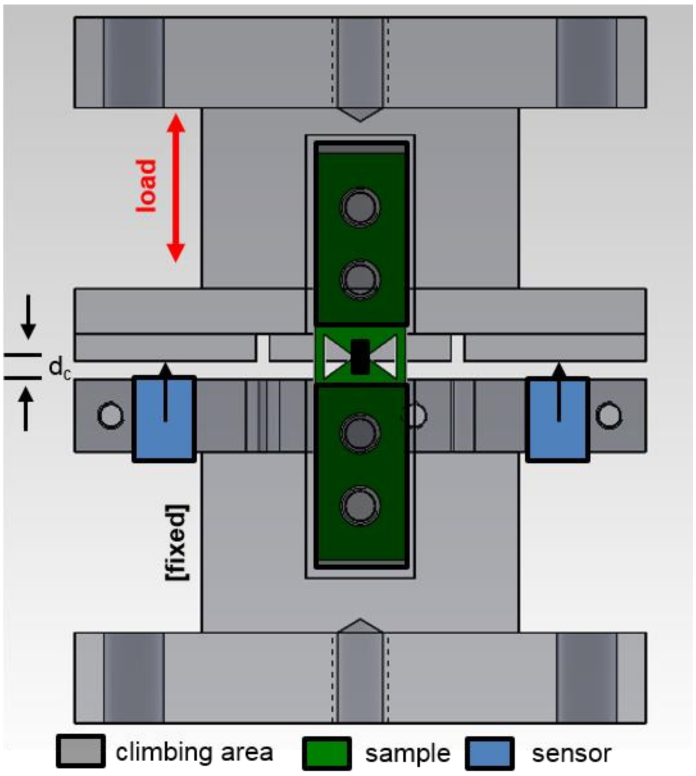

Figure 5.7. Precision micro-tensile stage of the LCF test setup including capacitive sensors to measure the displacement dc on the solder joint.

Table 8. Data of the capacitive sensor CS02 from μ-Epsilon.

Sensor Type	CS02
Measuring range	200 μm
Linearity	0.04 μm
Resolution (static, 2 Hz)	0.15 nm
Resolution (dynamic, 8.5 kHz)	4 nm
Temperature range (operation)	-50 … +200°C
Temperature range (storage)	-50 … +200°C
Temperature stability sensitivity	-2 nm/°C
Sensor dimensions	∅6 x 12 mm
Active measuring area	∅2.3 mm

Calibration measurements were conducted to correlate the adjusted displacement of the traverse to the displacement of the SMD samples as measured by the capacitive sensors. The relationship between the adjusted and measured displacement is given in Figure 5.8. The difference between the measured displacement results from the stiffness of the tensile machine and the precision stage and the clamped PCB of the sample. The calibration curve shows that a displacement of 40 µm of the traverse results in a displacement of 15 µm of the solder joints.

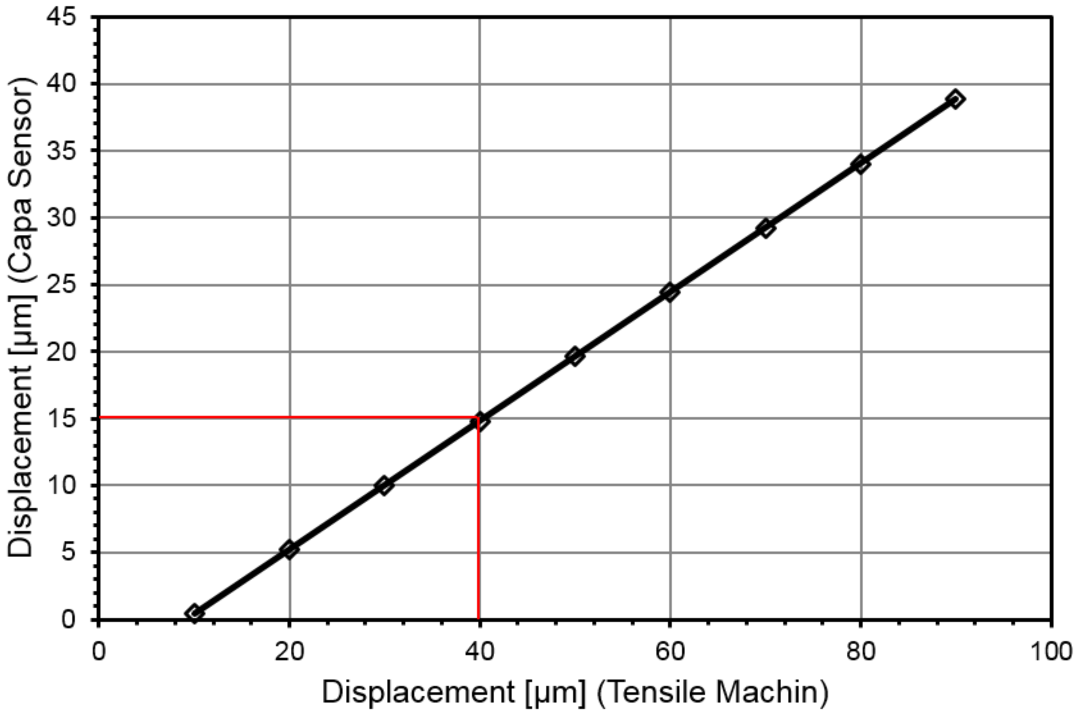

Figure 5.8. Relationship between the set and the measured displacement for LCF.

5.3.3. Cyclic Isothermal Mechanical Fatigue of SMD Capacitor

The symmetrically arranged SMD capacitor sample is mechanically cycled with a frequency of 10 mHz in the range of 9 µm up to 20 µm for 10^3 cycles at a testing temperature of 80°C. The 10^3 cycles were chosen according to the number of cycles which commonly lead to cracking of solder joints during the thermal cycling tests. Furthermore low cycle isothermal fatigue studies of similar SMDs report solder joint failure in the first 10^3 cycles [67][68]. Figure 5.9 gives an overview of the hysteresis development over the first 800 cycles at a measured displacement of 17.9 µm. The cyclic development of the hysteresis loop in the first 700 cycles shows a parallel reduction of the shear force at constant displacement (Figure 5.9a). In the last 100 cycles the hysteresis rotates in the clockwise direction until fracture (Figure 6.9b). A further increase of the total displacement amplitude resulted in an earlier hysteresis development of case (b). Total cyclic displacement amplitudes <17 µm have shown a parallel downward shift of the hysteresis over the first 10^3 cycles (a).

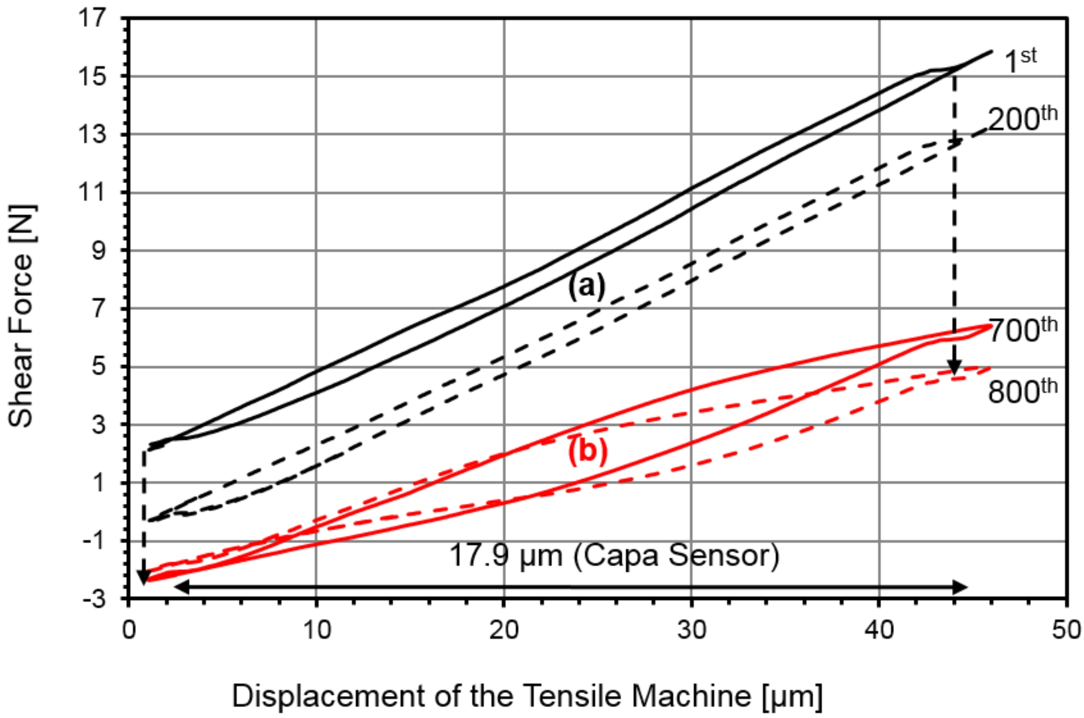

Figure 5.9. Hysteresis loop development of the SMD capacitor tested at a frequency of 10 mHz ((a) crack propagation through the ceramic body; (b) transition of the fracture into the solder meniscus).

Metallographic cross sections of the tested samples showed a crack initiation in the ceramic body of the SMD which propagates through the ceramic element and ends at the upper end of the meniscus type solder joint (Figure 5.10). Further investigation on untested samples showed the existence of micro-cracks in the ceramic due to the fabrication process of the special SMD testing design. It is assumed that the presence of a slot in the PCB in combination with symmetrically positioned devices led to high stresses after the soldering process, which resulted in a crack initiation in the ceramic. Therefore the hysteresis development of (a) can be interpreted as crack propagation in the brittle ceramic body and (b) as transition of the crack into the ductile meniscus type solder joint. It was concluded that the present geometry was not suitable for the fatigue investigations due to probable presence of the micro cracks in the SMD capacitor.

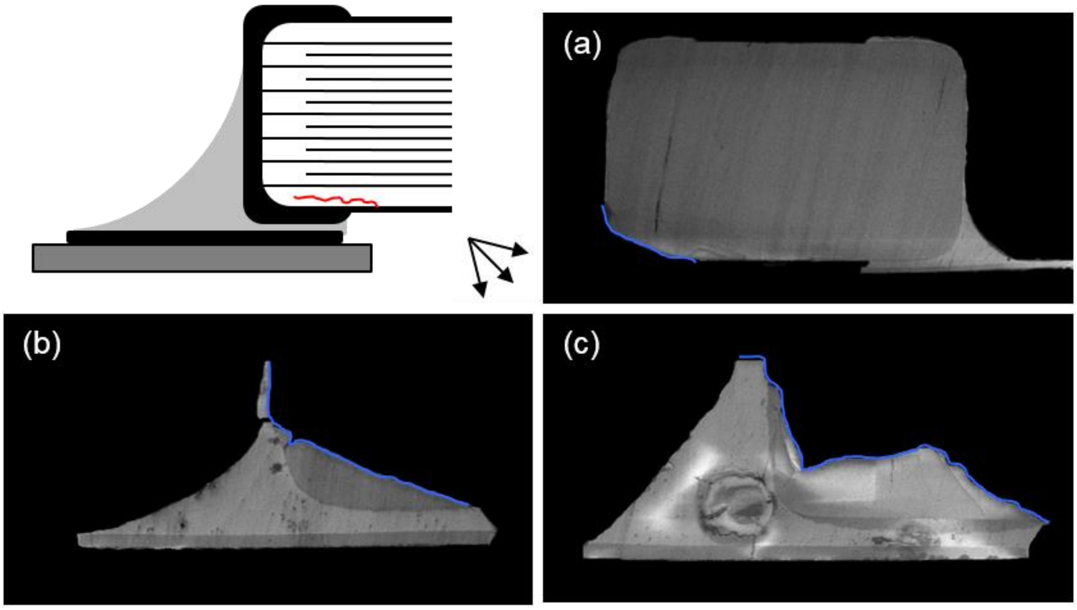

Figure 5.10. Fracture evolution of tested SMDs, influenced by predamaging due the fabrication process of the special testing design ((a-c) cross sections of SMD samples tested at a displacement of 17.9 µm after around 800 cycles).

The low cycle fatigue tests are continued with BGA samples as shown in Chapter 5.2 to demonstrate the functionality of the developed thermo-mechanical fatigue setup. The focus of the next chapter is to show that the developed method is a promising approach for replacement of thermal cycles with accelerated thermo-mechanical cycles.

5.3.4. Cyclic Isothermal Mechanical Fatigue of BGA

BGA samples with a slot in the PCB were tested at a frequency of 10 mHz with an amplitude of 15 µm up to 40 µm at 80°C for 1000 cycles in tension-tension loading mode. Figure 5.11 shows the hysteresis loop shape of 1st, 200th, 400th and 700th cycle at a displacement of 38.8 µm. In the first 200 cycles a stress relaxation is observed due the downward shift of the hysteresis loop. The hysteresis shapes >200 cycles suggest a softening of the solder joints until failure due to the total reduction of the shear force over the number of cycles shown in Figure 5.12. A confirmation of the observed effects can be taken from the literature [67][69]. Possible material cyclic deformation phenomena are memory effect, cyclic hardening, cyclic softening, cyclic stress relaxation and cyclic creep. They are classified over the time dependent hysteresis shape and are an important ingredient for computer-based simulations [70].

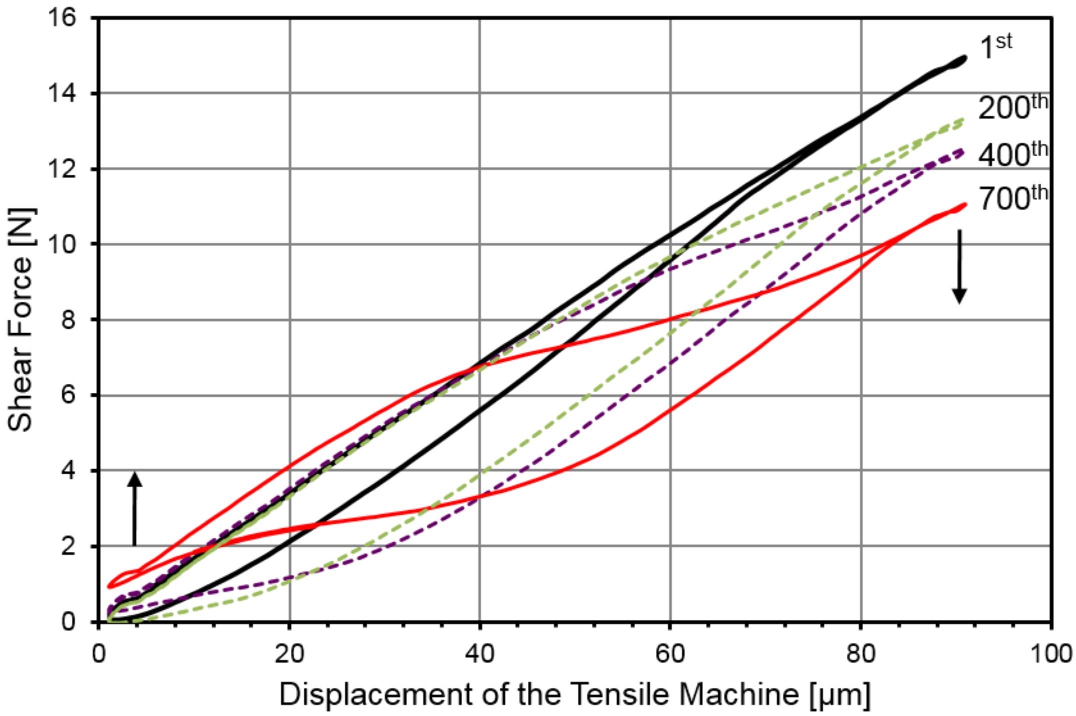

Figure 5.11. Hysteresis loop development of the BGA tested at a frequency of 10 mHz.

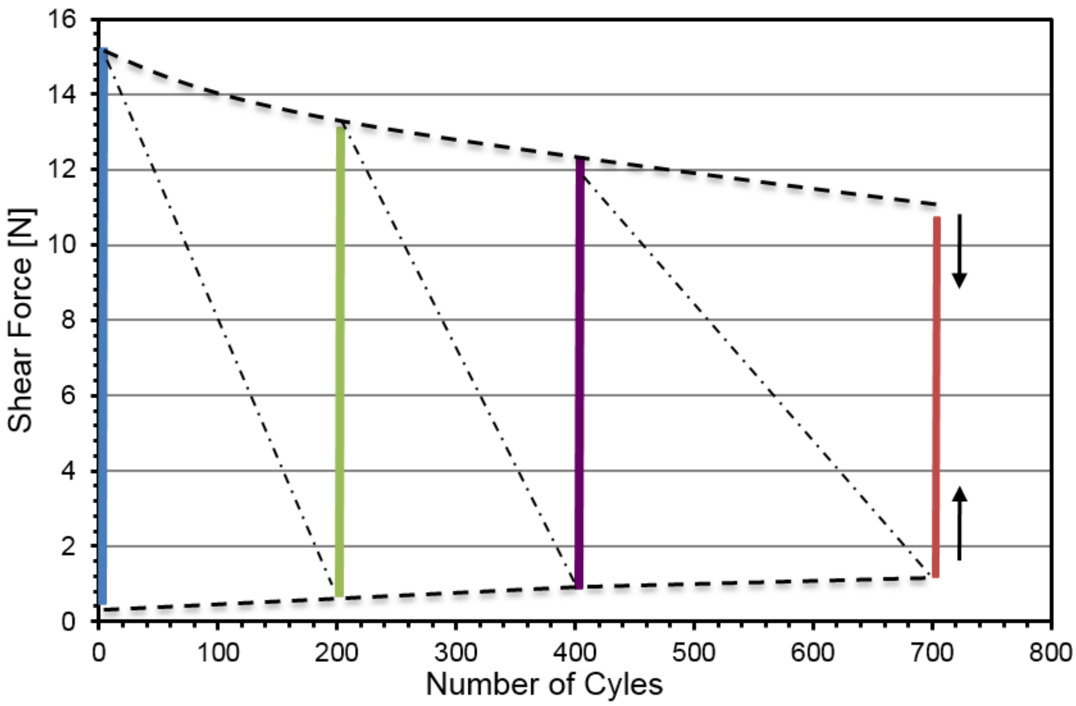

Figure 5.12. Change of the shear force under cyclic deformation of the BGA array until failure.

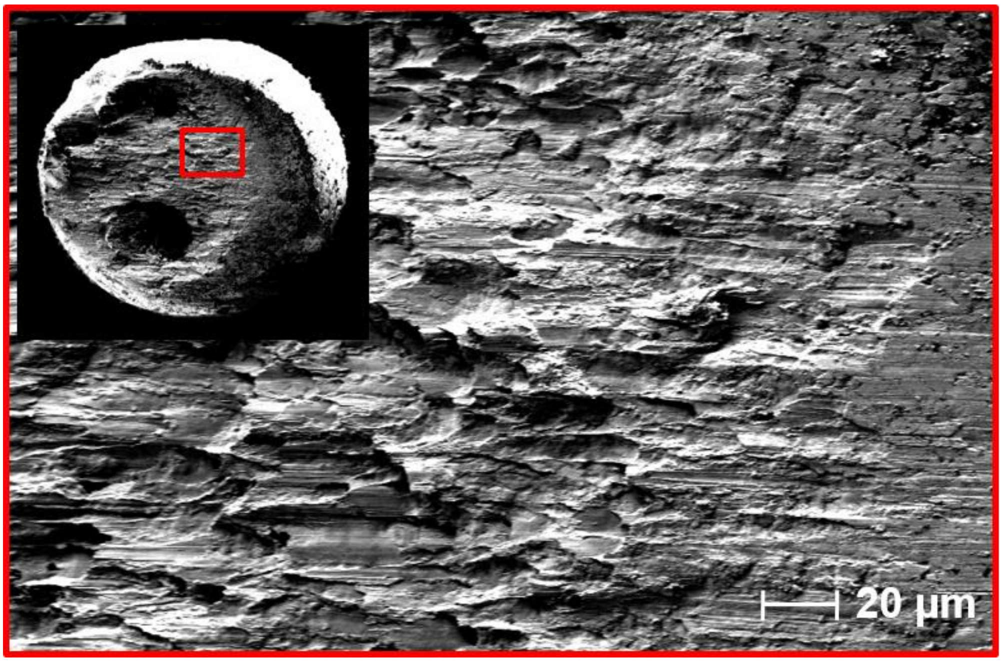

Figure 5.13. Fracture pattern of the BGA after 705 cycles at 10 mHz.

Figure 5.13 shows the fracture pattern of one of the 6 BGAs after 705 cycles (total displacement amplitude of 38.8 µm) at a frequency of 10 mHz. A crack in the interface between solder ball and the ground electrode was observed. This result of low cycle fatigue on BGA is in conformity with the results found in the literature [69]. Isothermal low cycle fatigue tests with BGAs with varying loading angles are performed by Park et al. with a similar hysteresis development until fracture.

These first results approve the feasibility of the developed set-up and methodology for low cycle fatigue testing of microelectronic components in the micron range. The mechanical fatigue testing set-up in combination with finite element analysis may be considered as one of the first steps for replacement of thermal cycles in an accelerated thermo-mechanical manner. However, further investigations exceeded the scope of the present work. The complexity of this task requires further extensive investigations including development of appropriate sample geometry for different types of solder joints. Further steps would be comparison of lifetime curves (S-N) and corresponding fracture mode with thermal cycles for different solder types and alloys. An important aspect would be comparison of the mechanisms of thermal and isothermal solder fatigue such as recrystallization effect as reported for lead-free solder joints after thermal cycling. Stored energy in the solder crystal due to thermal cycling is released in the form of defects and dislocations, leading to recrystallization at the interface of the solder joints [71]. Detailed microstructural investigations would provide more insight into the complex mechanisms of fatigue of lead-free solders.

5.4. Summary

In the present chapter a low cycle mechanical fatigue testing set up for solder joints in SMDs was developed to replace the thermally induced strains by means of equivalent mechanical strains in order to reduce the testing time. The developed method was demonstrated by using two different electronic devices: an SMD capacitor and a BGA array. Thermo-mechanical FEA simulations were performed to define the suitable boundary conditions for the LCF setup. The amount of displacement required to induce accumulated creep strain values equivalent to a certain temperature difference was calculated. FEM results also confirmed that by using the designed samples and mechanical testing set-up, the distribution of strain in the solder joints is similar to that observed as a result of thermal mismatch during the thermal cycling of the SMD. Nonetheless fatigue experiments on the SMD capacitors did not show the desired results. It was found that during the soldering process of the two SMDs on the PCB micro-cracks might be initiated in the ceramic part. In conclusion, an improved sample preparation process is required to produce defect free samples for LCF tests. The functionality of the developed setup was successfully demonstrated by using BGA solder joints. With the obtained results a possible low cycle fatigue setup was shown to test solder joints of electronic devices according to displacements in the micron range. The method is the first step in the replacement of thermal cycle tests by accelerated isothermal mechanical tests.

CHAPTER 6
High Cycle Fatigue of Surface Mounted Device Solder Connection

6.1. Introduction

Surface mounted devices (SMDs) in microelectronics are subjected to electrical, thermal and mechanical loads during service. Especially in automotive applications vibrational loading in combination with temperature effects may lead to failure of the devices due to mechanical fatigue. Thus the reliability of the devices is highly influenced by the mechanical and thermal response of the used solder joints [34]. Thermal cycling tests using temperature ranges between -40°C to 125°C with a dwell time of about 1 hour are commonly used for reliability testing of SMDs in automotive applications [27]. In this case time to failure is about several thousand hours. Reduction of testing time can be achieved by increasing the temperature hub and reducing the dwell times. One disadvantage of thermal acceleration is the possible occurrence of undesired failure modes due to low homologous temperature of the solders.

A new approach for studying the thermo-mechanical response of solder joints subjected to cyclic loading is application of mechanical isothermal high and low frequency fatigue testing. Combining thermal and mechanical loads allows realizing realistic service conditions in an accelerated manner. While the evaluated testing temperature of 80°C can accommodate the time dependent creep behavior of the solder joints, high-low frequency mechanical loads result in accumulation of strain per cycle in a very short time.

The aim of the present chapter is the investigation of fatigue response and failure modes of solder joints in SMD capacitors subjected to high frequency isothermal fatigue. For this purpose vibrational fatigue response of Sn3.5Ag0.75Cu lead-free solder alloys at RT and 80°C were investigated using commercial bi-polar ceramic capacitors. Reliability and lifetime of the solder joints were discussed with respect to their microstructural features, constraint effects, tensile properties and testing temperature. Feasibility of application of the developed accelerated mechanical testing procedure for assessment of thermo-mechanical reliability of solder joints in SMDs is discussed.

6.2. Specimen Characteristics for HCF

Commercial Bi-polar ceramic capacitors with Sn3.5Ag0.75Cu meniscus type solder joints as mounted on PCB substrates were used for fatigue experiments. A schematic illustration of the SMD capacitor is shown in Figure 6.1. The ceramic body is primarily made of $BaTiO_3$ multiple layers with intermediate Ni electrode layers. Cu is used as external electrode on the capacitor with a Ni layer on the external electrodes against solder heat. The capacitor is classified as C2012 X7R 1H 334 K, which includes the information about size, dielectric, rated voltage, capacitance and capacitance tolerance of the ceramic component listed in Table 9.

Table 9. Specifications of the main body of the used SMD capacitor.

C2012 X7R 1H 334 K

Main body:

Size (C2012)	L 2.00 x W 1.25 x T 1.25 mm
Dielectric (X7R)	-55 ~ +125°C; ± 15%
Rated voltage (1H)	DC 50 V
Capacitance (334)	330000 pF; 330 nF
Capacitance tolerance (K)	± 10%

Other specifications

PCB (printed circuit board)	Thickness: 1.5 mm
	Surface: chemical tin
Lead-free solder	Sn3.5Ag0.75Cu
Dielectric	CC 0805 / X7R

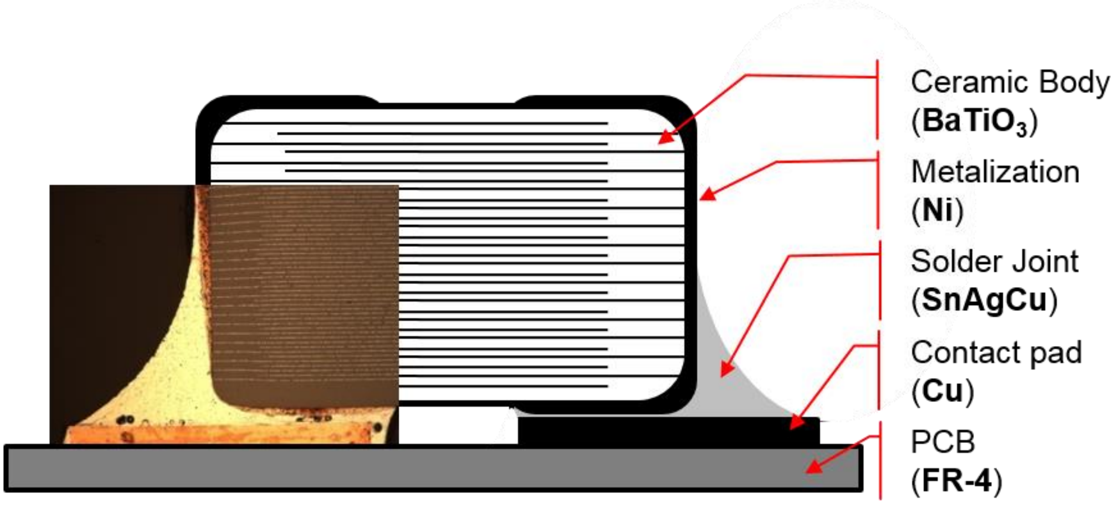

Figure 6.1.Schematically illustration of the capacitor soldered on PCB.

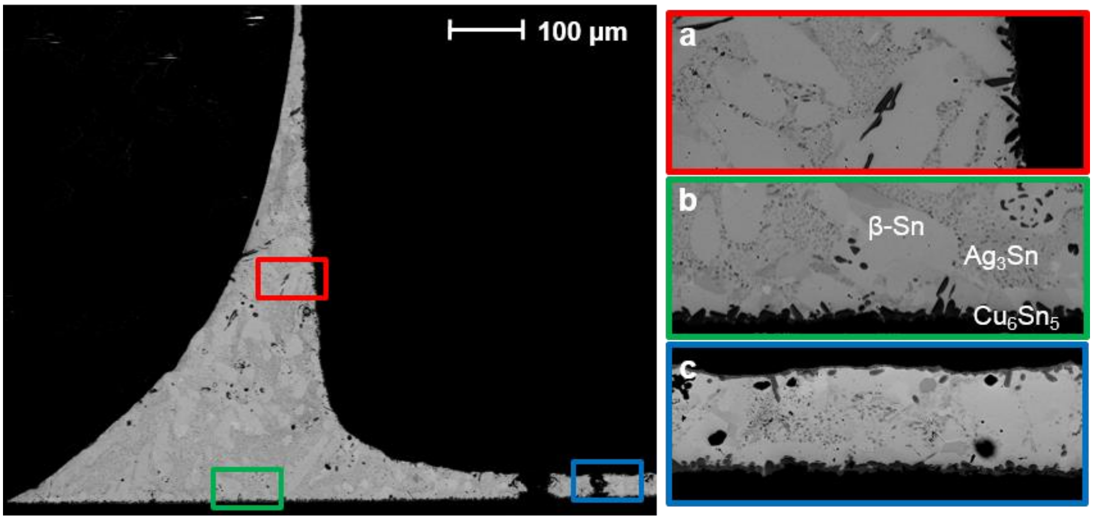

Figure 6.2.Overview of the tested bi-polar SMD with the microstructure of solder joint at different positions.

Figure 6.2 shows the distinct variety in the length scales of intermetallic compounds formation Cu_6Sn_5 at the solder interfaces and the change of Sn grain size in the meniscus and the gap under the component. The ternary eutectic structure of the meniscus consists of coarse β-Sn structure and fine Ag_3Sn particles as well as scallop shaped Cu_6Sn_5 intermetallics at the interface (a and b). The small-scaled solder gap thickness in the range of 20 µm consists of finer Sn grains and a planar Cu_6Sn_5 structure (c). The relationship between the solder size/volume and the microstructure can be found in the literature [37][38] and was studied in Chapter 2.3. With the miniaturization of the solder joints, the IMC proportion to the solder joint increases, which results in a significant change of the mechanical property of the solder joints.

Variation of the solder thickness due to the special geometry in these types of joints results in different local microstructures, affecting the mechanical response during tensile and fatigue loading. A study of the mechanical response of the solder joints with respect to the gap size and the microstructure was conducted using Cu/Sn3.5Ag0.75Cu/Cu model solder joints described in Chapter 2.4.

6.3. High Cycle Mechanical Fatigue of Surface Mounted Capacitor

6.3.1. Accelerated Mechanical Fatigue Measurements

An ultrasonic resonance fatigue testing system was used to induce forced cyclic vibrations in the SMD capacitor (attached on the specimen holder). The setup consists of ultrasonic transducer and an acoustic horn to amplify the longitudinal wave and a specimen holder. Displacement and strain varies along the half-wavelength of the specimen holder, with maximum strain distribution in the mid-section and maximum displacement distribution at the free end (Figure 6.3) [72]. Depending on the position of the device on the specimen holder, two loading scenarios can be applied. Either the solder joint is subjected to shear loading by placing the device in the direction of vibrational loading on the top of the specimen holder (Figure 6.3a), or a push-pull loading mode can be achieved by positioning the device perpendicular to the loading axis on the front face of the holder (Figure 6.3b). Depending on the loading type different damage modes are expected. Further details of this experimental set-up are also given in [29][73]. The primary aim of high cycle fatigue studies was to investigate the influence of microstructure and the testing temperature on the failure mode and crack path in the meniscus-type solder joints. For this purpose, shear mode loading during ultrasonic fatigue testing was chosen. This scenario corresponds to thermally induced stress in bi-polar capacitors inside automotive electronic components. The used setup for the accelerated shear test is shown in Figure 6.4.

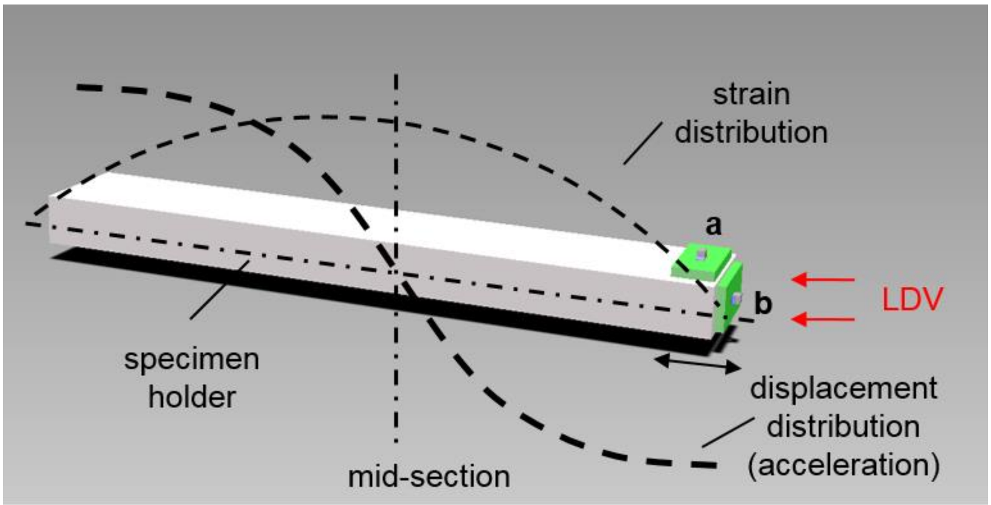

Figure 6.3.Schematic illustration of the fatigue testing set-up with sample position suggestion (a, b).

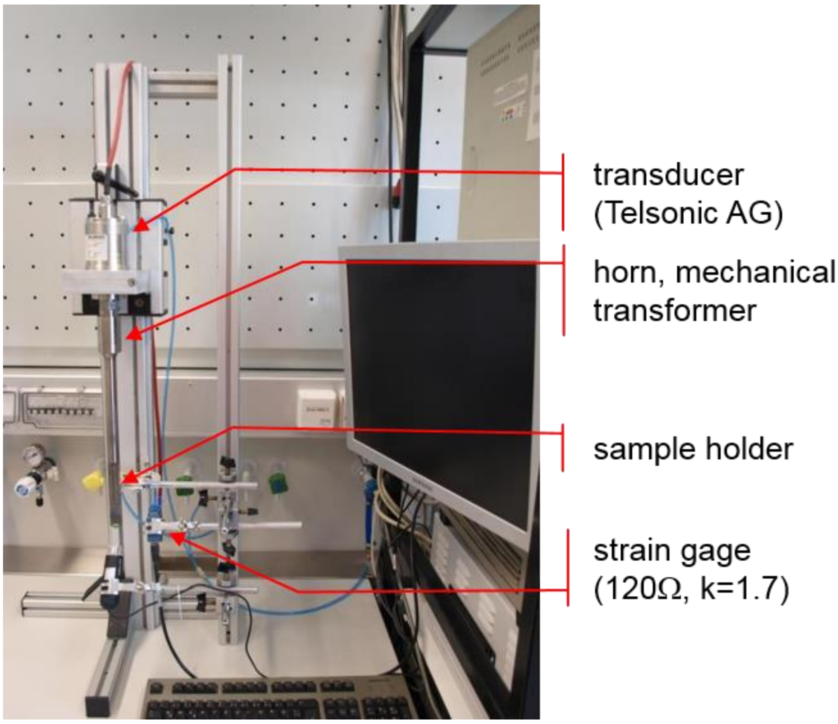

Figure 6.4.Setup of the 20 kHz shear fatigue test system.

The force induced in the joint is related to the mass of the SMD, the stiffness and the geometry of the micro joint. The acceleration of the device on the free end of the holder at 20 kHz was determined by using a laser Doppler vibrometer (LDV) for measurement of the cyclic displacement of the device. The average shear stress in the solder was calculated based on the mass of the component and the fracture surface of the solder joint (Figure 6.5). A soldered area of 2.6 mm^2 ($\pm$0.3 mm^2) was assumed for all the joints including the area of the voids in the solder joint. These voids were present in all the joints due to degassing of the solder pastes during the reflow process. The Bi-polar ceramic capacitors were accelerated in the range of $6x10^4$ up to $1x10^5$ g to determine the number of cycles to failure. The results are presented by means of S-N curves, i.e. shear stress amplitude vs. number of loading cycle.

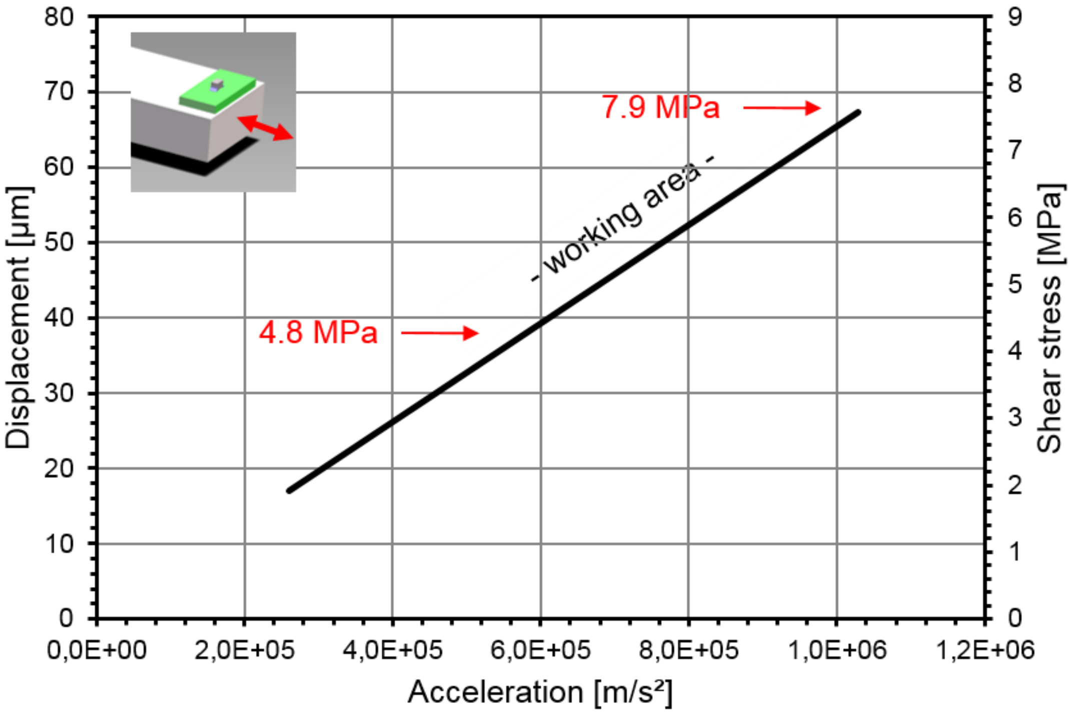

Figure 6.5.Relationship between the measured displacement and acceleration of the device and calculated shear stress in the solder joint.

As part of a COMET project supported by the Material Center Leoben GmbH, O. Sevecek has investigated HCF simulations of the solder joint of the SMD to illustrate the stress distribution in the solder joint subjected to shear loading at 20 kHz with an amplitude of 47.8 µm. Figure 6.6 shows the stress distribution in the solder joint at four significant points of the sinusoidal cyclic deformation. As expected, the main stress concentration is located near the interface to the Cu electrode and in the solder volume under the ceramic component. Furthermore, the crack initiation is expected at location with the highest shear stress (29.7 MPa).

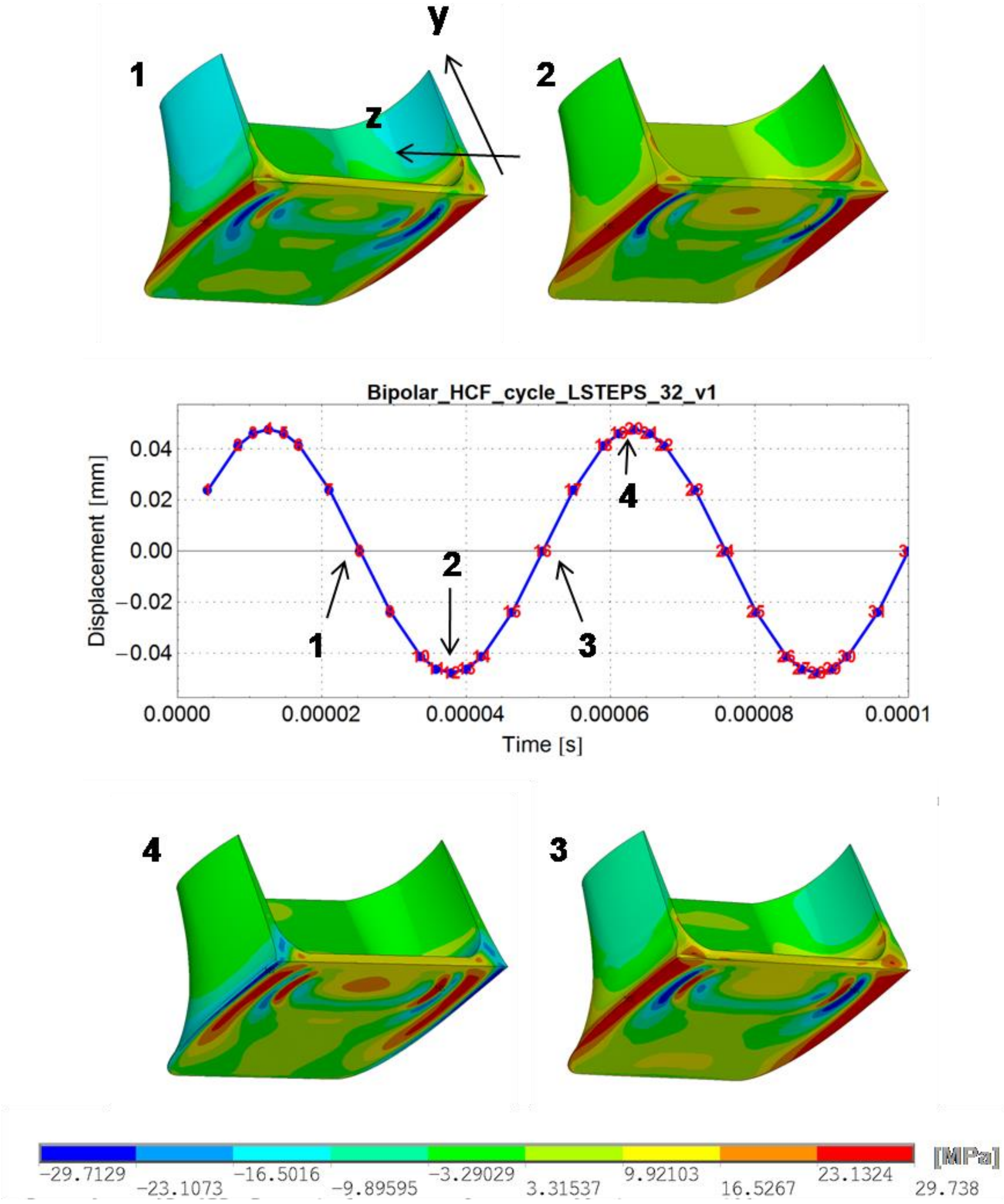

Figure 6.6. HCF simulation of the ½ FEM model of meniscus type solder joint at 20 kHz and an amplitude of 47.8 µm at four points of the cyclic deformation. [4]

[4] Project A.7-11 „Life time of functional multilayer ceramic systems“
Material Center Leoben GmbH, O. Sevecek

6.3.2. Accelerated Mechanical Shear Fatigue of SMDs

Figure 6.7 shows the S–N curves for the meniscus type Sn3.5Ag0.75 Cu solder joints in bi-polar SMD packages in non-aged conditions. The curve is plotted as function of shear stress and the number of loading cycles up to 10^9 cycles and shows a rather steep drop corresponding to fatigue testing at RT. The calculated average shear stress in the solder is between 4.8 MPa and 7.9 MPa. Depending on the load level different fracture types were observed. At high loading levels (7.1 MPa to 7.9 MPa) three types of fracture pattern are observed. Cu pad lift off, solder interface fracture, ceramic cratering or a combination of them occurred at a low number of cycles until failure. A detailed summary of all possible fracture surfaces which may occur at high loading levels are shown in Figure 6.9. High impact loading similar to drop tests is responsible for the variety of different fracture surfaces, which takes place in the Cu, in the solder, in the ceramic or in the interface between these.

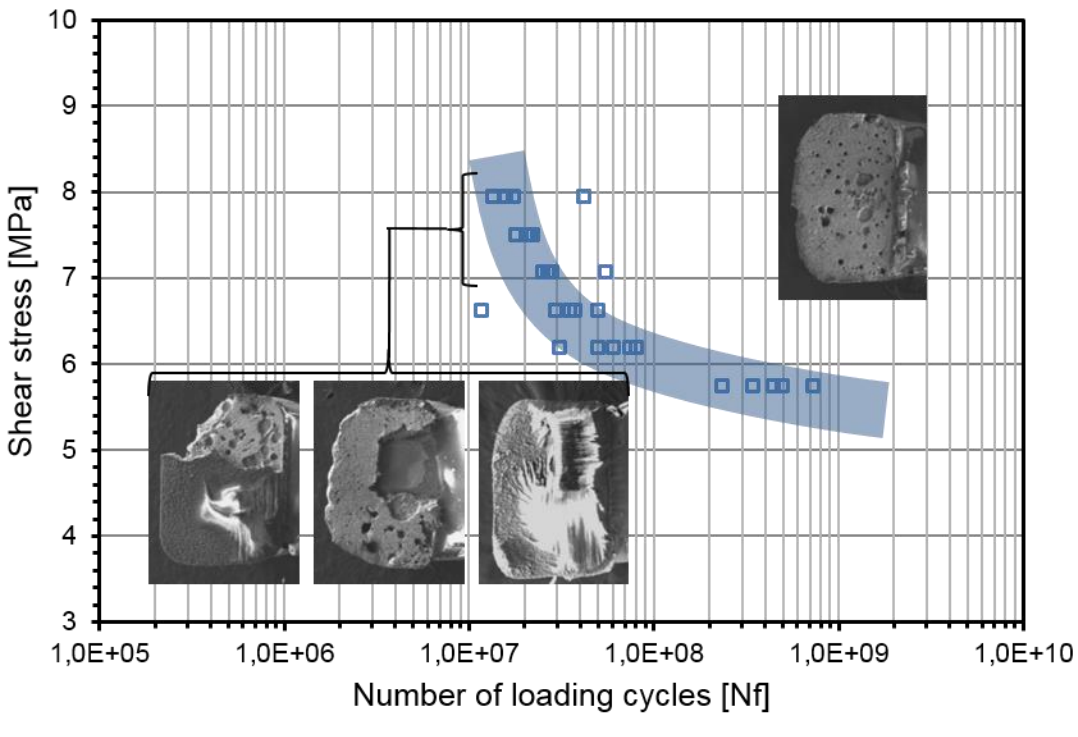

Figure 6.7. Lifetime of the meniscus type solder joints in SMDs at RT.

The Basquin equation (7) was used to characterize the fatigue life of SMDs by plotting $\log \sigma_s$ (σ_s, shear stress) versus $\log N_f$ (Figure 6.8). The lifetime of the nonaged SM-C device under shear loading in the x-orientation can be expressed as $\sigma =$

$28.04(N_f)^{-0.08}$, with σ_f' being the fatigue strength coefficient and *b* the fatigue strength exponent or Basquin exponent (-0.05 to -0.12). The obtained fatigue exponent of 0.08 is similar to those reported for SnAgCu values (b=0.073) [74]. The fatigue strength coefficient of 28.04 represents the fracture shear stress limit in MPa of the Sn3.5Ag0.75 alloy under static shear loading [75].

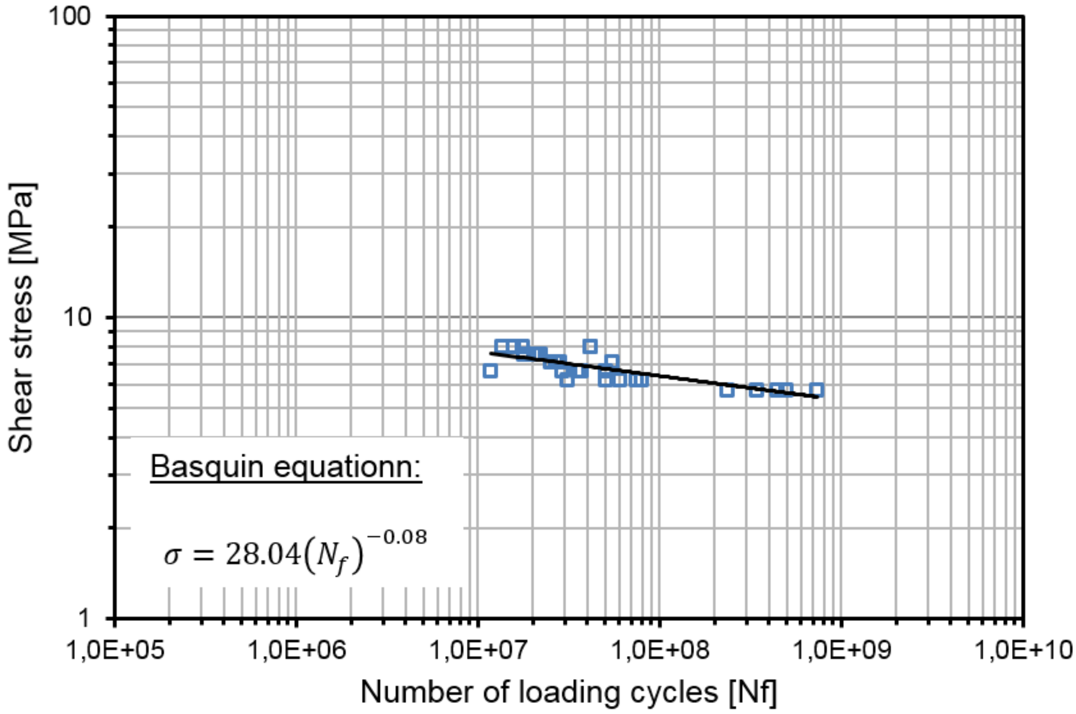

Figure 6.8. Basquin relationship of the S-N curve of the meniscus type solder joints in SMDs at RT.

The failure probability *H* of the SM-C was calculated for each shear load level by using the equation $\mathrm{H} = \frac{\mathrm{i}-0.3}{\mathrm{n}+0.4}$, where *n* is the total number of tested samples per level and *i* is the sample number arranged from low to high number of loaded cycles until failure. Figure 6.9 shows the failure probability of the device under shear loading in the range of 7.9 MPa down to 5.7 MPa. The two different slopes of the probability are related to the different fracture patterns in this region. The first three loading levels are representative for the mixed fracture pattern occurring at higher stress amplitudes and the remaining one for the pure solder fracture for samples with a higher lifetime

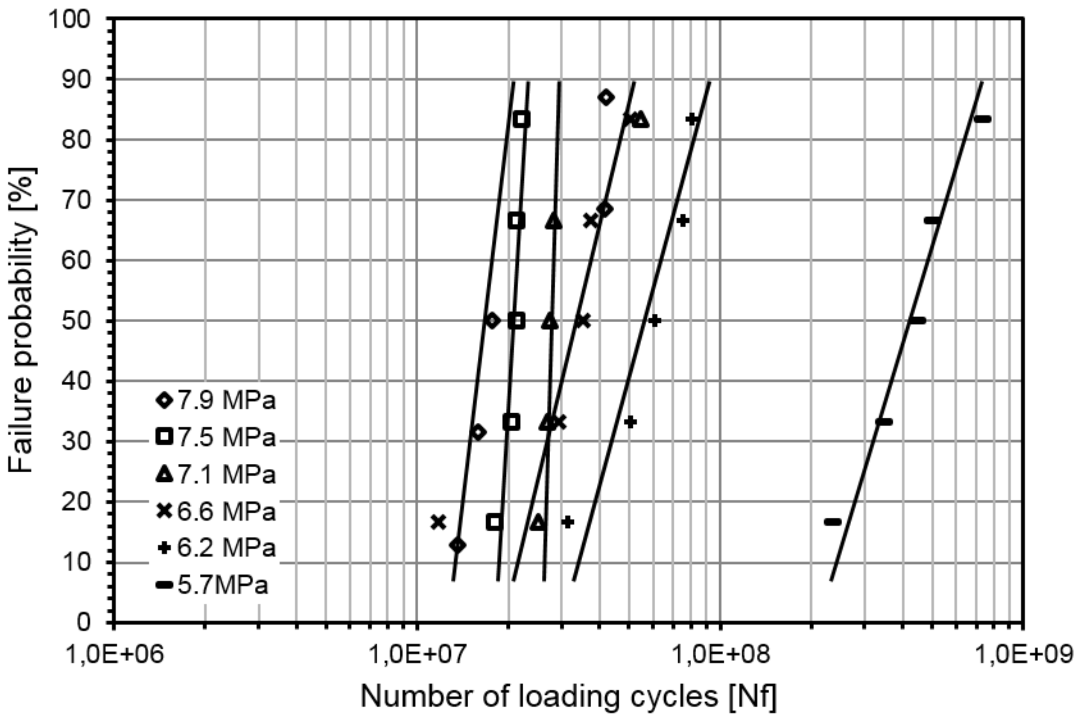

Figure 6.9. Failure probability of the SMD under shear loading in the range of 7.9 MPa down to 5.7 MPa.

Figure 6.10 shows a summary of all possible fracture surfaces observed at high stress amplitudes, ranging from fracture surfaces in the Cu, in the solder, in the ceramic or in the interface between these materials. Solder joints with the best fatigue performance failed mostly in the region near or at the interfacial IMC layer at the Cu pad side at shear stresses 7.0 MPa down to 5.3 MPa. Figure 6.11 shows the typical fracture surface in the mentioned loading range. Fracture surface analysis of the tested samples showed that the crack initiates and propagates in the Cu_6Sn_5 IMC layer resulting in brittle interfacial failure due to the high stress concentration in the interfacial region under the ceramic component. A transition from brittle to ductile failure is observed which occurs due to the presence of a tilting effect, which is increased with advanced crack growth (Figure 6.12). The resulting failure can be seen as a mixed failure mode between brittle IMC fracture and ductile solder fracture (Figure 6.13).

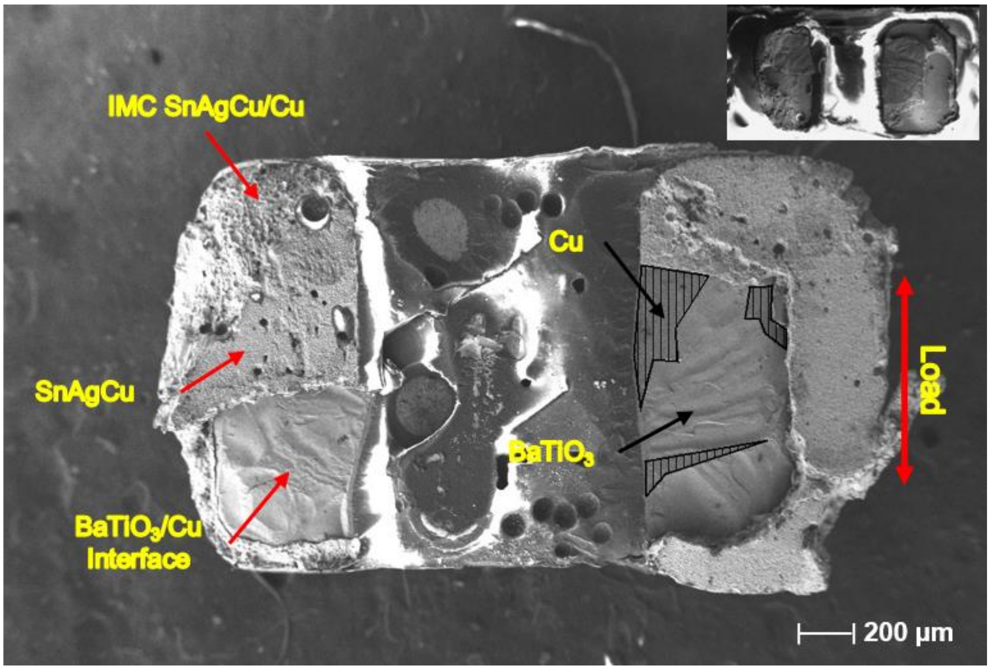

Figure 6.10. Possible fracture surfaces which may occur at high loading levels >7.0 MPa.

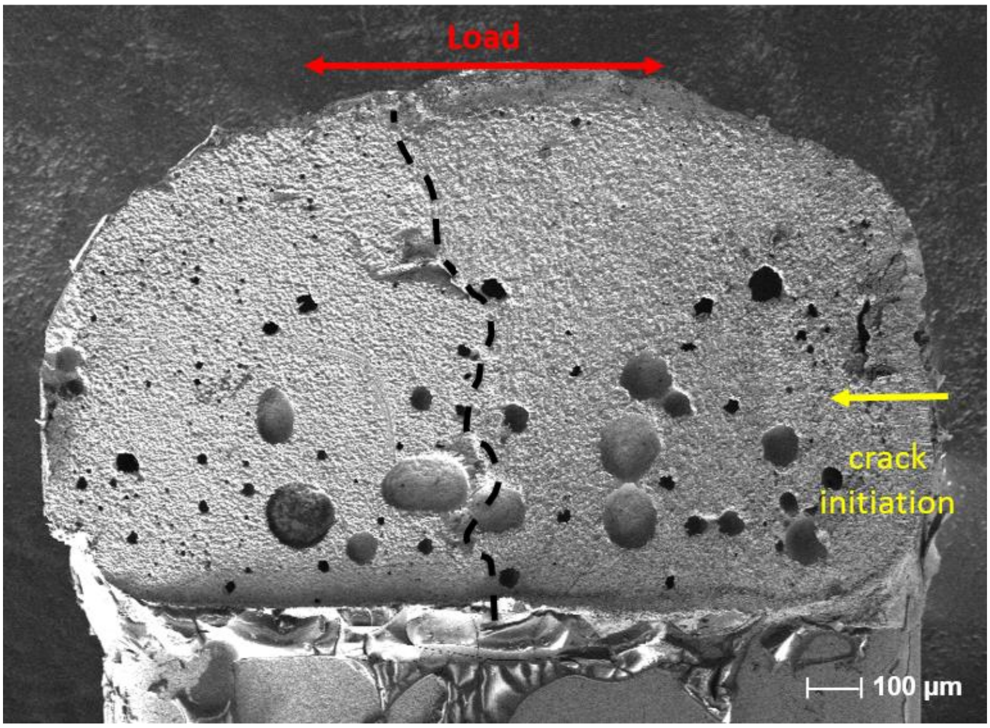

Figure 6.11. Fracture surface for shear loaded samples at high number of loading cycles.

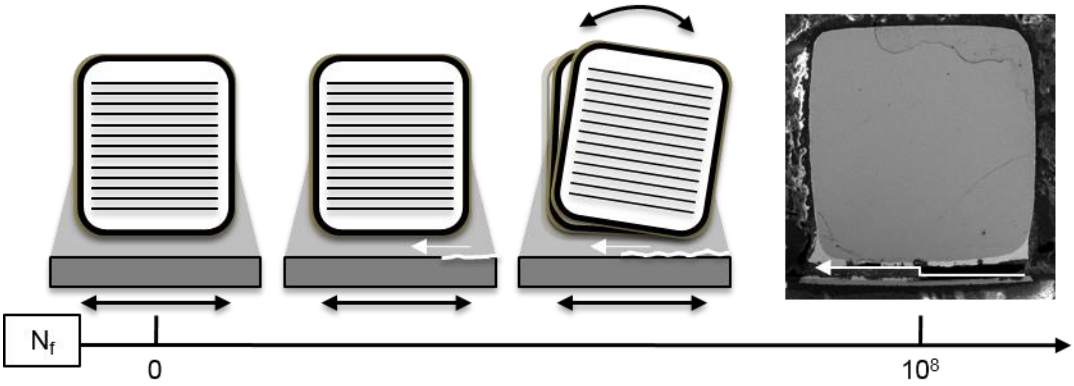

Figure 6.12. Schematically illustration of the occurring tilting effect.

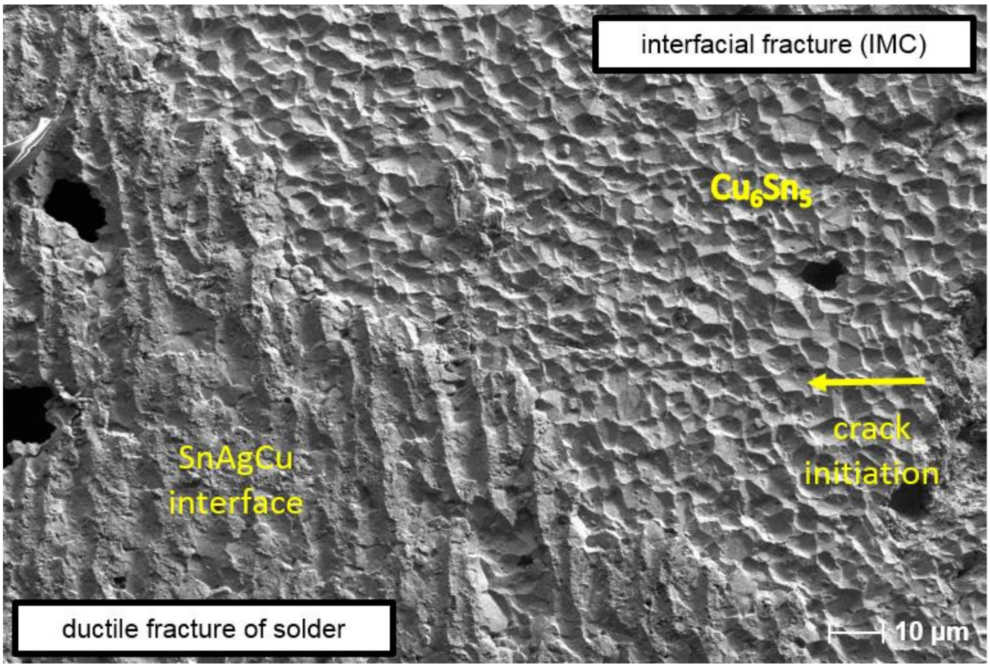

Figure 6.13. Fracture surface transition from brittle interfacial to ductile solder failure.

The final fracture path in the IMC is very similar to the fracture surface obtained from the tensile tests of Cu/SnAgCu/Cu solder joints. For solder joints with a gap size <100 μm the crack initiates and propagates in the Cu_6Sn_5 IMC layer resulting in brittle interfacial failure. Therefore a brittle failure mode was expected for the small sized solder gap under the ceramic body, where the crack initiation occurred.

In addition to the above described shear loading mode (x-orientation), for the next test series, the sample is rotated on the specimen holder by 90° (y-orientation). In this configuration the inert mass of the SMD (20 mg) was not sufficient to induce fatigue failure in the solder joint or in the ceramic. In the y-orientation the meniscus geometry of the solder joint provides a higher stability to shear stress than that obtained at the shear loading levels in x-orientation. For this reason the inert mass was increased by using 15 mg Cu pieces which were glued on the top of the ceramic component and finally led to failure of the component. Figure 6.14 shows the comparison of the two tested orientations.

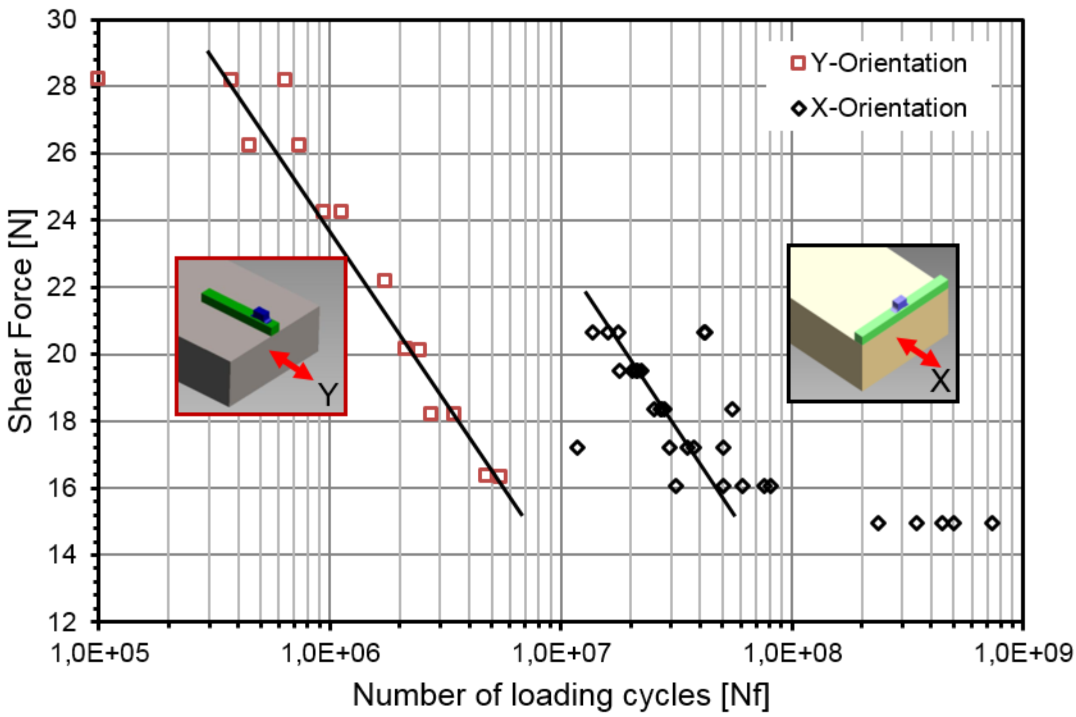

Figure 6.14. Lifetime curves of the SMDs with different shear loading directions at RT.

The curve is plotted as function of shear force and the number of loading cycles up to 10^9 cycles and shows an equal slope of the curve in the section for a low number of loading cycles. In the y-orientation the fracture occurs in the ceramic body with the crack initiation in the copper termination and propagates further into the ceramic body following a 45° path (Figure 6.15). Through the ceramic breakage this test series were not pursued because the goal of these experiments were evaluation of mechanical fatigue response of the solder joints.

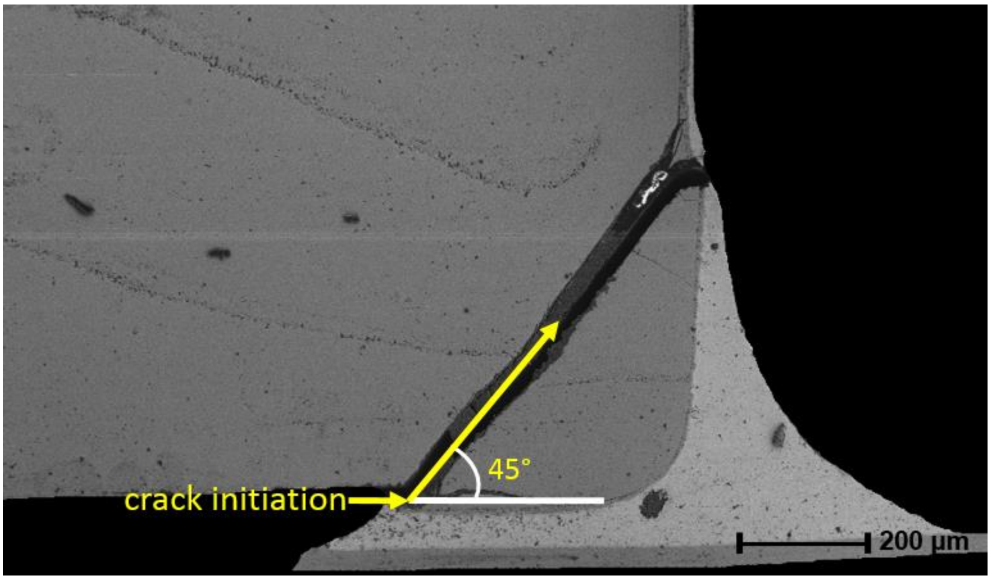

Figure 6.15. Fracture evolution observed in SMD tested in y-orientation.

6.3.3. Aging Effect on Fatigue Lifetime

The samples were subjected to various heat treatments (150°C up to 1000h) to reproduce the microstructural evolution of the solder joints under thermal loading conditions. Each aging condition represents a microstructure after a certain number of thermal cycles between -40°C and 125°C with holding times of 30 min for each maximum. This relationship is shown in Table 10.

Table 10. Microstructure equivalent by thermal cycles (-40°C and 125°C) and aging at 150°C.

Cycles (therm)	500	1000	1500	2000
Aging at 150°C	250h	500h	750h	1000h

Figure 6.16 shows a typical microstructure evolution of the solder in the middle section of the meniscus after four different aging times. The microstructure displays a typical ternary eutectic of Sn3.5Ag0.75Cu alloy consisting of a β-Sn matrix with Cu_6Sn_5 and Ag_3Sn particles. Long-time thermal exposure at 150°C resulted in a coarsening of the β-Sn phase and redistribution and coarsening of the Ag_3Sn and Cu_6Sn_5 particles. The size and number of IMC particles in the Sn matrix can also affect the mechanical response of the solder [76]. Thermal aging results in softening of solder material due to the microstructural changes and grain growth. Aging at 150°C also results in growth of Cu_6Sn_5 and Cu_3Sn at the interface, flattening of the IMC grains and increasing the

IMC thickness. Increased thermal exposure resulted in an increase of the Cu_6Sn_5 thickness from 2.5 µm to 5.2 µm (±0.4 µm) from the original state and after an aging time of 1000h respectively. A Cu_3Sn phase was formed during the aging and showed a thickness of 3.1 µm (±0.2 µm) after 1000h. The effects by aging are very similar to the results obtained in Chapter 2.3 for model solder joints.

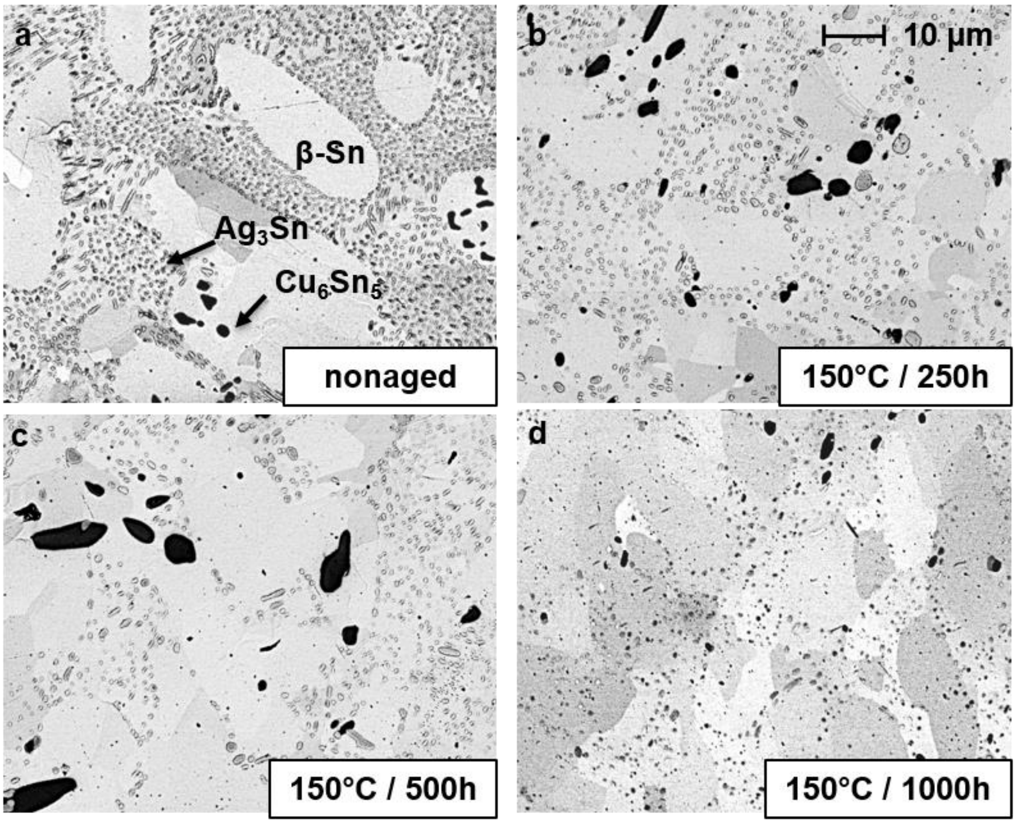

Figure 6.16. Microstructural changes of solder joint subjected to heat treatments at 150°C up to 1000h.

These thermally induced, thickness dependent microstructural changes have a high impact on the mechanical response of the meniscus type solder joint. The S-N curves presented in Figure 6.17 show that microstructural changes due to aging at 150°C have a significant influence on the lifetime of the SMD devices under shear loading at RT. Increasing the aging time resulted in a parallel downward shift of the S-N curve to shear stress values below 5 MPa at 10^9 cycles. The fatigue life curve of the non-aged devices covers the range of 10^7 up to 10^9 showing a rather steep drop from 7.9 to 5.8 MPa at about 10^8 cycles (a). Heat treatments results in a reduction of lifetime for shear loads from 7.9 to 4.8 MPa and a flattening of the whole curve (b-d). This trend resembles the one observed for the tensile response of model solder joints (Figure

2.15). Increasing the aging time resulted in a parallel downwards shift relative to the reference solder joints.

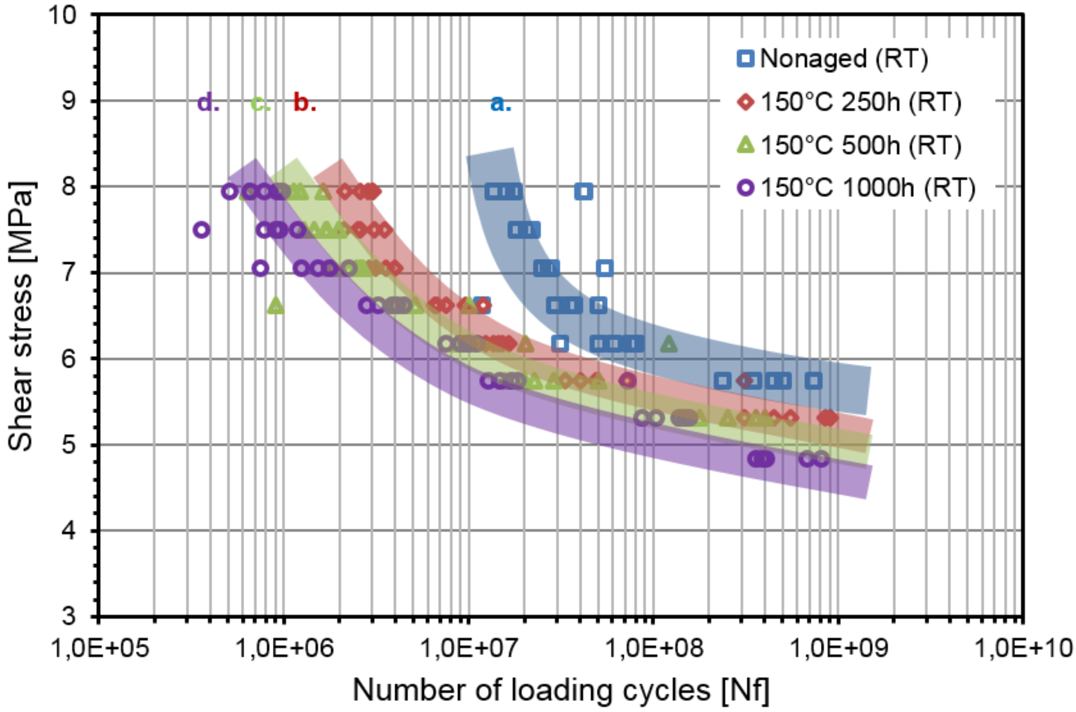

Figure 6.17. Lifetime of the meniscus type solder joints in SMDs for different heat treatments tested at RT.

Figure 6.18 shows the Basquin lifetime curves for the solder joints with different aging times. An overview of the obtained fatigue strength coefficient σ_f' and the fatigue strength exponent *b* are given in Table 11. The reduction of both parameters is representative for the thermal aging effect, which results in softening of solder material and grain growth. The fracture shear stress limit was reduced from 28.0 MPa down to 18.8 MPa. The 33% reduction of the shear stress is comparable to the observed average reduction of 30% of the UTS for thin solder model joints with increasing aging time up to 1000h. The fatigue strength coefficient was reduced from 0.08 to 0.06, which describes the ductility of the material.

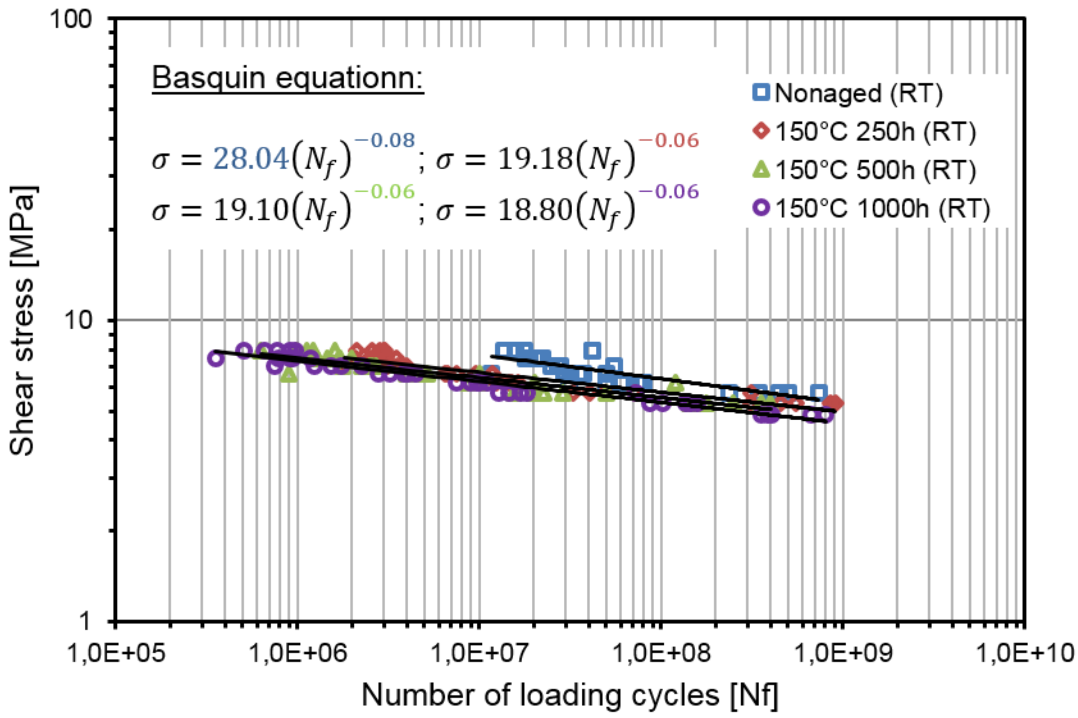

Figure 6.18. Basquin relationship of the S-N curve of the SMDs for different heat treatments tested at RT.

Table 11. Fatigue strength coefficient σ_f' and exponent b for different heat treatments.

	σ'_f [MPa]	b [-]
Nonaged	28.0	0.08
150°C, 250h	19.2	0.06
150°C, 500h	19.1	0.06
150°C, 1000h	18.8	0.06

Figure 6.19 shows the failure probability of the SM-Cs at a constant stress level of 7.1 MPa and demonstrates the effect of aging on the fatigue resistance of the samples. At this stress level aging at 150°C for 250h results in a considerable shift of failure probability curves to the lower N_f values. Further aging has a minor effect on the fatigue performance of the SMDs. Furthermore, the plots show a similar slope which would suggest a similar fracturing mechanism.

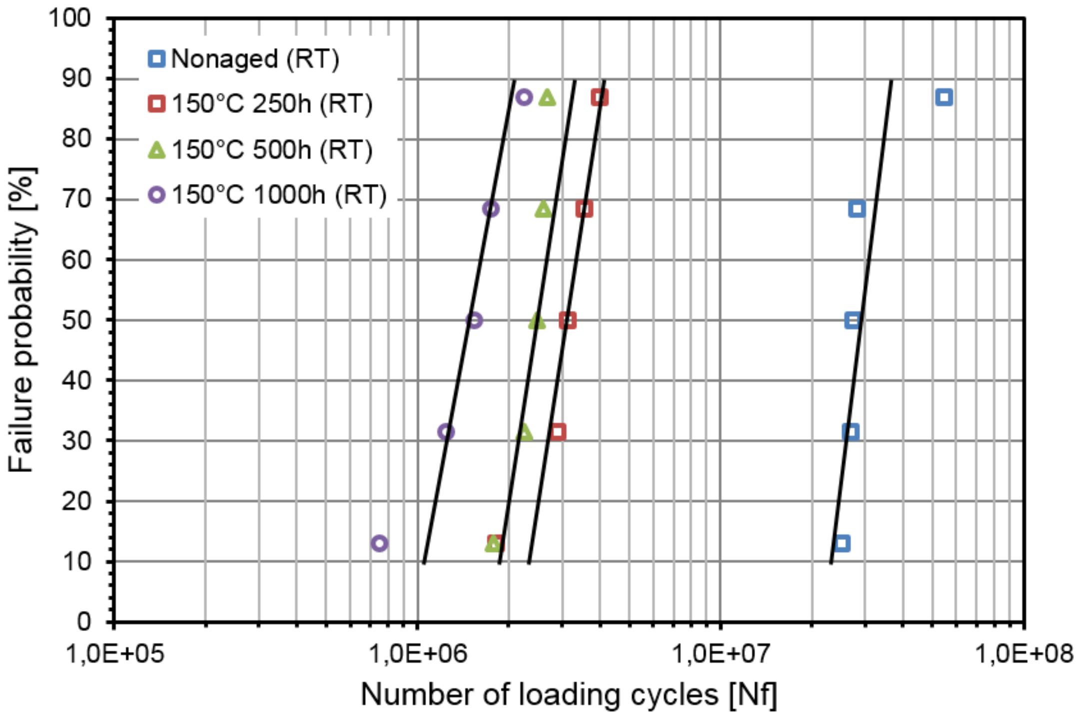

Figure 6.19. Failure probability of the SMD for different heat treatment along the shear stress 7.1 MPa.

Comparing the failure modes of the non-aged samples with aged ones, the factors dominating the failure mode in the meniscus are the microstructure of the bulk of the solder (Figure 6.16) and the thickness and morphology of the IMC layer. The fracture surface morphology of the samples aged up to 500h was similar to those observed in the non-aged solder joints, however with a different ratio of IMC/solder failure. For non-aged samples an area ratio from 1:3 brittle to ductile fracture surface was determined. Heat treatment at 150 °C, including the growth of the IMC, resulted in a shift of this relationship to about 3:1 for 500h aging time. Figure 6.20 shows exemplary fracture surface evolution at 5.6 MPa in which a transition from brittle to ductile failure is observed. With increased IMC layer thickness, the crack propagated a longer time in the IMC before deviating into the solder near the Cu_6Sn_5. The reduction of fatigue resistance in aged samples (up to 500h) is mainly related to the presence of a thick brittle IMC layer especially in the thin solder joint region below the capacitor which is more sensitive to mechanical loads. At high loading levels (7.5 MPa and 7.9 MPa) mixed failure modes are observed for aged samples similar to failures in nonaged samples at high impact loading.

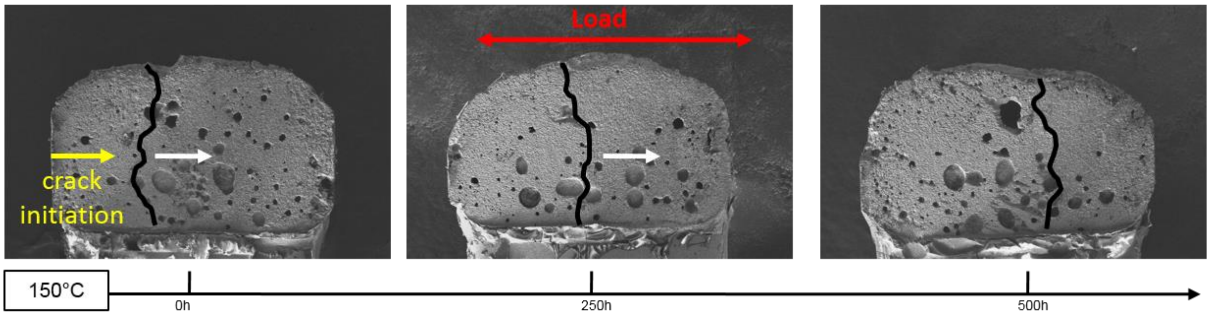

Figure 6.20. Fracture surface evolution at 5.6 MPa with observed transition from brittle to ductile failure.

The failure occurred mainly in the Cu_6Sn_5 layer and cracks leading to fracture are not identified in the Cu_3Sn layer. This effect is probably due to the higher internal stresses of Cu_6Sn_5 and the difference in the fracture toughness of the two phases. The fracture toughness of Cu_6Sn_5 and Cu_3Sn are reported to be 2.80 MPa $m^{1/2}$ and 5.72 MPa $m^{1/2}$, respectively [52]. A clear change in the failure mechanism was observed for samples aged for 1000h. The fatigue crack was initiated at the same location below the device but propagated already into the soft solder in the thin solder gap below the pad and further into the meniscus following an almost 45° path (Figure 6.21).

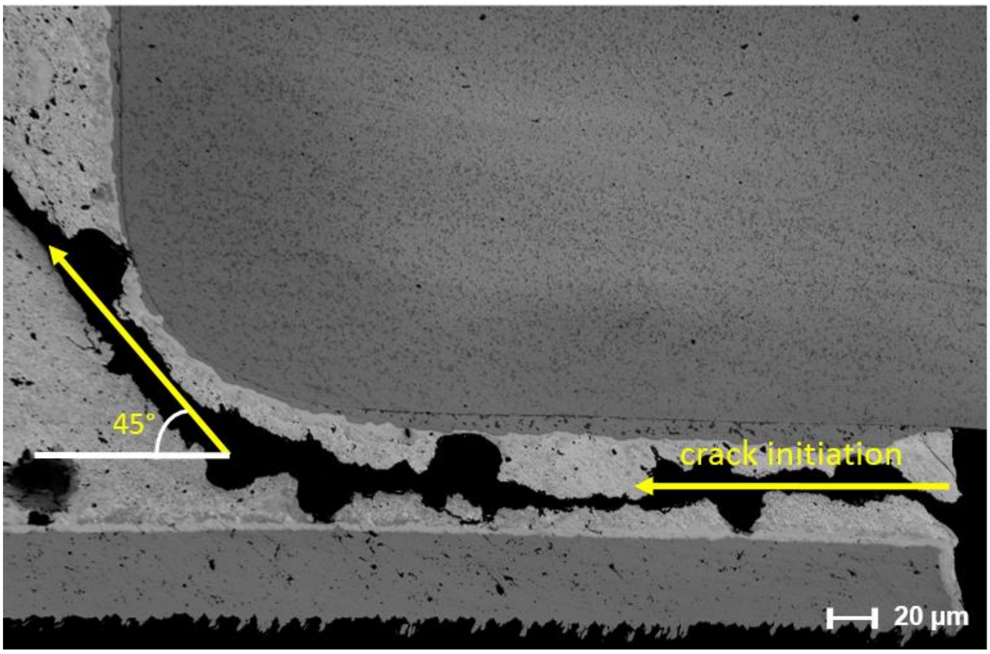

Figure 6.21. Fracture evolution observed in SMD aged samples at 150°C/1000h.

6.3.4. Influence of Testing Temperature on the Lifetime

Fatigue tests were conducted at ambient and elevated temperatures. Isothermal testing was performed at 80°C by using a hot air blower and the temperature was controlled during testing with an accuracy of ±1 K. The test device was attached to the holder and was preheated for about 1 hour to assure the thermal equilibrium during the testing. Figure 6.22 shows the isothermal S–N curves for the meniscus type Sn3.5Ag0.75Cu solder joints in bi-polar SMD packages in non-aged conditions.

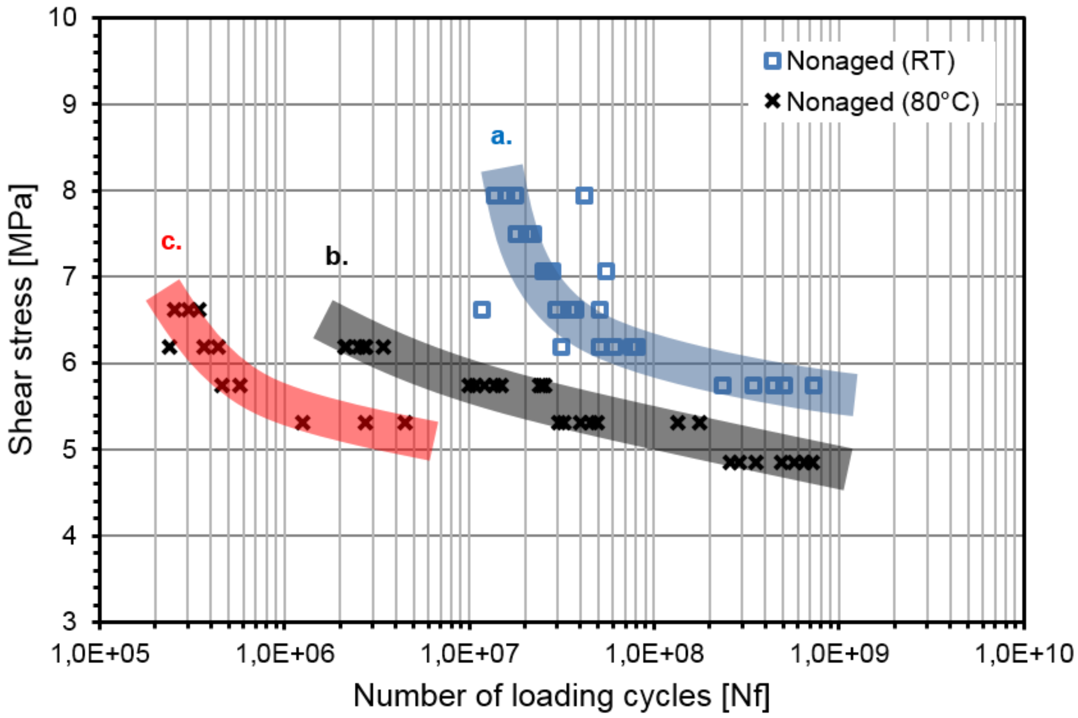

Figure 6.22. Lifetime of non-aged SMDs tested at RT (a) and 80 °C (b). (c) represents the frequent occurrence of pad cratering at 80°C.

The fatigue life curve of the non-aged devices covers the range of 10^7 up to 10^9 showing a rather steep drop from 7.9 to 5.8 MPa at about 10^8 cycles (a). Isothermal testing at 80°C results in a reduction of maximum of shear stress to 6.1 MPa and a flatter trend of curve (b). Due to the very short testing time during the ultrasonic fatigue testing at 20 kHz (few minutes up to max 15 h) major microstructural changes were not expected. The drop of the curve is mainly attributed to the creep effect at the homologous testing temperature of 0.7. A further feature of fatigue testing at 80°C was the frequent occurrence of pad cratering in the range of 10^5 up to 10^7 cycles as presented in curve (c). This effect was observed mostly for samples tested at higher stresses and can be related to the presence of weak interfaces between the Cu-pads and the PCB in a few samples. This failure type resembles the failure mode observed during the impact loading.

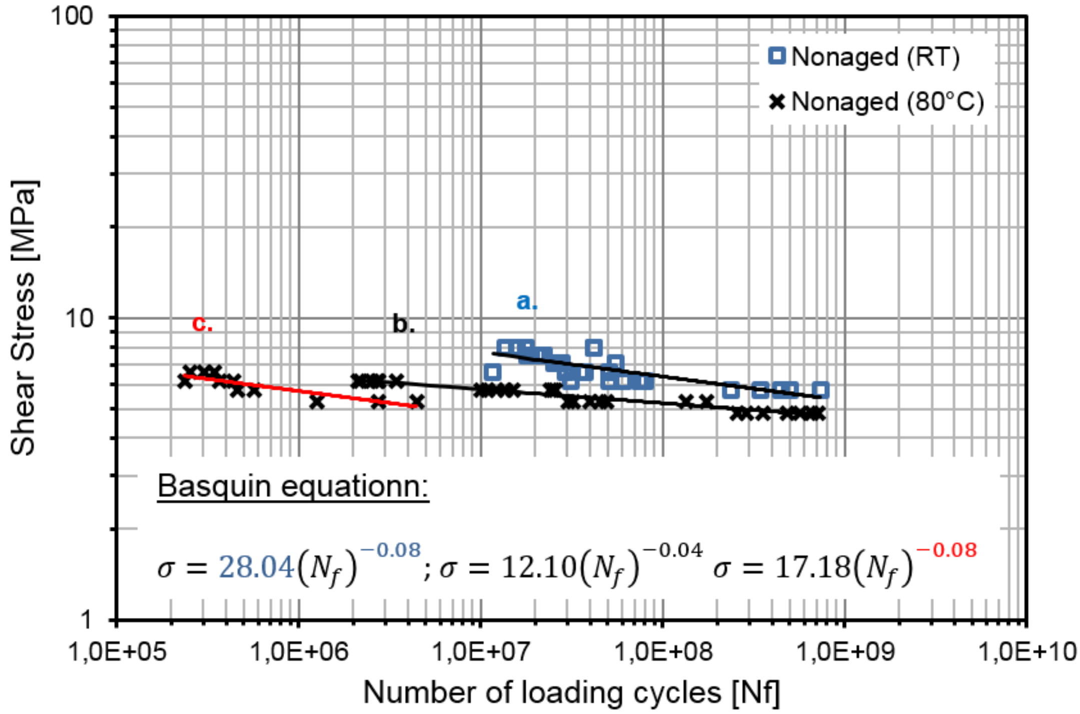

Figure 6.23. Basquin relationship of the S-N curve of the SMDs isothermal tested at RT and 80°C.

Figure 6.23 shows the Basquin fits for the devices isothermal tested at RT and 80°C. An overview of the observed fatigue strength coefficient σ_f' and the fatigue strength exponent *b* are given in Table 12. A plausible 57% reduction of the shear stress limit from 28.04 MPa to 12.10 MPa is given by the fits due to testing at 80°C. The same temperature effect was observed for the UTS limit of SnAgCu model joints. The fatigue strength coefficient was reduced from 0.08 to 0.04 by testing at 80°C, which can be interpreted as a change in the cyclic hardening effect.

Table 12. Fatigue strength coefficient σ_f' and exponent b for isothermal test conditions.

	σ_f' [MPa]	b [-]
RT	28.04	0.08
80°C	12.10	0.04

Fracture surface analysis showed a clear change of the failure mode and mechanism with increasing the testing temperature (RT and 80°C). The weak site of the joint was identified to be the thin 20 µm solder gap between the Cu pad and the capacitor in both cases. The crack always initiated at this location and propagated toward the meniscus. The further crack path, the direction of the crack growth in the meniscus and the resulting fracture mode and surface topography was highly dependent on the aging conditions as well as test temperature as explained in the following. Non-aged solder joints with the best fatigue performance failed mostly in the region near or at the interfacial IMC layer at the Cu pad side (Figure 6.24a). The crack was initiated in the 2.5 µm thick IMC layer under the component (Cu pad side) and propagated inwards. Reduction of the solder joint area beneath the capacitor resulted in an additional cyclic tilting of the device during the loading. From this point due to the mixed shearing and bending modes, the crack deviated from the Cu_6Sn_5 and propagated into the solder above the IMC until fracture of the joint. The ductile fracture in the solder joint can mainly be considered as the final rupture.

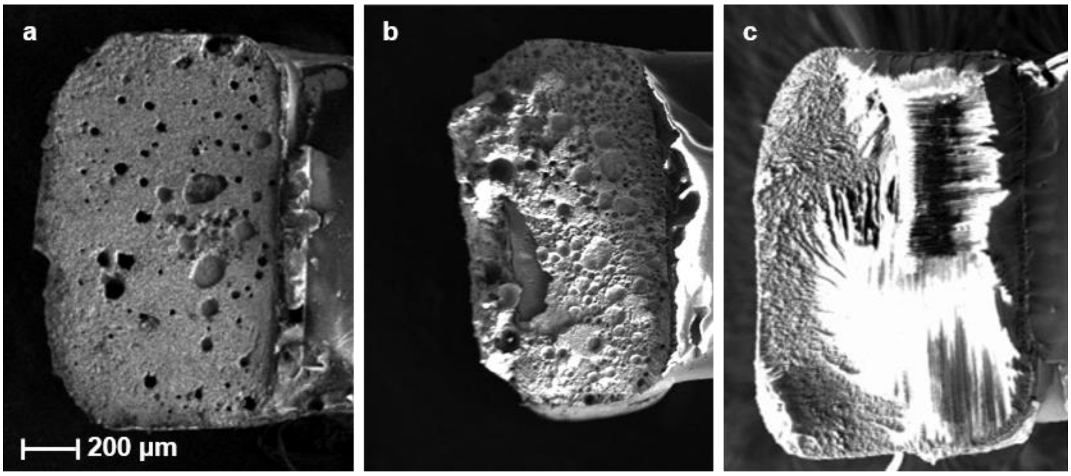

Figure 6.24. (a–c) Typical fracture surface of the tested SMD non-aged sample (IMC/solder, solder, pad fracture).

A clear change of the fatigue failure mode was observed in non-aged samples due to testing at 80°C (Figure 6.24b). Testing at elevated temperature resulted in a transition of the crack path from the brittle IMC layer into the solder resulting in a fatigue failure in a ductile manner. This interesting result shows clearly that at high homologous temperatures (T_h>0.7), even at such high strain rate loading conditions (>10^2), the creep effect in the solder is the dominating factor in lifetime of SAC solder joints. The higher accumulated plastic strain in the soft solder results in the reduced lifetime of the SMD devices. Besides solder joint fatigue, pad cratering was also observed as a further failure mode of the SMD at 80°C. This can be related to the reduced adhesion strength of the Cu pad to the PCB at elevated temperatures (Figure 6.24c). Figure 6.25a and b show a comparison of crack path and failure modes in non-aged samples tested at RT and 80°C.

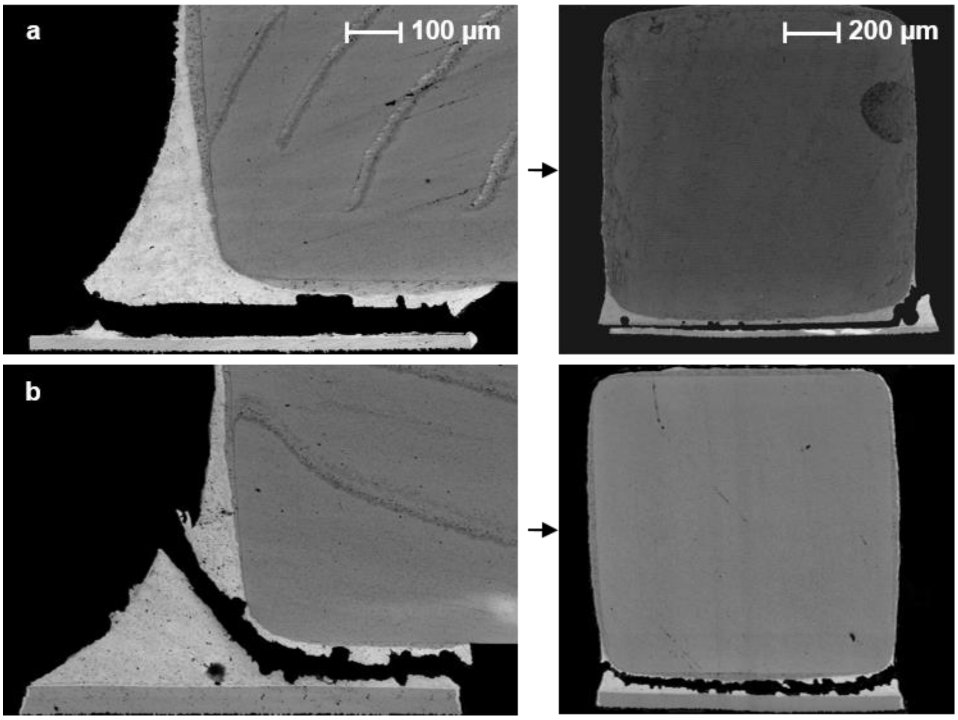

Figure 6.25. Cross section (a and b) of the non-aged SMDs tested at RT and 80°C.

In case of non-aged sample the crack is initiated at the IMC layer under the capacitor and propagates parallel to the Cu pad until final fracture in the solder layer above the IMC (Figure 6.25a). During the isothermal loading at 80°C the crack grows in the thin solder layer below the pad and is deflected in an approximately 45° angle into the meniscus. It is remarkable that this fracture behavior which is induced by isothermal mechanical cycling is closely similar to those observed in solder joints in SMD devices subjected to thermal cycling [27].

A comparison of the lifetime curve of the samples aged at 150°C/1000h with that of the isothermally tested non-aged devices is given in Figure 6.26. The curves run closely together and almost overlap in the higher loading cycles in the range of 10^7 up to 10^9 cycles. In both cases, the fatigue cracks are initiated below the device and propagated into the soft solder in the thin solder gap below the pad and further into the meniscus following an almost 45° path (Figure 6.25b).

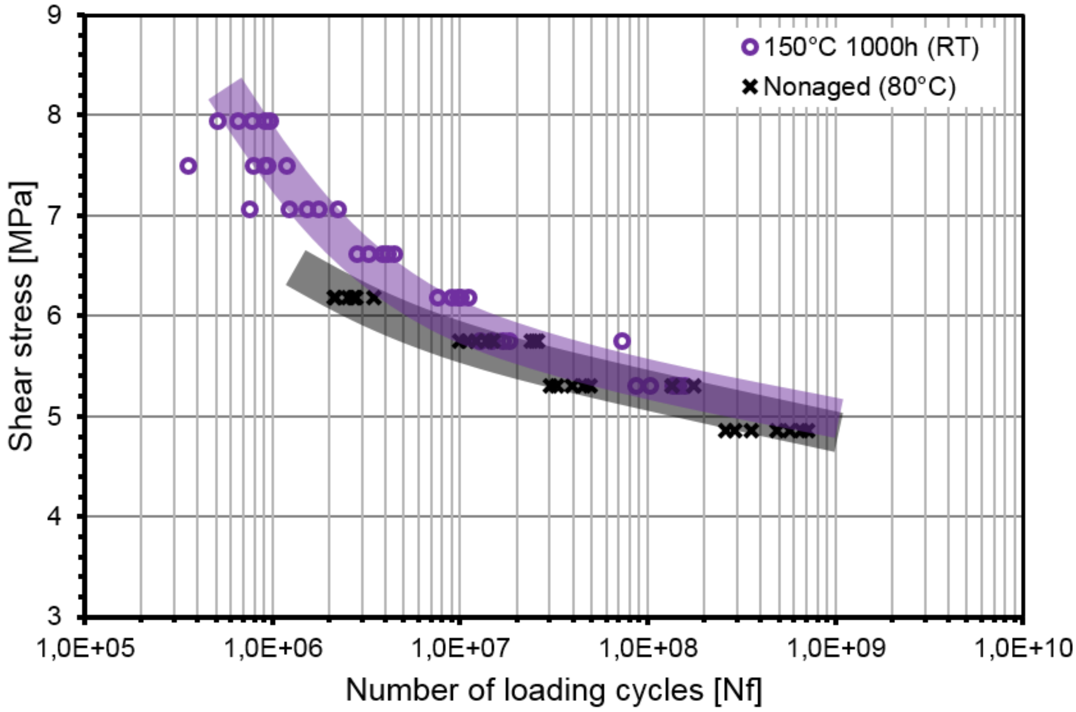

Figure 6.26. Comparison of the S–N curve of the SMDs aged at 150°C/1000h with the isothermally tested non-aged devices.

A comparison with tensile tests showed comparable results in the case of the overlapping sections of samples aged with that of the isothermally tested non-aged samples depending on the Cu/SnAgCu/Cu gap thickness. Decreasing the solder gap size resulted in a steady increase of ultimate tensile strength for all samples as shown in Figure 6.27. This behavior is known as geometrical constraint effect in thin solder joints [6]. Aging resulted in a downward shift of the ultimate tensile strength, which is related to softening of solder material concurrent with proportional increase in the brittle

IMC layer. Furthermore possible voids and cracks may also result in a reduced ductility and early fracture of the joints. As expected, testing at 80°C also results in a decrease of the tensile strength due to creep effects. The higher reduction of UTS for the thicker solder joints tested at 80°C is related to the higher contribution of the creep in the ductile solder material with increasing the solder volume.

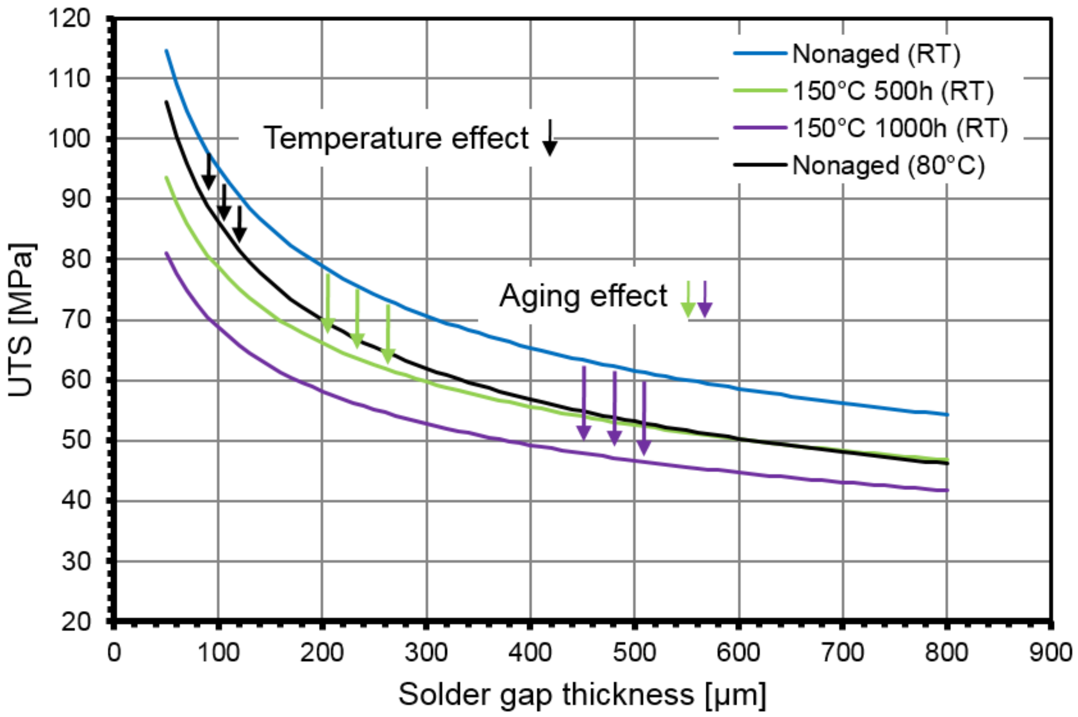

Figure 6.27. Dependence of ultimate tensile strength on solder joint thickness: comparison of aging and test temperature.

6. Summary

Isothermal high frequency mechanical shear fatigue response of Sn3.5Ag0.75Cu meniscus type solder joints in bi-polar capacitors has been investigated. The influence of microstructure on their lifetime was studied by aging the SMD at 150°C up to 1000h. Fatigue life and the related failure modes were highly dependent on the testing temperature, microstructure of the solder joints and the proportion of interfacial IMC layer. In automotive applications, the reliability of the devices is assessed by thermal cycling procedures. In this case, the failure mode is fatigue failure in the solder with a defined crack path in the solder joint. In this study it could be shown that isothermal accelerated mechanical fatigue testing of the non-aged devices at 80°C results in the same failure mode in the solder joint as observed due to traditional thermal cyclic procedures. The same case was observed for solder joints subjected to long term aging at 150°C. These results are definitely different from failures usually observed in solder joints subjected to high strain rate repetitive mechanical loads. A further interesting finding is the overlapping of the lifetime curves of the non-aged isothermally tested samples with those aged at 150°C/1000h in the range of 10^7–10^9 cycles. More than once a correspondence between the tensile tests of model solder joints and fatigue behavior could be obtained. In particular, the knowledge of strengths and weaknesses of miniaturized model joints by the existence of the brittle IMC was used to interpret fatigue properties of the SMD solder joint under cyclic loads.

The present chapter contributes to a better understanding of the fatigue response of lead-free solder joints to high strain rate loading conditions by considering the microstructural and thermal effects. The findings can be considered as a further step for development of an alternative accelerated testing procedure based on mechanical fatigue for replacement of traditional thermal cycling procedures and rapid evaluation of solder joints in automotive applications.

CHAPTER 7
Highlights

7.1. Tensile Properties Measurement and Microstructure Analysis for SnAgCu Lead-Free Solders

SnAgCu (SAC) is one of the mostly accepted solders among the lead-free solder compositions in microelectronic applications. The knowledge of the complex thermo-mechanical response of miniaturized solder joints is of high significance for the prediction of the reliability of the devices. Thermal and mechanical behavior of the solder joints is primarily affected by the dimensional constraint and microstructural factors. In Chapter 2 the influence of microstructure and geometrical constraint on the mechanical response of miniaturized lead-free solder joints is investigated.

The relationship between the solder gap size and thickness of the intermetallic compound (IMC) on tensile behavior of Cu/Sn3.5Ag0.75Cu/Cu solder joint models with different ratios of IMC to the gap size is studied by tensile experiments using a laser speckle system to measure the strain. The variation of the IMC size was realized by different reflow times or heat treatments. An increased ratio of IMC thickness to the gap size results in a transition of the fracture mode from ductile to brittle and affects the strength of the solder joint. An increase in tensile strength and a decrease in fracture strain with decreasing the gap size were observed with a stronger effect for thinner joints due to their finer initial microstructure and the higher proportional IMC/thickness ratio. Increasing the solder gap size results in a shift of the crack path from the interfacial region to the bulk of the solder. Aging at 150°C for a period of 500h up to 1000h resulted in a reduction of the stress and an increase of the elongation of the solder joints with a stronger effect of the latter for thicker joints. The distribution of strain on the surface of solder joint during the tensile loading was investigated by 3D digital image correlation technique, which showed strain concentration in the interfacial region of the solder to substrate for all gap sizes. The results provide a further explanation for interfacial or near interface failure mode in the solder joints. With the obtained data on the strain distribution and microstructure evolution in solder joints with gap sizes ≤ 800 μm, a constitutive model for Finite Element Model simulations can be created. The obtained data can also be used to classify solder joints in electronic components under mechanical loads. It is known that solder joints in electronic applications must survive a combination of mechanical and thermal stress under service. For reliability concepts of solder joints in real devices, the knowledge of their strengths and weaknesses is essential.

7.2. Creep Behavior of SnAgCu Lead-Free Solder System

Creep properties are important to understand the time and temperature dependent mechanical deformation of materials, especially solder joints, which are in use at high homologous temperatures. This material property is often responsible for failures in solder joints under static or dynamic loads and can be displayed via a stress strain time relationship. To understand the time, the temperature and the microstructure dependent material properties of miniaturized solder joints stress relaxation experiments were performed (Chapter 3). Stress relaxation is defined as a decrease in stress with time under a constant deformation or strain.

Stress relaxation tests are performed for eutectic Cu/Sn3.5Ag0.75Cu/Cu model solder joints with a gap thickness of 100 µm up to 900 µm. A higher stress drop for thick solder gaps in comparison to thin gaps is obtained due to the constraint effect and the higher proportion of high-strength but brittle intermetallic compound (IMC) phase in thin solder joints. The stress exponents and activation energies are determined by employing a simple creep power law equation. The stress exponent is temperature dependent and decreases for thick solder gaps (>800 µm) from n=14.4 at room temperature down to n=5.3 at 125°C. For thin solder gaps <200 µm, very high stress exponents are calculated, which is due to the amount of brittle IMC resulting in highly reduced stress relaxation. The activation energy is dependent on the solder gap thickness and is 55.4 kJ/mol for a solder gap >800 µm and 72.9 kJ/mol for a thin solder joint <150 µm. Therefore the size effect on creep behavior as well as the dependence on the content of brittle IMC phase is significant for miniaturized solder joints. The miniaturization effect becomes reasonable where microstructural changes occur. Therefore the effect of IMC growth and microstrcutural changes on the creep behavior is much stronger at miniaturized solder joints than in bulk materials. The measurements on aged solder joint samples showed a decreasing trend of thermal expansion of the solder joints with increasing the aging time up to 1000h at 150°C.

The obtained (size, temperature and time dependent) creep behavior of the studied solder joints can be included in parametric FE models to describe the strain and stress evolution in electronic devices after thermo or mechanical cycling loads. The experiments can be explained by a new constitutive model considering a strain dependent threshold value for creep. Alternatively, one of the existing creep models, like the generalized Garofalo model, also leads to a satisfactory description of the stress relaxation experiments. Stress relaxation data are therefore a key to future FEM of lead-free solders. Estimation of stress relaxation effects of miniaturized solder systems is one of the key factors for optimization of the design of surface mounted devices.

7.3. Coefficient of Thermal Expansion of Miniaturized SnAgCu Solder Joints

The thermal expansion coefficient is a basic material characteristic, which virtually in all areas of engineering affects the functionality and the durability of the system components. Microelectronic devices are composed of a variety of materials with different physical and mechanical properties. Mismatch between the coefficients of thermal expansion of the constituent materials is the primary source of stress or strain in these complex structures. To understand the size and the microstructure dependent thermal properties of miniaturized solder joints thermal strain measurements were performed in Chapter 4.

The focus of the study was the change of the overall coefficient of thermal expansion of Cu/Sn3.5Ag0.75Cu/Cu solder joints with different ratios of IMC. A laser interferometric system (LIS) is applied to measure the local thermal strain of miniaturized Sn3.5Ag0.75Cu joints with a thickness of 80 µm and 120 µm. The LIS system allows determination of local deformation of thermal elongation between two Vickers microhardness indentations with a resolution of about 2 nm. An overall CTE of 26.1 ± 0.2 ppm/°C is observed for miniaturized solder gaps. Measurements of the aged solder gaps showed a decreasing trend of thermal expansion with increasing the aging time up to 1000h at 150°C due to proportional increase of the IMC layers. The measured thermal strain values show that the overall CTE of the solder joints is highly dependent on their microstructural evolution. The obtained result confirms the importance of knowledge of thermal properties of the solder joints in their actual dimensions and geometries. Knowledge of the changes in the CTE value due to the geometrical and aging effects allows to establish improved lifetime prediction models for solder joints in real devices. By using these experimentally determined CTE values, reliable thermo-mechanical simulations can be conducted and the distribution of thermal strain in the complex multilayer structures can be calculated. Such simulations have been used as part of a COMET project (A7.11) to study the relationship between thermal and mechanical cycles.

7.4. Low and High Cycle Fatigue of Surface Mounted Device Solder Connection

Surface mounted devices (SMDs) in microelectronics are subjected to electrical, thermal and mechanical loads during the service. Especially in automotive applications vibrational loading in combination with temperature effects may lead to failure of the devices due to mechanical fatigue. Thus the reliability of the devices is highly influenced by the mechanical and thermal response of the used SnAgCu solder joints. A new approach for studying the thermo-mechanical response of solder joints subjected to cyclic loading is the application of mechanical isothermal low or high frequency fatigue testing. A combination of thermal and mechanical loads allows realizing realistic service conditions in an accelerated manner. The aim of Chapter 5 and 6 is the investigation of fatigue response and failure modes of solder joints in SMD capacitors subjected to high and low frequency isothermal fatigue.

A low cycle fatigue life testing method for selected solder joints was investigated with an attempt to establish a relationship between mechanical and thermal lifetimes. The suitable boundary conditions for the LCF setup were determined by finite element simulations in which the mechanical displacement amplitude required for inducing the equivalent accumulated thermal strain in the solder joint was calculated (performed by project partner). Due to some complications with the developed SMD design, the LCF setup could only be checked on the basis of tin-lead BGA solder joints. These findings can be considered as a further step for development of alternative accelerated testing procedure based on thermo-mechanical fatigue for replacement of traditional thermal cycling procedures and rapid evaluation of solder joints in automotive applications. Establishment of reliability assessment methods for solder joints based on mechanical fatigue testing as a replacement for thermal cycling procedures requires further intensive research. Further necessary steps are investigations on topics such as strain rate dependency, determination of the acceleration factor, recrystallisation effects, variation in the load axis or superposition of thermal and mechanical cycles to establish an adequate method to replace thermal cycles.

Isothermal lifetime curves of solder joints in SMD devices subjected to high strain vibrational loading were obtained by using an ultrasonic fatigue testing set-up at 20 kHz. Mechanical reliability and the failure modes of solder joints in the SMD capacitors were found to be highly dependent on the microstructure of the solder and the intermetallic compound layer and the testing temperature. In automotive applications, the reliability of the devices is assessed by thermal cycling procedures. The study of Chapter 5 shows that isothermal accelerated mechanical fatigue testing of the nonaged devices at 80°C results in the same failure mode in the solder joint as observed due to traditional thermal cyclic procedures. The same case was observed for solder joints subjected to long term aging at 150°C. These results are definitely different from failures usually observed in solder joints subjected to high strain rate repetitive mechanical loads. A further interesting finding is the overlapping of the lifetime curves of the non-aged isothermally tested samples with those aged at 150°C/1000h in the range of 10^7 to 10^9 cycles. The study contributes to a better understanding of the fatigue response of lead-free solder joints to high strain rate loading conditions by considering the microstructural and thermal effects.

BIBLOGRAPHY

[1] N.-C. Lee, “Getting Ready for Lead-free Solders*,” *Solder. Surf. Mt. Technol.*, vol. 9, no. 2, pp. 65–69, 1997.

[2] J. Lau, R. Horsley, I. Menis, and M. Park, “HDPUG ’ s Design for Lead-Free Solder Joint Reliability of High-Density Packages,” in *IPC SMEMA Council APEX®*, 2003.

[3] Y. T. Chin, P. K. Lam, H. K. Yow, and T. Y. Tou, “Investigation of mechanical shock testing of lead-free SAC solder joints in fine pitch BGA package,” *Microelectron. Reliab.*, vol. 48, no. 7, pp. 1079–1086, Jul. 2008.

[4] K. Moon and W. J. Boettinger, “Accurately Determining Eutectic Compositions : The S n -Ag-Cu Ternary Eutectic,” *JOM*, vol. 56, no. 4, pp. 22–27, 2004.

[5] G. E. Dieter, “Chapter 8-1, Engineering Stress-Strain Curve,” in *Mechanical Metallurgy*, 1986, pp. 275–283.

[6] G. Khatibi, H. Ipser, M. Lederer, and B. Weiss, “Influence of miniaturization on mechanical reliability of lead-free solder interconnects,” in *Lead-free solders: Materials reliability for electronics*, 2012, pp. 445–485.

[7] K. . Kim, S. . Huh, and K. Suganuma, “Effects of cooling speed on microstructure and tensile properties of Sn–Ag–Cu alloys,” *Mater. Sci. Eng. A*, vol. 333, no. 1–2, pp. 106–114, Aug. 2002.

[8] W. H. Bang, K. H. Oh, J. P. Jung, J. W. Morris, and F. Hua, “The correlation between stress relaxation and steady-state creep of eutectic Sn-Pb,” *J. Electron. Mater.*, vol. 34, no. 10, pp. 1287–1300, Oct. 2005.

[9] S. Wiese, M. Roellig, M. Mueller, S. Bennemann, M. Petzold, and K.-J. Wolter, “The Size Effect on the Creep Properties of SnAgCu-Solder Alloys,” *2007 Proc. 57th Electron. Components Technol. Conf.*, pp. 548–557, 2007.

[10] S. Wiese and K.-J. Wolter, “Microstructure and creep behaviour of eutectic SnAg and SnAgCu solders,” *Microelectron. Reliab.*, vol. 44, no. 12, pp. 1923–1931, Dec. 2004.

[11] Y. J. C. M. L. Fuqian, “Deformation behavior of tin and some tin alloys,” *J. Mater. Sci. Mater. Electron.*, vol. 18, pp. 191–210, 2007.

[12] E. Arzt, “Size effects in materials due to microstructural and dimensional constraints: a comparative review,” *Acta Mater.*, vol. 46, no. 16, pp. 5611–5626, Oct. 1998.

[13] A. Schubert, R. Dudek, and E. Auerswald, “Fatigue life models for SnAgCu and SnPb solder joints evaluated by experiments and simulation,” *53RD Electron.*, pp. 603–610, 2003.

[14] Y. Qi, H. R. Ghorbani, and J. K. Spelt, “Thermal Fatigue of SnPb and SAC Resistor Joints: Analysis of Stress-Strain as a Function of Cycle Parameters,” *IEEE Trans. Adv. Packag.*, vol. 29, no. 4, pp. 690–700, Nov. 2006.

[15] Y. He, “Heat capacity, thermal conductivity, and thermal expansion of barium titanate-based ceramics,” *Thermochim. Acta*, vol. 419, no. 1–2, pp. 135–141, Sep. 2004.

[16] J. Suhling, R. Johnson, and J. White, “Solder joint reliability of surface mount chip resistors/capacitors on insulated metal substrates,” *Electronic*, 1994.

[17] H. Chen, C. Wang, and M. Li, “Numerical and experimental analysis of the Sn3.5Ag0.75Cu solder joint reliability under thermal cycling,” *Microelectron. Reliab.*, vol. 46, no. 8, pp. 1348–1356, Aug. 2006.

[18] C. Andersson and D. Andersson, “Effect of different temperature cycle profiles on the crack propagation and microstructural evolution of lead free solder joints of different electronic components,” *5th. Int. Conf. Therm. Mech. Simul. Exp. Micro-electronics Micro-Systems, EuroSimE2004*, 2004.

[19] N. Islam, J. Suhling, P. Lall, T. Shete, H. Gale, R. Johnson, M. Bozack, P. Seto, T. Gupta, and J. Thompson, “Thermal Cycling Reliability of Chip Resistor Lead Free Solder Joints,” in *Electronics*, 2003.

[20] G. Grossmann, G. Nicoletti, and U. Solbr, “Results of Comparative Reliability Tests on Lead Free Solder Alloys,” *Electron. Components Technol. Conf.*, pp. 1232–1237, 2002.

[21] M. N. Collins, J. Punch, R. Coyle, M. Reid, R. Popowich, P. Read, and D. Fleming, “Thermal Fatigue and Failure Analysis of SnAgCu Solder Alloys With Minor Pb Additions,” *IEEE Trans. Components, Packag. Manuf. Technol.*, vol. 1, no. 10, pp. 1594–1600, 2011.

[22] P. Limaye, K. Lambrinou, and B. Vandevelde, “Crack growth analysis of lead free passive component assemblies,” *Conf. Proc.*, vol. 1, pp. 774–782, 2006.

[23] W. . Lee, L. . Nguyen, and G. . Selvaduray, “Solder joint fatigue models: review and applicability to chip scale packages,” *Microelectron. Reliab.*, vol. 40, pp. 231–244, 2000.

[24] S. W. Shin and J. I. N. Yu, “Creep Deformation of Sn-3 . 5Ag-xCu and Sn-3 . 5Ag-xBi Solder Joints,” *J. Electron. Mater.*, vol. 34, no. 2, pp. 188–195, 2005.

[25] R. S. Sidhu, X. Deng, and N. Chawla, “Microstructure Characterization and Creep Behavior of Pb-Free Sn-Rich Solder Alloys: Part II. Creep Behavior of

Bulk Solder and Solder/Copper Joints,” *Metall. Mater. Trans. A*, vol. 39, no. 2, pp. 349–362, Dec. 2007.

[26] A. Grusd, “Lead free solders in electronics,” *Proc. Surf. Mt. Int. Conf*, 1997.

[27] K. Meier, M. Roellig, and A. Schiessl, “Life time prediction for lead-free solder joints under vibration loads,” *EuroSimE*, pp. 1–8, 2011.

[28] G. Khatibi, W. Wroczewski, B. Weiss, and T. Licht, “A fast mechanical test technique for life time estimation of micro-joints,” *Microelectron. Reliab.*, vol. 48, no. 11–12, pp. 1822–1830, Nov. 2008.

[29] G. Khatibi, W. Wroczewski, B. Weiss, and H. Ipser, “A novel accelerated test technique for assessment of mechanical reliability of solder interconnects,” *Microelectron. Reliab.*, vol. 49, no. 9–11, pp. 1283–1287, Sep. 2009.

[30] J.-W. Park, J.-H. Chae, I.-H. Park, H.-J. Youn, and Y.-H. Moon, “Thermo-Mechanical Stresses and Mechanical Reliability of Multilayer Ceramic Capacitors (MLCC),” *J. Am. Ceram. Soc.*, vol. 90, no. 7, pp. 2151–2158, Jul. 2007.

[31] V. Krieger, W. Wondrak, a. Dehbi, W. Bartel, Y. Ousten, and B. Levrier, “Defect detection in multilayer ceramic capacitors,” *Microelectron. Reliab.*, vol. 46, no. 9–11, pp. 1926–1931, Sep. 2006.

[32] J. Maxwell, “CRACKS: THE HIDDEN DEFECT,” *Tech. Informations Bull. AVX Corp.*, 1988.

[33] S. Wiese, M. Roellig, and M. Mueller, “The size effect on the creep properties of SnAgCu-Solder alloys,” *ECTC’07.*, pp. 548–557, 2007.

[34] H. Ma and J. C. Suhling, “A review of mechanical properties of lead-free solders for electronic packaging,” *J. Mater. Sci.*, vol. 44, no. 5, pp. 1141–1158, Jan. 2009.

[35] P. Zimprich, A. Betzwar-Kotas, G. Khatibi, B. Weiss, and H. Ipser, “Size effects in small scaled lead-free solder joints,” *J. Mater. Sci. Mater. Electron.*, vol. 19, no. 4, pp. 383–388, Jul. 2008.

[36] G. Khatibi, M. Lederer, and E. Byrne, “Characterization of Stress–Strain Response of Lead-Free Solder Joints Using a Digital Image Correlation Technique and Finite-Element Modeling,” *J. Electron. …*, vol. 42, no. 2, pp. 294–303, 2013.

[37] B. Wang, F. Wu, J. Peng, H. Liu, Y. Wu, and Y. Fang, “Effect of miniaturization on the microstructure and mechanical property of solder joints,” in *International Conference on Electronic Packaging Technology & High Density Packaging*, 2009, pp. 1149–1154.

[38] S. Wiese, M. Roellig, M. Mueller, and K.-J. Wolter, “The effect of downscaling the dimensions of solder interconnects on their creep properties,” *Microelectron. Reliab.*, vol. 48, no. 6, pp. 843–850, Jun. 2008.

[39] M. N. Islam, A. Sharif, and Y. C. Chan, “Effect of volume in interfacial reaction between eutectic Sn-3.5% Ag-0.5% Cu solder and Cu metallization in microelectronic packaging,” *J. Electron. Mater.*, vol. 34, no. 2, pp. 143–149, Feb. 2005.

[40] W. Tang, A. He, Q. Liu, and D. G. Ivey, “Solid state interfacial reactions in electrodeposited Cu/Sn couples,” *Trans. Nonferrous Met. Soc. China*, vol. 20, no. 1, pp. 90–96, Jan. 2010.

[41] O. M. Abdelhadi and L. Ladani, “IMC growth of Sn-3.5Ag/Cu system: Combined chemical reaction and diffusion mechanisms,” *J. Alloys Compd.*, vol. 537, pp. 87–99, Oct. 2012.

[42] B. G. Zagar and C. Kargel, “A laser-based strain sensor with optical preprocessing,” *IEEE Trans. Instrum. Meas.*, vol. 48, no. 1, pp. 97–101, 1999.

[43] P. Zimprich, U. Saeed, A. Betzwar-Kotas, B. Weiss, and H. Ipser, “Mechanical Size Effects in Miniaturized Lead-Free Solder Joints,” *J. Electron. Mater.*, vol. 37, no. 1, pp. 102–109, Oct. 2008.

[44] M. Lederer, G. Khatibi, and B. Weiss, “FEM simulation of the size and constraining effect in lead free solder joints,” *Appl. Comput. Mech.*, vol. 6, pp. 17–24, 2012.

[45] P. Hegde, D. C. Whalley, and V. V. Silberschmidt, “Size and microstructure effects on the stress-strain behaviour of lead-free solder joints,” *2009 Eur. Microelectron. Packag. Conf.*, 2009.

[46] M. Yunus, K. Srihari, J. M. Pitarresi, and A. Primavera, “Effect of voids on the reliability of BGA/CSP solder joints,” *Microelectron. Reliab.*, vol. 43, pp. 2077–2086, 2003.

[47] Q. Yu, T. Shibutani, D. S. Kim, Y. Kobayashi, J. Yang, and M. Shiratori, “Effect of process-induced voids on isothermal fatigue resistance of CSP lead-free solder joints,” *Microelectron. Reliab.*, vol. 48, pp. 431–437, 2008.

[48] V. Jakkali, “Finite Element Modeling of the Effect of Reflow Porosity on the Mechanical Behavior of Pb-free Solder Joints,” Arizona State University, 2011.

[49] P. Zimprich, U. Saeed, B. Weiss, and H. Ipser, “Constraining effects of lead-free solder joints during stress relaxation,” *J. Electron. Mater.*, pp. 1–28, 2009.

[50] T. An and F. Qin, “Effects of the intermetallic compound microstructure on the tensile behavior of Sn3.0Ag0.5Cu/Cu solder joint under various strain rates,” *Microelectron. Reliab.*, vol. 54, no. 5, pp. 932–938, May 2014.

[51] X. Li, X. Yang, and F. Li, “Effect of isothermal aging on interfacial IMC growth and fracture behavior of SnAgCu/Cu soldered joints,” in *ICEPT-HDP*, 2008.

[52] C. C. Lee, P. J. Wang, and J. S. Kim, “Are Intermetallics in Solder Joints Really Brittle?,” in *57th Electronic Components and Technology Conference*, 2007, pp. 648–652.

[53] M. Lederer, J. Magnien, G. Khatibi, and B. Weiss, “FEM simulation of the size- and constraining effect in leadfree solder joints with the theory of strain gradient elasticity,” *J. Phys. Conf. Ser. Accept.*

[54] I. Shohji, T. Yoshida, T. Takahashi, and S. Hioki, “Tensile properties of Sn-Ag based lead-free solders and strain rate sensitivity,” *Mater. Sci. Eng. A*, vol. 366, pp. 50–55, 2004.

[55] F. Lang, H. Tanaka, O. Munegata, T. Taguchi, and T. Narita, “The effect of strain rate and temperature on the tensile properties of Sn-3.5Ag solder,” *Mater. Charact.*, vol. 54, pp. 223–229, 2005.

[56] R. J. Mccabe and M. E. Fine, “Creep of Tin, Sb-Solution-Strengthened Tin, and SbSn- Precipitate-Strengthened Tin,” *Metall. Mater. Trans. A*, vol. 33, no. May, pp. 1531–1539, 2002.

[57] M. Anwander, B. G. Zagar, B. Weiss, and H. Weiss, “Noncontacting strain measurements at high temperatures by the digital laser speckle technique,” *Exp. Mech.*, vol. 40, no. 1, pp. 98–105, Mar. 2000.

[58] B. Weiss, V. Gröger, G. Khatibi, a. Kotas, P. Zimprich, R. Stickler, and B. Zagar, “Characterization of mechanical and thermal properties of thin Cu foils and wires,” *Sensors Actuators A Phys.*, vol. 99, no. 1–2, pp. 172–182, Apr. 2002.

[59] W. N. Sharpe, “Applications of the interferometric strain/displacementgauge,” *Opt. Eng.*, vol. 21, pp. 483–488, 1982.

[60] B. Zagar, H. Weiss, M. Anwander, B. Weiss, and R. Stickler, “A laser interferometric system for local strain measurements with nanometer resolution,” in *Local strain and temperature measurements in non-uniform fields at elevated temperatures*, 1996, pp. 87–97.

[61] J. Magnien, T. Baumgartner, and G. Khatibi, “LASER OPTICAL STRAIN SENSOR APPLICATION FOR MINIATURIZED SYSTEMS,” in *3. Tagung Innovation Messtechnik*, 2013, pp. 31–34.

[62] B. G. Zagar, “A laser-interferometer measuring displacement with nanometer resolution,” *1993 IEEE Instrum. Meas. Technol. Conf.*, vol. 1, no. 4, 1993.

[63] P. Hidnert and H. S. Krider, “Thermal Expansion of Aluminum and Some Aluminum Alloys,” *J. Res. Natl. Bur. Stand. (1934).*, vol. 48, no. 3, pp. 209–220, 1952.

[64] T. Bieler and H. Jiang, “Influence of Sn grain size and orientation on the thermomechanical response and reliability of Pb-free solder joints,” *Electron. Components Technol. Conf.*, no. 2, pp. 1462–1467, 2006.

[65] R. J. Fields and S. R. Low III, “Physical and mechanical properties of intermetallic compounds commonly found in solder joints,” *Metal Science of Joining*, 1991. [Online]. Available: http://www.metallurgy.nist.gov/mechanical_properties/solder_paper.html.

[66] T. A. Hahn, “Thermal Expansion of Copper from 20 to 800 K—Standard Reference Material 736,” *J. Appl. Phys.*, vol. 41, no. 13, p. 5096, 1970.

[67] D. Xie, Y. Chan, J. Lai, and I. Hui, “Fatigue life estimation of surface mount solder joints,” *… Technol. Part B …*, vol. 19, no. 3, 1996.

[68] K. Meier and M. Roellig, “Reliability study on chip capacitor solder joints under thermo-mechanical and vibration loading,” *hermal, Mech. …*, pp. 1–7, 2014.

[69] T.-S. Park and S.-B. Lee, “Low Cycle Fatigue Testing of Ball Grid Array Solder Joints under Mixed-Mode Loading Conditions,” *J. Electron. Packag.*, vol. 127, no. 3, p. 237, 2005.

[70] A. Conle, T. R. Oxland, and T. H. Topper, “Computer-based prediction of cyclic deformation and fatigue behavior,” *ASTM Spec. Tech. Publ.*, pp. 1218–1236, 1988.

[71] A. Mayyas, A. Qasaimeh, P. Borgesen, and M. Meilunas, “Effects of latent damage of recrystallization on lead free solder joints,” *Microelectron. Reliab.*, vol. 54, pp. 447–456, 2014.

[72] G. Khatibi, V. Gröger, B. Weiss, G. Lefranc, and G. Mitic, “Verfahren zur zyklischen Scherbelastungsprüfung von Mikroverbindungen zwischen Werkstoffen,” Nr. 10 2005 016 038.7., 2005.

[73] G. Khatibi, P. Zimprich, and V. Groeger, “A new technique for shear fatigue testing of microjoints,” *Int. Fatigue*, 2006.

[74] Y. Zhou, M. Al-Bassyiouni, and A. Dasgupta, “Vibration Durability Assessment of Sn3.0Ag0.5Cu and Sn37Pb Solders Under Harmonic Excitation,” *J. Electron. Packag.*, vol. 131, no. 2009, p. 011016, 2009.

[75] J. W. Kim and S. B. Jung, “Experimental and finite element analysis of the shear speed effects on the Sn-Ag and Sn-Ag-Cu BGA solder joints,” *Mater. Sci. Eng. A*, vol. 371, pp. 267–276, 2004.

[76] A. U. Telang, T. R. Bieler, S. Choi, and K. N. Subramanian, “Orientation imaging studies of Sn-based electronic,” *J. Mater. Res.*, vol. 17, no. 9, pp. 2294–306, 2002.

LIST OF TABLES

LIST OF FIGURES

Chapter 1:

Chapter 2:

Chapter 3:

Chapter 4:

Chapter 5:

Chapter 6:

APPENDIX

Chapter 2 Tensile Properties Measurement and Microstructure Analysis for SnAgCu Lead-Free Solders

Figure 2.6.Growth of intermetallic compounds with respect to the aging time at 150°C.

Sqr Time [h^1/2]	Total IMC [µm]	Cu_3Sn [µm]	Cu_6Sn_5 [µm]
0.0	2.6	0.0	2.6
22.4	6.5	2.3	4.2
31.6	8.4	3.1	5.3

Figure 2.7. Calculated Growth kinetics for the IMC layer depending on the produced gap size and heat treatment at 150°C.

Solder Gap Thickness [µm]	Total IMC Y Growth [µm/h^1/2]	Cu_3Sn Y Growth [µm/h^1/2]	Cu_6Sn_5 Y Growth [µm/h^1/2]
800	0.19	0.09	0.09
400	0.19	0.10	0.09
100	0.18	0.10	0.08
50	0.17	0.11	0.06

Figure 2.8. Interfacial IMCs layer proportion of different gap sizes with the corresponding totally IMC layer thickness for different heat treatments.

Solder Gap Thickness [µm]	Nonaged IMC Layer Proportion [%]	150°C, 500h IMC Layer Proportion [%]	150°C, 1000h IMC Layer Proportion [%]	Nonaged IMC Thickness [µm]	150°C, 500h IMC Thickness [µm]	150°C, 1000h IMC Thickness [µm]
800	0.7	1.7	2.3	2.9	6.9	8.9
400	1.3	3.3	4.3	2.5	6.6	8.5
100	4.9	12.8	16.6	2.4	6.4	8.3
50	9.6	24.12	30.6	2.4	6.0	7.6

Figure 2.9. Relationship between Cu_6Sn_5 and Cu_3Sn layer thicknesses to the solder gap size after aging at 150°C/500h and 150°C/1000h.

Solder Gap Thickness [µm]	150°C, 500h IMC Thickness Cu_3Sn [µm]	150°C, 1000h IMC Thickness Cu_3Sn [µm]	150°C, 500h IMC Thickness Cu_6Sn_5 [µm]	150°C, 1000h IMC Thickness Cu_6Sn_5 [µm]
800	2.1	2.9	4.8	5.9
400	2.2	3.0	4.5	5.5
100	2.5	3.2	3.9	5.1
50	2.6	3.3	3.4	4.4

Figure 2.12. Dependencies of tensile strength and fracture strain on solder gap thickness. a) fracture strain behavior without defects, b) fracture strain with voids in the solder due the soldering.

Solder Gap Thickness [µm]	(a) UTS [MPa]	Fracture strain [%]	(b) UTS [MPa]	Fracture strain [%]
800	50.6	0.94	60.1	0.16
400	64.2	0.57	76.1	0.14
100	87.1	0.10	87.1	0.10
50	113.0	0.09	113.0	0.09

Figure 2.13. Strain rate dependence of the ultimate tensile strength as a function of solder gap thickness.

Solder Gap Thickness [µm]	0.2 mm/min UTS [MPa]	Solder Gap Thickness [µm]	$3.5x10^{-3}$ s^{-1} UTS [MPa]
960.3	48.6	960.3	48.6
832.2	47.5	372.3	58.6
840.0	48.7	152.1	73.1
840.0	48.7	62.9	90.5
391.7	61.7	413.1	61.6
406.8	68.3	107.4	71.2
538.5	60.3	47.6	109.5
533.7	55.6	775.0	50.3
409.6	60.4	411.0	51.8
123.2	75.0	186.3	61.0
96.4	89.6	110.1	71.4
177.9	70.0	60.5	110.0
95.1	81.3	44.9	115.3

Figure 2.15. Dependency of tensile strength on solder gap thickness for different aging conditions.

Solder Gap Thickness [µm]	Nonaged UTS [MPa]	150°C, 500h UTS [MPa]	150°C, 1000h UTS [MPa]
800	50.6	47.4	40.2
400	64.2	55.0	46.0
100	87.1	73.3	66.6
50	113.0	98.0	78.8

Figure 2.16. Dependency of fracture strain on solder gap thickness for different aging conditions.

Solder Gap Thickness [µm]	Nonaged Fracture Strain [%]	150°C, 500h Fracture Strain [%]	150°C, 1000h Fracture Strain [%]
800	0.94	2.3	3.3
400	0.57	1.5	2.1
100	0.10	0.5	0.8
50	0.09	0.3	0.5

Figure 2.19. Effect of temperature on tensile strength of Cu/Sn3.5Ag0.75Cu/Cu solder joints with different gap thicknesses at RT, 80°C and 125°C.

Solder Gap Thickness [µm]	UTS at RT [MPa]	UTS at 80°C [MPa]	UTS at 125°C [MPa]
800	50.6	42.6	36.3
400	64.2	55.0	47.1
100	87.1	71.4	62.0
50	113.0	81.3	64.9

Figure 2.26. Dependencies of Von Mises strain on solder gap thickness of different aging conditions before crack initiation.

Solder Gap Thickness [µm]	Von Mises Strain [%]	Von Mises Strain [%]	Von Mises Strain [%]
800	6.3	8.1	9.2
400	5.3	6.6	7.2
100	2.9	3.5	3.8

CHAPTER 3 Creep Behavior of SnAgCu Lead-Free Solder System

Figure 3.6. Dependency of the stress exponent n_2 on solder gap thickness of different isothermal boundary conditions RT, 80°C and 125°C.

SnAgCu Gap Thickness [µm]	n, RT	n, 80°C	n, 125°C
830	14.4	7.6	5.3
450	31.9	9.4	5.5
200	121.0	32.2	13.3
130	255.4	170.4	78.7

Figure 3.7. Activation energy versus solder gap thickness of the solder alloys Sn3.5Ag0.75Cu and Sn3.5Ag [literature].

SnAgCu Gap Thickness [µm]	SnAgCu, Q [kJ/mol]	SnAg Gap Thickness [µm]	SnAg, Q [kJ/mol]
830	55.4	750	44
450	61.9	550	54
200	69.6	250	68
130	72.9	150	68

Figure 3.8. Dependencies of stress reduction on solder gap thickness of different aging conditions at RT.

Solder Gap Thickness [µm]	Nonaged Reduction [%]	Solder Gap Thickness [µm]	150°C, 1000h Reduction [%]
780	12.5	830	18.5
830	13.4	780	17.7
810	13.4	800	19.0
560	8.8	480	8.5
450	6.2	440	9.4
480	6.0	540	11.3
180	3.3	200	3.0
200	3.1	210	2.5
160	3.6	180	2.9
90	2.7	110	1.4
130	2.9	130	2.5
110	2.5	100	1.9

Figure 3.9. Dependencies of stress reduction on solder gap thickness of different aging conditions at 80°C.

Solder Gap Thickness [µm]	Nonaged Reduction [%]	Solder Gap Thickness [µm]	150°C, 500h Reduction [%]	Solder Gap Thickness [µm]	150°C, 1000h Reduction [%]
970	25.9	910	34.9	840	39.0
820	21.0	840	27.0	750	34.5
850	21.0	810	25.0	810	35.9
430	12.9	380	12.1	480	12.5
450	14.9	450	10.9	440	16.9
400	12.0	400	11.2	420	15.5
210	4.7	190	4.5	150	3.1
180	3.9	170	3.9	180	4.0
200	5.0	210	4.0	200	4.5
110	3.4	130	2.1	100	2.0
130	3.5	100	3.3	120	2.4
90	3.6	110	1.9	90	2.5

Figure 3.10. Dependencies of stress reduction on solder gap thickness of different aging conditions at 125°C.

Solder Gap Thickness [µm]	Nonaged Reduction [%]	Solder Gap Thickness [µm]	150°C, 500h Reduction [%]	Solder Gap Thickness [µm]	150°C, 1000h Reduction [%]
830	35.0	860	39.0	860	37.4
730	25.5	800	37.4	890	48.0
800	31.0	810	36.0	810	41.0
470	17.0	420	18.0	400	18.8
390	14.9	470	19.0	460	20.0
400	15.7	390	17.0	410	18.0
180	5.5	190	5.0	220	6.4
160	4.7	240	10.1	180	6.5
200	5.7	220	8.0	200	3.9
100	2.9	100	4.0	110	4.0
110	2.9	120	6.0	130	3.3
120	4.0	140	2.5	90	4.0

Chapter 4 Coefficient of Thermal Expansion of Miniaturized SnAgCu Solder Joints

Figure 4.3. Thermal strain measurements using an Aluminum NIST sample for calibration of the LIS.

dT [K]	Sample #1 Thermal Strain [ppm]	Sample #2 Thermal Strain [ppm]
9	179	196
19	383	419
29	633	640
39	874	906
49	1143	1179

Figure 4.6. Thermal strain versus temperature change of 80 μm and 120 μm solder gap starting from room temperature up to a temperature difference of 102°C.

dT [°C]	80μm Thermal Strain [ppm]	120μm Thermal Strain [ppm]
18	435	582
62	1823	1966
102	3308	3456

Figure 4.7. Thermal strain versus temperature change of a 120 μm solder gap starting from room temperature subjected to 80°C/3h, 150°C/500h and 150°C/1000h heat treatments.

dT [°C]	Nonaged Thermal Strain [ppm]	150°C/500h Thermal Strain [ppm]	150°C/1000h Thermal Strain [ppm]
18	582	447	312
62	1966	1604	1269
102	3456	2869	2387

Figure 4.8. Thermal strain versus temperature change of a 80 μm solder gap starting from room temperature subjected to 80°C/3h, 150°C/500h and 150°C/1000h heat treatments.

dT [°C]	Nonaged Thermal Strain [ppm]	150°C/500h Thermal Strain [ppm]	150°C/1000h Thermal Strain [ppm]
18	435	316	225
62	1823	1617	1431
102	3308	3143	2898

Figure 4.9. Calculated CTE values of two SnAgCu gap thicknesses (80 µm and 120 µm) with respect to their aging time at 150°C.

Aging Time [h]	80µm CTE [ppm/°C]	120µm CTE [ppm/°C]
0	26.19	25.93
500	21.43	21.24
1000	18.57	15.84

Chapter 5 High Cycle Fatigue of Surface Mounted Device Solder Connection

Figure 5.6. Lifetime of the meniscus type solder joints in SMDs at RT.

Shear Stress [MPa]	Sample #1 Nf [10^6]	Sample #2 Nf [10^6]	Sample #3 Nf [10^6]	Sample #4 Nf [10^6]	Sample #5 Nf [10^6]
7.9	41.8	13.6	42.0	15.9	17.6
7.5	18.0	20.5	21.3	21.3	22.1
7.1	54.8	25.1	26.9	27.4	28.1
6.6	35.4	29.5	37.4	50.4	11.7
6.2	31.3	50.4	75.4	60.8	80.4
5.7	735.1	235.9	501.5	447.4	345.8

Figure 5.11. Lifetime curves of the SMDs with different shear loading directions at RT.

Y-Orientation Shear Stress [MPa]	Sample #1 Nf [10^6]	Sample #2 Nf [10^6]	Sample #3 Nf [10^6]
10.8	0.6	0.1	0.4
10.1	0.4	0.7	
9.3	1.1	0.9	
8.5	1.0	1.7	
7.7	2.5	2.1	
7.0	2.8	3.4	
6.2	5.5	4.8	

Figure 5.14. Lifetime of the meniscus type solder joints in SMDs for different heat treatments tested at RT.

Shear Stress [MPa]	Nonaged Nf [10^6]	150°C 250h Nf [10^6]	150°C 500h Nf [10^6]	150°C 1000h Nf [10^6]	Shear Stress [MPa]	Nonaged Nf [10^6]	150°C 250h Nf [10^6]	150°C 500h Nf [10^6]	150°C 1000h Nf [10^6]
7.9	41.8	2.1	1.6	0.6	6.2	31.3	13.4	10.1	9.7
7.9	13.6	2.9	1.2	0.5	6.2	50.4	12.4	120.9	10.1
7.9	42.0	2.5	0.6	0.7	6.2	75.4	15.2	20.3	8.9
7.9	15.8	3.0	1.1	0.9	6.2	60.8	14.5	9.6	11.1
7.9	17.6	2.8	0.9	0.9	6.2	80.4	16.4	8.7	7.5
7.5	18.0	2.5	1.6	0.3	5.7	735.1	311.0	28.9	16.9
7.5	20.4	2.1	1.2	1.1	5.7	235.9	71.7	50.4	18.4
7.5	21.3	2.6	1.7	0.9	5.7	501.5	48.9	22.5	72.7
7.5	21.3	3.5	1.9	0.9	5.7	447.4	33.1	19.8	12.8
7.5	22.1	3.1	1.4	0.7	5.7	345.7	40.5	15.7	14.7
7.1	54.8	1.8	2.4	1.7	5.3		312.4	143.4	102.6
7.1	25.1	2.9	1.7	1.2	5.3		451.5	177.5	157.2
7.1	26.9	3.1	2.5	0.7	5.3		850.6	251.3	137.6
7.1	27.4	3.5	2.6	2.2	5.3		905.4	400.5	146.7
7.1	28.1	3.9	2.2	1.5	5.3		551.8	359.1	86.7
6.6	35.4	9.6	0.9	4.1	4.8				404.0
6.6	29.4	6.4	5.1	2.8	4.8				389.4
6.6	37.4	6.7	4.5	3.8	4.8				357.9
6.6	50.4	11.9	10.0	4.4	4.8				674.2
6.6	11.7	7.5	3.9	3.2	4.8				802.4

Figure 5.17. Lifetime of non-aged SMDs tested at RT and 80 °C.

Shear Stress [MPa]	Nonaged b (80°C) Nf [10^6]	Shear Stress [MPa]	Nonaged b (80°C) Nf [10^6]	Shear Stress [MPa]	Nonaged b (80°C) Nf [10^6]	Shear Stress [MPa]	Nonaged c (80°C) Nf [10^6]	Shear Stress [MPa]	Nonaged c (80°C) Nf [10^6]
6.2	2,545	5.7	9,98	5.3	49,364	6.6	0.2	5.3	2.7
6.2	2,171	5.7	24,04	5.3	45,698	6.6	0.3	5.3	4.5
6.2	2,76	5.7	25,73	4.8	289,712	6.6	0.3		
6.2	2,131	5.7	14,987	4.8	259,18	6.2	2.5		
6.2	2,689	5.7	12,131	4.8	356,48	6.2	0.2		
6.2	3,456	5.3	30,465	4.8	569,99	6.2	0.4		
6.2	2,764	5.3	39,803	4.8	485,8	6.2	0.4		
5.7	10,845	5.3	32,514	4.8	712,39	5.7	0.6		
5.7	13,77	5.3	134,374	4.8	654,91	5.7	0.5		
5.7	24,89	5.3	175,313			5.3	1.3		

Julien MAGNIEN, Mag. rer. nat.
e-mail: jul.magnien@gmail.com

Curriculum vitae

Personal Details

date of birth:	25 december 1984
nationality:	Austria, France

Academic curriculum vitae

2011-dato: doctoral studies at the University of Vienna;thesis: „Investigation of Mechanical Behavior and Failure Mechanisms in Miniaturized Solder Interconnects“; Physics of Nanostructured Materials; advicer: Prof. Dr. Herbert Ipser & Dr. Golta Khatibi

2005-2010: diploma studies at the Karl Franzens University; thesis: „Printed, flexible, organic, opto-thermal Sensor“; Institute of Physics; advicer: Prof. Dr. Joachim Krenn

Additional Skills

mother tongue:	German
language:	French
	English

Work and Research Experience:

2015-dato: Materials Center Leoben Forschung GmbH; scientist in the field „Microelectronics“

2011-2015: Materials Center Leoben Forschung GmbH; postgraduate research in the field „Lifetime of Functional Multilayer Ceramic Systems (FMCS)“

2009-2010: Joanneum Research Forschungsgesellschaft; graduate research in the field „Organic Electronics“

Recent research interests

Material Science; Microelectronics; Fatigue Testing; Reliability; Solder Technology; Device Characterization; Electronics; Nanotechnology

Publications

Assessment of mechanical reliability of surface mounted capacitor by an accelerated shear fatigue test technique; J. Magnien, G. Khatibi; Microelectronics Reliability, 54, 9-10, 1764-9; 2014

Laser optical strain sensor application for miniaturized systems; J. Magnien, T. Baumgartner, G. Khatibi; Proceedings of the 3rd Meeting on Innovation Measurement, 31-4; 2013

Fully printed, flexible, large Area Organic Optothermal Sensors for Human-Machine-Interfaces; M. Zirkl, G. Scheipl, B. Stadlober, et al.; Eurosensors Xxiv Conference, 5, 725-729; 2010